Installation and testing of the Isobar Separator for Anions at the A. E. Lalonde AMS Laboratory using chlorine-36 analysis

by

Erin Flannigan

A thesis submitted in partial fulfillment
of the requirements for the
Doctor of Philosophy
degree in Physics

Department of Physics
Faculty of Science
University of Ottawa

ABSTRACT

Installation and testing of the Isobar Separator for Anions at the A. E. Lalonde AMS Laboratory using chlorine-36 analysis

Erin Flannigan
University of Ottawa, 2023

Advisor:
Dr. W. E. Kieser

Accelerator Mass Spectrometry (AMS) studies of rare isotopes with abundant isobars that form negative ions often require the use of large accelerators to achieve high sensitivity measurements. The Isobar Separator for Anions (ISA) is a radiofrequency quadrupole (RFQ) reaction cell system that provides selective isobar suppression for many of these isotopes in the low energy system, prior to injection into an accelerator. The ISA can then facilitate the measurement of these ions using smaller accelerators. A commercial version from *Isobarex Corp.* was installed in a separate low energy injection line of the 3 MV accelerator system at the A. E. Lalonde AMS Laboratory in the University of Ottawa and was tested using the measurement of ^{36}Cl, suppressing its stable isobar ^{36}S.

The ISA includes a DC deceleration region, a combined cooling and reaction cell, and a DC acceleration region. The deceleration region reduces the beam energy from the ion source (20-35 keV) to a level that chemical reactions can occur, scattering is minimized, and that the reaction cell can accept and contain. RFQ segments along the length of the cell create a potential well, which limits the divergence of the traversing ions. DC offset voltages on these RFQ segments maintain a controlled ion velocity through the cell.

Helium was used as a cooling gas to further decelerate the ions, facilitating charge exchange between ^{36}S and a reaction gas. Helium provided the highest transmission of 30-80% for chlorine anions. The reaction gas NO_2 was chosen to preferentially react with sulfur. Over seven orders of magnitude reduction of sulfur to chlorine was observed. After exiting the cell, the beam is reaccelerated prior to injection into the tandem accelerator for AMS analysis.

Using ^{36}Cl reference materials, it was determined that linear transmission results could be obtained for a ^{36}Cl/Cl ratio ranging from 10^{-11} to 10^{-15}. The measurements were stable over more than 24 hours of continuous measurement. A blank level on the order of 10^{-15} was observed. The ISA was used to measure unknown ^{36}Cl /Cl ratio groundwater samples and the results are compared to external AMS measurements.

Acknowledgements

Most of the research described in this thesis was performed at the AEL-AMS laboratory, a national research facility hosted at the University of Ottawa. This project was possible through funding from the Canada Foundation of Innovation's Infrastructure Fund 'MicroSTARR' and Major Science Initiatives (MSI) programs, the Ontario Research Fund, Innovative Solutions Canada, and the Natural Sciences and Engineering Research Council of Canada (NSERC).

I would first like to thank my advisor, Dr. Liam Kieser. I am grateful for all of your guidance and encouragement throughout this work, the scientific discussions, and for lending your technical and scientific expertise. This work would not be possible without you.

I am also very grateful to Dr. Xiaolei Zhao for dedicating his time and expertise to training me on the accelerator. I appreciate your help with the technical requirements for measuring Cl on the AMS system, all of the times you shared your knowledge, and the in-depth discussions we were able to have.

I would like to thank *Isobarex Corp.*, including Dr. Jean-François Alary, Dr. Reza Javarhery, and Dr. Lisa Cousins for designing and producing the Isobar Separator for Anions used in this research. I would also like to thank you for your helpful advice and scientific discussions throughout these years. I would especially like to thank Dr. Jean-François Alary for dedicating so much of your time to helping with my experimental and technical work and for training me on the ISA.

I would like to thank many current and former members of A. E. Lalonde. Thank you to Dr. Collin Tiessen for your helpful discussions and edits. Having the support of a fellow graduate student was very appreciated. Thank you to Normand St-Jean for your assistance with AMS system operations and technical support. Thank you to Dr. Barbara Francisco and Carley Crann for your assistance with sample preparation. Thank you to Dr. Doru Pacesila for helping with accelerator tuning. Thank you to Dr. Marie-Josée Nadeau for your helpful scientfic discussions and manuscript edits.

I would like to extend my appreciation to those that generously prepared and supplied samples for my research including Dr. John Gosse, Dr. Guang Yang, Dr. Ian Clark, and Monika Wilk.

I would like to thank Dr. Adina Lucian-Mayer, Dr. Razvan Gornea, and Dr. Ian Clark for serving as my advisory committee members and offering feedback towards my research. I am thankful to the Physics Department at the University of Ottawa for their administrative support and the graduate course offerings.

I am appreciative of Dr. Iain Campbell for your continued mentorship over the past decade. I am very lucky to continue research with you.

Finally, I am forever grateful to my life outside of my research. I am indebited to my partner, David Bolton. Thank you for your manuscript edits but most importantly for your patience and support during these years. Thank you to all of my friends but especially Kathleen Songin, Kelly Copestake, Rachel McGrath, and Scott Gardner for your long distance love and support through this journey. Thank you to Spencer Sterling and Dr. Benoit Vanus for making sure that I leave the house. All of your friendships mean so much to me. I would like to thank my parents and my brother, I would not be who I am without your encouragement.

Contents

List of Tables

List of Figures

List of Acronyms and Abbreviations

AEL-AMS André E. Lalonde accelerator mass spectrometry

AMS Accelerator mass spectrometry

ALIS Anion Laser Isobar Separator

BPM beam profile monitor

CAMS-LLNL Center for Accelerator Mass Spectrometry, Lawrence Livermore National Laboratory

CAN controlled area network

CRISDal Cosmic Ray Isotope Sciences at Dalhousie Lab

ESA electrostatic analyzer

ETH Eidgenössische Technische Hochschule (Zurich, Switzerland)

FSI fast sequential injection

GIC gas ionization chamber

HE high energy

HVEE High Voltage Engineering Europa BV

ICP-MS inductively coupled plasma mass spectrometry

ILIAMS Ion-Laser InterAction Mass Spectrometry

ISA Isobar Separator for Anions

LE low energy

LOD limit of detection

LOQ limit of quantification

LSC liquid scintillation counting

MS/MS Tandem mass spectrometry or mass spectrometry/mass spectrometry

NIST National Institute of Standards and Technology

PRIME Purdue Rare Isotope Measurement

RF radiofrequency

RFQ radiofrequency quadrupole

ROI region of interest

SCCM standard cubic centimeters per minute

SRM standard reference material

SSI slow sequential injection

VERA Vienna Environmental Research Accelerator

Chapter 1

Introduction

1.1 Accelerator Mass Spectrometry

Accelerator mass spectrometry (AMS) is a highly sensitive method of counting single atoms to measure isotopic ratios in the range 10^{-11} to 10^{-16} [1]. AMS evolved from mass spectrometry and the ion sources, accelerators, and detectors used in nuclear physics laboratories during the 1960s and 1970s [2]. The important work of Roy Middleton and Purser et al. [3], showing that ^{14}N does not form a stable negative ion, led to the first detection of ^{14}C anions using a tandem accelerator [4, 5]. Prior to these measurements, decay counting was used to measure ^{14}C concentration. AMS reduced the sample size by a factor of 1000 and reduced the measuring time by a factor of 100 [1]. Compared to the many other mass spectrometry techniques, AMS also has superior suppression of isobaric background and an increased sensitivity limit.

While the measurement of ^{14}C is still the most widely used application of AMS, the field has expanded to include the measurement of many isotopes for a variety of applications [6]. The most common of these isotopes include ^{10}Be, ^{26}Al, ^{36}Cl, ^{41}Ca, and ^{129}I. AMS is only able to measure these low isotopic ratios when elemental and molecular isobars, elements with the same mass as the isotope of interest, can be suppressed. This limits the isotopes available to AMS study. Current techniques being employed for the suppression of abundent isobars are discussed in Section 1.1.1.

AMS is an expensive technique that requires large amounts of space. A typical AMS system will contain a negative ion source (most commonly a Cs$^+$ sputter ion source), an accelerator that firsts accelerates the negative ions, strips them of a selectable number of electrons, and then further accelerates the now positive ions, electrostatic and magnetic analyzers, and a detector that identifies and counts single atoms [7]. While some AMS facilities have large accelerators with terminal voltages of 5-10 MV or greater, many AMS facilities use medium accelerators with terminal voltages of 2-3 MV [8, 9]. These medium accelerators are of sufficient energy for the measurement of most commonly studied isotopes. In recent years, there has been a trend towards small accelerators (0.2-1 MV), which greatly reduce initial investment, operating cost, and space required [9]. These machines are predominately used to study ^{14}C but have also been applied to isotopes such as ^{10}Be, ^{26}Al, ^{129}I, and ^{244}Pu [10].

1.1.1 Isobar Suppression

The ability to separate isobars from an ion beam has been essential to the development of AMS. Molecular isobars are removed in the stripping canal of a tandem accelerator or following a single stage AMS system. At the terminal of the tandem accelerator, the electrons are stripped from the anion to create a cation that is further accelerated. During this stripping process molecules are dissociated, with most molecules dissociating at a charge state over 2+ [11].

The first of the elemental isobar removal techniques occurs in the negative ion source; isobars with negative electron affinities will not form stable anions. This separation technique is only available in rare cases, including the removal of ^{14}N, ^{26}Mg, ^{55}Mn, and ^{129}Xe in the detection of ^{14}C, ^{26}Al, ^{55}Fe and ^{129}I, respectively [12, 2]. Most atomic isobars will form stable anions and therefore require different removal techniques.

In the case of the removal of ^{10}B in the measurement of ^{10}Be, degrader foils may be used to separate the isobars through differential energy loss [10, 13]. Additional techniques such as complete stripping of ions [14], or gas-filled magnets [15] are also used. Often these separation techniques are only possible with large, high energy accelerators and despite these techniques, even large accelerators are often unable to achieve the separation necessary to study some heavier elements [2].

As smaller accelerators have advantageous costs and size, isobar suppression techniques that do not require high energies must be developed. The suppression of these isobars in the low energy end of the AMS system has been of great interest in recent years. Two methods of on-line, low energy isobar suppression are currently being investigated. One of these methods uses a gas-filled reaction cell to facilitate ion-gas molecule reactions or collisional-induced dissociation at eV energies. The focus of this thesis involves the use of the Isobar Separator for Anions (ISA), discussed further in Section 1.2 to apply this technique.

The second of these techniques uses non-resonant laser photodetachment to remove unwanted isobars. This method exploits the difference in electron affinities between an isobar and the isotope of interest. Inside a cooling gas-filled radiofrequency quadrupole (RFQ) ion guide, the ion beam is exposed to an intense laser beam. When an ion has an electron affinity below the energy of the laser, the ion will become a neutral element through photodetachment; ions with higher electron affinities will pass through unaffected [16]. The Ion-Laser InterAction Mass Spectrometry (ILIAMS), which exploits this technique, is currently being used at the Vienna Environmental Research Accelerator (VERA) to study ^{36}Cl, ^{26}Al, ^{90}Sr, and ^{135}Cs with 3 MV AMS [17]. The use of the ILIAMS is also currently being investigated for the measurement of ^{41}Ca, ^{99}Tc, and ^{182}Hf.

The work on the ILIAMS has also successfully tested a combination of both laser photodetachment and ion-gas molecule reactions for the measurement of isotopes ^{90}Sr, and ^{182}Hf [18, 19]. The Anion Laser Isobar Separator (ALIS), which will be an RFQ ion cooler with both element-selective laser photodetachment and ion-gas reaction capabilities, is being developed for installation on the 6 MV AMS system of CologneAMS [20].

1.2 The Isobar Separator for Anions

The ISA is a gas-filled RFQ reaction cell that has been developed for the removal of isobars in the low energy end of an AMS system. It suppresses isobaric interferences using ion-gas molecule reactions, including specific collision-induced dissociation or electron transfer reactions. The ions should be at low energy to allow for thermal or near thermal reactions between the ion and reactions gases; reactions are much more likely to occur at these low energies. To confine and reduce scattering effects of these low energy ions, an RFQ ion guide is used. An RFQ creates a confining potential for the ions using a high frequency alternating field. These ion guides are described in more detail in Section 1.2.1. A brief history of the development of RFQ reaction cells and their application to isobar suppression in AMS is provided in Section 1.2.2.

1.2.1 Ion motion in RFQ ion guides

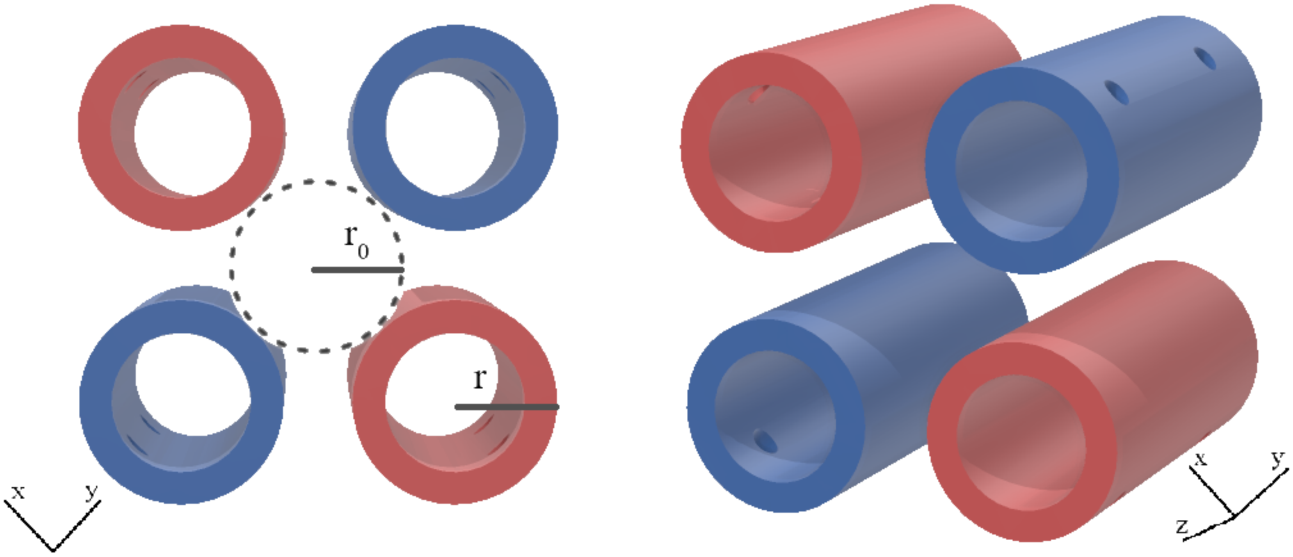

Figure 1.1: An RFQ made of four parallel cylindrical rods placed symmetrically around the central z-axis. The views from the front face and the side profile are included. Ions are injected along this central axis. Electrodes pictured in the same colour are set at the same time-dependent potential given by Equation 1.1. The neighbouring electrodes are set to the same magnitude potential but with opposite sign.

The ISA uses four cylindrical electrodes, a quadrupole, to confine ions in the x- and y-direction, while the ions travel in the z-direction. The face and profile of the RFQ structure can be seen in Figure 1.1. The electrodes are symmetrical around the central axis, with their inside surfaces on a radius of r_0. To create a pure quadrupole field, the electrodes should have a hyperbolic cross-section [21]. However, the cylindrical rods pictured in Figure 1.1 are widely used due to the ease of manufacturing this shape. To give the best approximation of a quadrupole field using round rods, the radius of the rod should be equal to $1.13r_0$ [22]. Diametrically opposite rods are given a time-dependent potential:

$$V(t) = \frac{V_{pp}}{2} cos(\omega t) - U \tag{1.1}$$

where V_{pp} is the peak-to-peak amplitude of the radiofrequency (RF) voltage, U is a DC voltage applied to the rods, and ω is 2πf for a fixed frequency. Neighbouring rods have the same magnitude potential but with the opposite sign.

The resulting 2-dimensional potential, ϕ_2, in the Cartesian plane is restoring in one direction and repulsive in the other. This potential is well known for a quadrupole, given by the equation [23]:

$$\phi_2(x, y, t) = \frac{(x^2 - y^2)}{2r_0^2}(U - V_{pp} cos\omega t) \tag{1.2}$$

The force on an ion with mass m and charge q is determined by:

$$\vec{F} = m\frac{d\vec{v}}{dt} = -q\nabla\phi_2(x, y, t) \tag{1.3}$$

With no collisions, the ions would move freely along the z-axis. The motion in the x- and y-direction can be determined using Equations 1.2 and 1.3:

$$\frac{\partial^2 x}{\partial t^2} + \frac{q}{mr_0^2}[U - V_{pp} cos\omega t]x = 0 \tag{1.4}$$

$$\frac{\partial^2 y}{\partial t^2} - \frac{q}{mr_0^2}[U - V_{pp} cos\omega t]y = 0 \tag{1.5}$$

The motion in x and y are decoupled from each other for a quadrupole. A parameter ξ can be defined as:

$$\xi = \frac{\omega t}{2} \tag{1.6}$$

This provides the following substitutions:

$$\frac{\partial^2 x}{\partial t^2} = \frac{w^2}{4}\frac{\partial^2 x}{\partial \xi^2} \tag{1.7}$$

$$\frac{\partial^2 y}{\partial t^2} = \frac{w^2}{4}\frac{\partial^2 y}{\partial \xi^2} \tag{1.8}$$

Using these substitutions, Equations 1.4 and 1.5 can lead to the differential equations known as the Mathieu differential equations [23]:

$$\frac{\partial^2 x}{\partial \xi^2} + [a_2 - 2q_2 cos(2\xi)]x = 0 \tag{1.9}$$

$$\frac{\partial^2 y}{\partial \xi^2} - [a_2 - 2q_2 cos(2\xi)]y = 0 \tag{1.10}$$

where the dimensionless parameters q_2 and a_2 are defined as:

$$q_2 = \frac{2qV_{pp}}{mr_0^2\omega^2} \tag{1.11}$$

$$a_2 = \frac{4qU}{mr_0^2\omega^2} \tag{1.12}$$

where the subscript '2' identifies the order of the pole symmetry of a quadrupole. The parameters q_2 and a_2 are referred to as 'stability parameters'. The solutions of the Mathieu differential equations describe the trajectories of the ions and are classified as stable or unstable. This stability is often demonstrated on a stability diagram which can be found in Tanner *et al.* [24] and Dawson [25]. An a_2-q_2 stability diagram shows where the ion trajectories are stable in both the x- and the y-direction.

With both q_2 and a_2 dependent on the m/q ratio of a particle, these quadrupoles may be used as a mass filter if a_2/q_2 is kept constant [25]. However, the ion guide used for the ISA does not require mass filtering and so the DC potential, U, is set to 0. This results in $a_2=0$ and the stability of the ions is therefore only dependent on q_2. When a quadrupole system is operated with these parameters, it is referred to as a quadrupole ion guide.

The solutions discussed here are only applicable to single charged ions in a vacuum and are not complete when the ion guide includes a cooling or reaction gas or when space charge effects are present.

1.2.2 Radiofrequency Quadrupole Reaction Cells

Using RF fields to confine and guide ions was proposed by Paul and Steinwedel in the 1950s [26]. The first devices were created in the 1960s but research using RFQs as linear ion guides and mass filters did not pick up until the 1970s-1980s when they were used as collision or reaction cells.

RFQ reaction cells are an extension of these ion guides. They allow for ion chemistry or reaction studies; collisional reactions between an ion and a neutral gas molecule are promoted in the RFQ environment. The products of these reactions can then be studied downstream of the RFQ reaction cell. The applications include trace gas analysis, elemental or isotopic analysis, and organic analysis [25].

Tandem mass spectrometry or mass spectrometry/mass spectrometry (MS/MS) with an RFQ ion guide was applied to isobar suppression in the late 1980s. These instruments use an RFQ as a mass filter to select out an ion of interest, a second RFQ as an ion guide or collisional cell, and then a final mass filter RFQ to separate the daughter products from the collisions. This technique was successfully used in inductively coupled plasma mass spectrometry (ICP-MS) using Ar gas [27, 28]. Previously, magnet-based instruments were used. The RFQs had higher resolving power, faster scanning times, and could be used at much lower kinetic energies [29].

RFQ reaction cells have also been applied to measure the masses and nuclear decay of short-lived nuclides. The reaction cells are used to cool, accumulate, and bunch ion beams for these applications. In 2007, Liu *et al.* modified the RFQ ion guide typically applied to positive ions to improve the transmission of more fragile negative ions [30]. The ions are decelerated to eV energies prior to injection into the quadrupoles. The modification of Liu *et al.* involved minimizing the buffer gas (also referred to as a cooling gas in this thesis work) that interacts with the ions before they are decelerated below the threshold energy for electron detachment. This RFQ ion cooler was used for the suppression of isobar contaminants in negative radioactive ion beams using laser photodetachment [31].

1.2.2.1 Isobars suppression by chemical reaction for AMS

Studies by Dunkin *et al.* found that NO_2 gas would react with S^-, creating neutral S, while transmitting Cl^- [32]. In an internal report from IsoTrace Laboratory, University of Toronto Kilius *et al.* and later Doupé *et al.* proposed using these ion-gas molecule reactions for isobar separation at keV energies in AMS measurements [33]. The multiple scattering resulting from these reactions reduced the ion beam quality and therefore the efficiency of the method [34]. In 2007, Litherland *et al.* proposed decreasing the energy of the ions from the sputter sources used for AMS down to eV energies [35]. To control these low energy ions, the use of a linear RFQ was proposed.

A prototype device using an RFQ reaction cell, called the ISA, was built at the IsoTrace Laboratory. This device contained a deceleration region, an RFQ column, and a reacceleration region [36, 37]. It was applied to the measurements of ^{36}Cl [38], and ^{90}Sr and ^{135,137}Cs [39].

This thesis uses a commercial ISA from *Isobarex Corp.*, which is upgraded from the IsoTrace Laboratory prototype with a segmented RFQ column to allow easy alterations to the configuration for testing [40]. The deceleration and reacceleration regions have been upgraded with a high vaccuum in that region and a lower vacuum surrounding the RFQ column. The column is also easily inserted and removed from the chamber, allowing for measurements along the beamline without the ISA. It should make it possible to study many new isotopes on the 3 MV AMS system but this work focuses on the benchmark case of ^{36}Cl.

1.3 Chlorine-36

Chlorine has two stable isotopes, ^{35}Cl and ^{37}Cl, and a naturally occurring radioisotope, ^{36}Cl. Table 1.1 includes the natural abundances and the masses of these three chlorine isotopes. ^{36}Cl has a half-life of 302 x 10^3 years with 98.1% of ^{36}Cl decaying via beta-minus to the ground state of ^{36}Ar [41]. The remaining 1.9% disintegrates by electron capture to the ground state of ^{36}S. A further 0.0015% beta-plus decays to the ground state of ^{36}S.

Isotope	Mass (AMU) [42]	Natural Abundance (%) [43]
^{35}Cl	34.9689	75.78
^{36}Cl	35.9683	trace
^{37}Cl	36.9659	24.22

Table 1.1: The masses and natural abundances of the three naturally occurring chlorine isotopes.

The two daughter products of ^{36}Cl are also its two stable elemental isobars. Table 1.2 includes the natural abundances, masses, and mass difference to ^{36}Cl of both of these isotopes. Both isobars are more abundant than the trace element ^{36}Cl and have very small mass differences with ^{36}Cl.

Isotope	Natural Abundance (%) [43]	Mass (AMU) [42]	Mass Difference to ^{36}Cl (AMU)
^{36}S	0.02	35.9671	0.0012
^{36}Ar	0.3365	35.9675	0.0008

Table 1.2: The natural abundances, mass, and mass difference to ^{36}Cl of the mass 36 stable isotopes.

1.3.1 Production of chlorine-36

^{36}Cl is a cosmogenic and subsurface radionuclide, naturally produced in the atmosphere and in the Earth's surface. It is produced in the upper atmosphere through interaction between cosmic rays and atmospheric ^{40}Ar or ^{36}Ar. Approximately 66% of the ^{36}Cl produced in the atmosphere is produced via the reaction [44]:

$$^{40}Ar + p \longrightarrow ^{36} Cl + n + \alpha \tag{1.13}$$

The remaining ^{36}Cl in the atmosphere is produced by the reaction [44]:

$$^{36}Ar + n \longrightarrow ^{36} Cl + p \tag{1.14}$$

The ^{36}Cl produced in the atmosphere is then deposited to the surface of the earth by precipitation or dry fallout, with the deposition varying with latitude [44]. In regions of increased precipitation, such as near the equator or coastal regions, there will be an increase in ^{36}Cl fallout. In coastal regions the ^{36}Cl/Cl ratio is diluted by marine aerosols, which contain no ^{36}Cl [45].

The ^{36}Cl in the Earth's surface is produced via spallation reactions, muon reactions, and thermal neutron activation [46]. The reactions from cosmic rays interacting with rocks exposed at the surface of the earth are:

$$^{39}K + n \longrightarrow ^{36} Cl + 2n + 2p \tag{1.15}$$

$$^{40}Ca + n \longrightarrow ^{36} Cl + 2n + 3p \tag{1.16}$$

These reactions dominate at high elevations where the majority of the cosmic ray flux is neutrons. At sea level and below, negative muon flux is comparable or greater than neutron flux and the following two muon reactions can occur [46]:

$$^{40}Ca + \mu^- \longrightarrow ^{36} Cl + \alpha \tag{1.17}$$

$$^{39}K + \mu^- \longrightarrow ^{36} Cl + p + 2n \tag{1.18}$$

In groundwater, thermal neutron activation with neutrons produced in the decay of U and Th may occur through the reaction [46]:

$$^{35}Cl + n \longrightarrow ^{36} Cl + \gamma \tag{1.19}$$

1.3.2 Applications of chlorine-36 measurement

The measurement of ^{36}Cl can be applied to many research areas: the production of radionuclides by cosmic rays, dating or tracing groundwater, paleoclimate studies (using ice sheets and glaciers), solar variability studies, bomb-peak records, exposure dating of rocks, studies of nucleosynthesis in stars, nuclear waste management, and neutron dosimetry of the Hiroshima bomb [1]. Many of these applications are geological or hydrological, with groundwater dating and tracing as the predominant application of ^{36}Cl measurement.

The ^{36}Cl half-life of 302 x 10^3 years means that it can be used to date groundwaters that are up to a million years old [45]. For groundwater dating and tracing, ^{36}Cl is measured relative to stable chlorine, with ^{36}Cl/Cl ratios in the range of 10^{-15} to 10^{-13} or higher [47]. The ^{36}Cl concentrations in water are low and therefore the radioactivity of groundwater samples is also low. The determination of the ^{36}Cl/Cl ratio, along with the decay of the initial concentration and groundwater recharge, may be used to date a sample. Between decay of ^{36}Cl to ^{36}Ar and recharge of ^{36}Cl from ^{35}Cl following Equation 1.19, the ^{36}Cl/Cl ratio will reach a secular equilibrium. This occurs after approximately five half-lives, after which only a minimum groundwater age can be determined. This dating is complicated by the multiple production mechanisms discussed in Section 1.3.1 and the variation in atmospheric production of ^{36}Cl based on latitude [47].

1.3.3 Measurement methods of chlorine-36

Two main techniques are used for the detection and quantification of radioisotopes: radiometric or mass spectrometry. The first of these techniques measures the characteristic radiation emitted when a radioisotope decays. The specific technique used is dependent on the type of radiation emitted (alpha particles, beta particles, gamma rays) and its energy. This type of detection works most efficiently for radioisotopes with short half-lives, leading to a higher decay frequency. It is unable to measure stable isotopes, so if measurement of both the radioisotope and its stable isotope is required, two different measurement techniques are required. It is also impractical to measure radioisotopes with small concentrations in a sample or radioisotopes with long half-lives ($>$ 1 x 10^6 years).

^{36}Cl decays via β^- decay, emitting a beta particle with an energy of 708.6 keV [48], with a half-life of 302 x 10^3 years. With these characteristics, liquid scintillation counting (LSC) is the most widely used radiometric technique. LSC involves mixing the sample with a liquid that fluoresces when exposed to radiation. The resulting emission of light is measured and the activity of the sample may be used to determine the concentration of the radioisotope.

For ^{36}Cl measurement, LSC has the advantage of low equipment costs [49]. While the sensitivity is low enough for ‘young’ water dating or for applications such as nuclear waste, it does not have the sensitivity for many common applications [45, 50]. For example, groundwater dating or tracing is often measuring samples with ^{36}Cl/Cl ratios in the range of 10^{-13} to 10^{-15}, which may result in single digit decays per day [47]. LSC also requires larger sample sizes (20 g of Cl for LSC compared to 2 mg of Cl for AMS), and has lower sample throughput than mass spectrometry techniques. A study of a ^{36}Cl/Cl dilution series for use as AMS standards found that LSC measurement of the samples in the range of 10^{-2} to 10^{-8} had uncertainties of ± 1-2% [51]. These samples are at ratios that are typically too high for AMS measurement. The sample with a ^{36}Cl/Cl ratio of 10^{-10}, which could be measured by both AMS and LSC was only measured by the latter with considerable effort. They required approximately 5 g of solution with uncertainty up to ± 3%. It was unable to measure the samples in the ^{36}Cl/Cl range of 10^{-11} to 10^{-13}.

Many forms of mass spectrometry exist, varying based on the type of mass analyzer used to separate ions (time-of-flight, magnetic sector, quadrupole, etc) and the ionization technique involved (ICP-MS, electron impact, chemical ionization, etc). AMS is the most widely used measurement technique for ^{36}Cl and is discussed in more detail in Section 1.3.3.1. Other mass spectrometry techniques are not able to sufficiently separate the stable isobars ^{36}Ar and ^{36}S for measurement of ^{36}Cl [52, 53, 54].

1.3.3.1 AMS of chlorine-36

AMS is capable of producing high ion currents from small sample sizes (approximately 2 mg of Cl), has high sample throughput, and has relatively low time requirements per sample. It is currently the only measurement technique capable of reaching ^{36}Cl/Cl ratios lower than 10^{-15}. This is necessary for many of the applications of ^{36}Cl measurement discussed in Section 1.3.2. The disadvantage comes from its cost and large space requirements. It is also more difficult to perform AMS measurements when stable, abundant isobars exist.

^{36}Cl has two stable elemental isobars with significantly higher abundances: ^{36}S with a natural abundance of 0.02% and ^{36}Ar with a natural abundance of 0.3365% [43]. With such low abundances for ^{36}Cl, any interfence from these isobars can have a large effect on analysis or overwhelm the gas ionization chamber (GIC) with counts. ^{36}Ar^{-} is either not produced in the ion source or is not stable enough to make it to the final detector [55]. However, ^{36}S is still a significant problem for measurement of ^{36}Cl.

To reduce the presence of ^{36}S in AMS measurement of ^{36}Cl, partial purification is first performed on all samples being studied. This involves either removing some S by passing the AgCl solution through resin columns or precipitating S as $BaSO_4$ [56]. The Cu and Al targets typically used in AMS may have traces of S high enough to interfere with the measurement of ^{36}Cl. To minimize this contamination, many laboratories surround their AgCl targets with AgBr with a low S content [57].

Even with partial chemical purification, some sulfur will remain in the spectra, possibly from the Cs^+ beam used to ionize the sample or from residual gas in the system. Only large accelerators, with terminal voltages of 5 MV or higher, are capable of measuring ^{36}Cl without additional isobar suppression techniques [58]. The high energy accelerators produce larger yields of ^{36}Cl in higher charge states. ^{36}Cl is typically measured on these high energy machines in the 5+ or 7+ charge state [57]. The resulting high energy of the beam (approximately 30 MeV to 105 MeV) allows for sufficient separation between the ^{36}Cl and ^{36}S in the GIC. The laboratories measuring ^{36}Cl on 5 MV accelerators are only capable of these measurements due to advances in technology, including updates to the entrance windows of GICs [58]. Additional high energy techniques for the removal of ^{36}S include differential energy loss in a gas-filled magnet [59] and, at extremely high energies (performed on a 25 MV tandem accelerator), the complete stripping of ^{36}Cl and ^{36}S to $^{36}Cl^{17+}$ and $^{36}S^{16+}$ [60]. This work using a 25 MV tandem accelerator reported a ^{36}Cl/Cl ratio of $(5 \pm 3) \text{ x } 10^{-16}$, the highest sensitivity for ^{36}Cl at that time [60]. Since these measurements in 2007, other laboratories have reported similar capabilities [61, 62]. The current chemical preparation and high energy requirements for the measurement of ^{36}Cl without the interference of ^{36}S mean that it is one of the most expensive isotopes to measure by AMS.

The ILIAMS technique, mentioned in Section 1.1.1, is well suited to the measurement of ^{36}Cl because laser photodetachment takes advantage of the difference in electron affinity between an isotope and its isobar. The electron affinity of ^{36}Cl (3.6 eV) is 1.5 eV greater than that of ^{36}S (2.1 eV). The ILIAMS has shown a reduction of more than 10 orders of magnitude in ^{36}S counts [63]. VERA is now routinely measuring ^{36}Cl on a 3 MV accelerator [17].

Using the ISA to suppress the ^{36}S through ion-gas molecule electron transfer reactions has also been explored for the measurement of ^{36}Cl on prototype instruments. The history of the technique and the ISA are discussed in Section 1.2. This work details the integration of the *Isobarex Corp.* ISA into the existing 3 MV André E. Lalonde accelerator mass spectrometry (AEL-AMS) system at the University of Ottawa. The transmission of the ISA is characterized before it is applied to the measurement of ^{36}Cl standards and groundwater samples.

Chapter 2

Integration of the Isobar Separator for Anions into the 3 MV AMS system at the AEL Laboratory

The research work detailed in this thesis involves the construction of an additional beamline, referred to as the Research Line, connected to the main beamline of the AMS setup at AEL-AMS Laboratory. The main components of the original beamline and the Research Line, including the electronic controls, are detailed in this chapter.

2.1 Accelerator Mass Spectrometry at A. E. Lalonde

The 3 MV AMS system was installed in the Advanced Research Complex at the University of Ottawa in 2014 [64]. It replaced the University of Toronto IsoTrace Laboratory as the only remaining AMS facility in Canada. This system was designed for multi-element analysis, capable of analyzing isotopes such as ^{10}Be, ^{14}C, ^{129}I, and actinides. The installed system, indicated as the Main Line in Figure 2.1, was built by High Voltage Engineering Europa BV (HVEE). This main line includes the basic functions of a typical tandem AMS system, with a low energy (LE) mass spectrometer before the accelerator, the 3 MV accelerator, and a high energy (HE) mass spectrometer after the accelerator. In addition to the major components labelled in Figure 2.1, there are a number of focusing lenses, steerers, apertures, and slits.

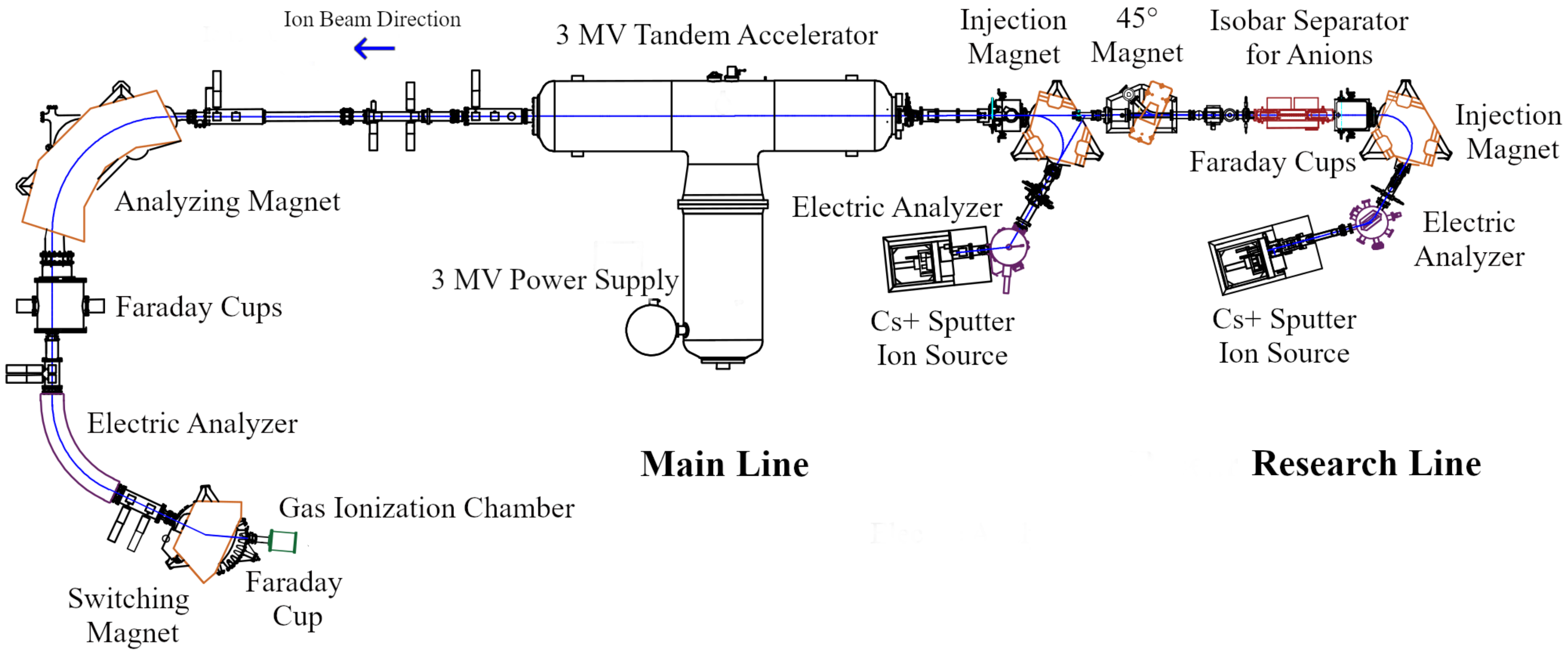

Figure 2.1: A schematic overview of the A. E. Lalonde AMS accelerator system with two injection lines. The main line includes the leftmost source, electric analyzer and injection magnet. The Research Line extends from the rightmost sputter source to the entrance of the main line injection magnet. Either line can inject into the 3 MV accelerator and the high energy spectrometer.

2.2 Low Energy Mass Spectrometer

The low energy mass spectrometer of the main line on the 3 MV system can be seen in Figure 2.1. This line is not used in this work but is an important part of the 3 MV AEL-AMS system. Section 2.2.1-Section 2.2.3.1 detail the major components of this line.

2.2.1 Ion source

The ion sources on the 3 MV system are HVEE SO-110C Cs^+ sputter ion sources [65]. Because of Cs's high-efficiency negative ion formation, Cs^+ sputter ion sources can provide the stable currents required in AMS measurements [66]. Measurement of volatile isotopes, like Cl, also require low source memory and background. The SO-110C version of the source improves the sputtering area over previous versions; the sputter region is decreased to the sample area thus reducing contamination from the copper targets [65].

The Cs reservoir is externally mounted to the source body. The reservoir heats Cs to a vapour which is injected into a shroud with holes that spray Cs atoms onto the ionizer. The Cs is ionized into Cs^+, which is accelerated towards the target using a voltage set by the user (Target Voltage). The Cs^+ liberates negative ions from the samples which are accelerated away from the target. They are further accelerated by another user-set voltage (Extraction Voltage). Typical AEL-AMS measurements run with a target voltage of 7 kV and an extraction voltage of 28 kV, resulting in a 35 keV anion beam.

Chemically-prepared powdered samples are pressed into copper targets that are inserted into a 200 sample wheel. This wheel is mounted into the source carousel shown in Figure 2.2. A pneumatic cylinder is used to inject the targets into the ion source.

2.2.2 Electrostatic analyzers

The electrostatic analyzer (ESA) acts as an energy filter that will only transmit anions of a specific energy. It consists of two spherical or cylindrical plates with a potential difference, V_{ESA}, across them. V_{ESA} is determined by the kinetic energy of the beam, E, the separation of the two plates, d, the radius of curvature, ρ, and the charge state of the beam, q:

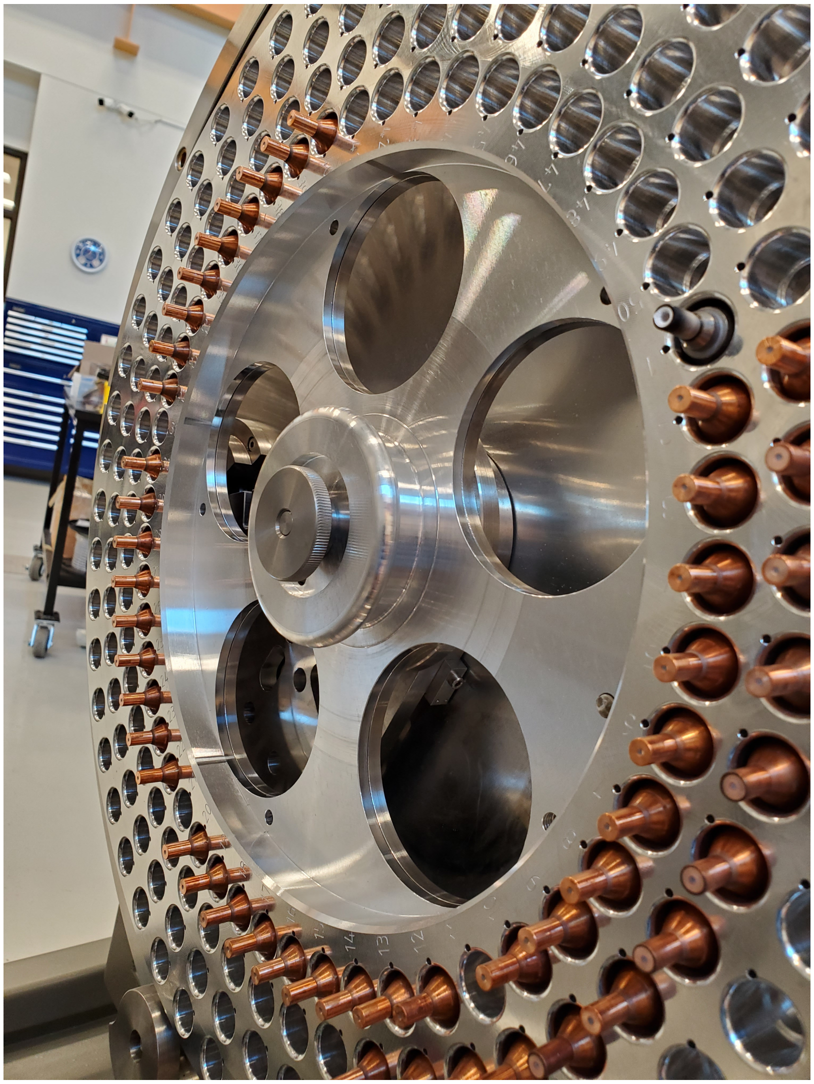

Figure 2.2: The High Voltage Engineering SO-110C 200 sample wheel on the Research Line with inserted copper targets.

$$V_{ESA} = \frac{2dE}{\rho q} \tag{2.1}$$

The voltage is typically evenly divided between the two plates, minimizing the required voltage from a power supply and reducing aberrations from the fringe fields. For negative ions, the inner plate is held at a positive voltage and the outer at the negative of that value.

An ESA is often used in both the LE mass spectrometer and HE mass spectrometer, as shown in Figure 2.1.

2.2.3 Magnetic analyzers

After analysis by the ESA, the beam is injected into a 120° injection magnet. The ions, with varying masses, will have the same kinetic energy from the ESA but different momenta and will be separated by their momenta. The magnetic field, B, required to inject ions with mass M is given by:

$$B = \frac{\sqrt{2ME}}{\rho q} \tag{2.2}$$

where E is the kinetic energy, ρ is the radius of curvature for the magnet, and q is the charge state of the beam. The 120° injection magnet has a bending radius of 0.455 m and a bending power of 12 MeV-amu [64, 67]. With the beam from the ion source at 20 keV, the bending power of the magnet can accommodate ions with a mass up to 600 amu. The injection magnet is required to inject all isotopes of interest. However, magnetic fields are slow to change and hysteresis makes tuning more difficult. To avoid hysteresis during tuning and analysis, a Hall probe is used to control the magnetic field [68]. To allow for rapid changes between the isotope being injected, the magnetic field is held constant while a voltage is placed on the vacuum chamber of the magnet to accelerate or decelerate the ions to the correct energy for the magnetic field. This isotope selection process is known as 'bouncing' and is further discussed in Section 2.2.3.1.

2.2.3.1 Isotope Selection Electrode ('Bouncer')

Sequential injection or 'bouncing' is used to measure two or more isotopes. On this injector magnet, a positive or negative voltage can be applied to the entire vacuum box inside the magnet. This changes the momentum of the ions when they pass through the magnet and restores the original momentum when the ion leaves the magnet. The voltage is cyclically changed to inject all masses of interest. The voltage control on the HVEE bouncer allows for both fast sequential injection (FSI) and slow sequential injection (SSI) [69].

In both bouncer modes, voltages are set to allow the injection of different isotopes. The magnetic field is tuned to accommodate this voltage offset for the rare beam. Because the magnetic field in Equation 2.2 will remain constant, the voltages required for the stable beam are calculated based on just the masses, the energy of the beam, and the energy change in the beam resulting from the small voltage offset used for the rare beam:

$$V_{stable} = \frac{\frac{M_{rare}}{M_{stable}}(\frac{q_{stable}}{q_{rare}})^2(E_{rare} + V_{rare}q_{rare}) - E_{stable}}{q_{stable}} \tag{2.3}$$

FSI uses a cycling frequency of 100 Hz, with a measurement time of 9.75 ms on the rare beam and 100 μs on the stable beam. During the work completed in this thesis, this was not adjustable by the user. The user can adjust the gate delay of the detector, the flight time delay for Faraday cup measurements, and the wait time between switching voltages. For the 3 MV system, the typical value for a gate delay on the GIC and for a delay on Faraday cup measurement is 250 ns. A delay of 300 μs is also applied to allow each voltage to settle. During this time, an ultra-fast beam blanker is used to stop the beam [69].

SSI mode uses the same adjustable parameters as FSI mode but permits the adjustment of many components on the system, e.g. lenses, steerers, and even the accelerator terminal voltage. It can include up to five rare radioisotopes but only one stable isotope. It takes 7.5 s to switch between isotopes. The amount of time spent measuring the isotopes is adjustable by the user on the seconds scale. Typical settings for the 3 MV AEL-AMS system use 2-5 s on stable beams and 10-100 s on the rare radioisotopes depending on typical count rates.

DC mode is also available, allowing for the continuous injection of one isotope. However, a batch analysis of multiple samples requires the use of the bouncer. It is possible to set all bouncer voltages to the same voltage to inject only one isotope.

2.3 The Research Line

The Research Line, shown in Figure 2.1, is a new injection line added to the previously installed 3 MV AMS system at the AEL-AMS Laboratory. The line is comparable to a typical AMS LE mass spectrometer with the exception of a novel component, the ISA. This is a commercial version of the earlier proof-of-principle system developed by *Isobarex Corp.* [40] in collaboration with the IsoTrace Laboratory [35, 38].

The Research Line has the same SO-110 Cs$^+$ sputter ion source discussed in Section 2.2.1. However, work completed in this thesis used a target voltage of 7 kV and an extraction voltage of 13 kV, resulting in a 20 keV anion beam. The reason for these lower voltages are discussed in Section 2.3.1. The Research Line has a 45° spherical ESA with a radius of 0.406m [70]. The ESA is rotatable, allowing for the addition of a second source. The injection magnet prior to the ISA is the same as the 120° injection magnet of the main line. At the time of writing, the power supply of the main line injection magnet is temporarily disconnected from the main line and connected to the Research Line injection magnet when it is used. To eliminate any possible remnant magnetic field on the injection magnet of the main line, a degaussing unit is connected during accelerator runs using the Research Line.

Following the ISA is a 45° magnet with a radius of 1.32 m. An electron multiplier system may be added at the end of the 45° exit line of this magnet to enable stand-alone analysis of the beam when the main injection line is in use for other analyses. During analysis through the entire AMS system the field of the magnet is set to zero.

The voltage settings for the experimental work detailed here can be found in Table C.1 of Appendix C.

2.3.1 The Isobar Separator for Anions

The ISA is an RFQ reaction cell that uses selective anion-gas molecule reactions to remove isobars. It decelerates a keV beam from the ion source down to eV energies to facilitate electron transfer and ion dissociation reactions within the RFQ-lined reaction cell. The ISA integrated into the Research Line is a commercial version manufactored by *Isobarex Corp.* [40], shown in the lower panel of Figure 2.3.

The ISA consists of deceleration optics, an RFQ ion guide, and acceleration optics in a single, 1 m long vacuum chamber. A schematic and photo are given in Figure 2.3. To facilitate the deceleration of the incoming ions, all components in the ISA (referred to as the 'deck') are held at a voltage slightly more positive than the sum of the ion source target and extraction voltages (both negative). An Einzel lens is included in both the deceleration and acceleration optics to focus the respective incoming and outgoing beams.

The ISA vacuum chamber is differentially pumped by two triple channel *Leybold Turbovac 400/300/50 iC* pumps, with the 300 L/s ports pumping each end of the central section and

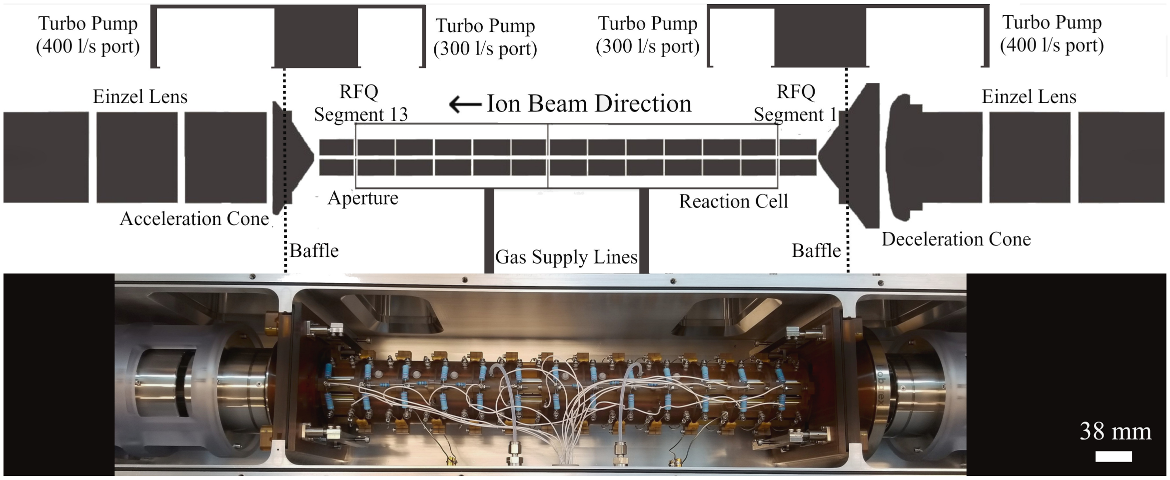

Figure 2.3: The top panel shows a schematic drawing of the ISA column. The bottom panel shows the ISA column within its vacuum chamber.

the 400 L/s ports pumping the higher vacuum in the deceleration and acceleration sections, as indicated in Figure 2.3. These maintain the pressure of the central cavity in the range of 1 x 10^{-5} to 1 x 10^{-4} mbar when reaction and cooling gases are admitted into the RFQ ion guide and leak out through the cell entrance and exit apertures. The 400 L/s high-capacity vacuum port are used to maintain the deceleration and acceleration optic cavities at pressures of 1 x 10^{-6} mbar.

The RFQ ion guide is composed of 13 modules, each containing a 36 mm long quadrupole with space at the end for an aperture plate. With the guide assembled, the rods are separated from each other and from aperture plates by a 2 mm gap. Together they form a 496 mm continuous segmented ion guide. Because of the modular design, the location, number, and size of aperture plates can be varied. The configurations studied in this work are detailed in Section 3.1.

Two RF amplifiers are used: one to drive the first 7 segments, the second, the last 6 segments. The frequency is fixed at 2.5 MHz and the RF amplitude is adjustable over 100 to 5000 peak-to-peak RF voltage, V_{pp}. This ensures that the system can achieve a confinement value of q_2=0.3 up to 275 amu, where q_2 is the dimensionless Mathieu parameter derived from the solution of the Mathieu equations that describe the motion of an ion in the RFQ [24], given by the equation:

Component	Value
Deceleration Lens 1	0 V
Deceleration Lens 2	-20,000 to 0 V
Deceleration Lens 3	0 to 1000 V
Deceleration Cone*	-6000 to 6000 V
RF quadrupole (peak-to-peak)*	100 to 5000 V_{pp}
RFQ offsets*	-250 to 250 V
Apertures*	-250 to 250 V
Acceleration cone*	-6000 to 6000 V
Acceleration lens 1	0 to 1000 V
Acceleration lens 2	-20,000 to 0 V
Acceleration lens 3	0 V

Table 2.1: The voltage ranges for the ISA components. *Values are relative to the deck voltage

$$q_2 = \frac{qV_{pp}}{2m(\pi f r_0)^2} \tag{2.4}$$

In Equation 2.4 q is the charge, m is the mass of the anion, f is the radiofrequency, and r_0 is the inscribed radius of the quadrupole electrodes. The r_0 of this model of the *Isobarex* ISA is 6.9 mm. The RFQ segments are capacitively coupled to each other for their RF connections, but each can be raised individually with a DC potential from -250 V to 250 V relative to the high voltage deck. An axial field is generated between segments to maintain coherent movement of the ions through the gas cell. Table 2.1 contains the voltage ranges of the ISA components.

The introduction of cooling and reaction gases to the ISA cell is controlled by two separate mass flow controllers (Horiba SEC-Z500X), each programmable over the range 0-10 standard cubic centimeters per minute (SCCM).

2.3.1.1 User interface

The user interface for the ISA, shown in Figure 2.4, is on an ISA control computer separate from the control computer for the rest of the 3 MV system. The ISA deck voltage, deceleration Einzel lens, and acceleration Einzel lens are controlled by the 3 MV system computer (indicated in Figure 2.5). The ISA communicates with its control computer through a 5G

Wi-Fi bridge. A Wi-Fi repeater is located on the ISA deck and another is located in the electronics enclosure below the ISA at ground potential; the two form a stable link.

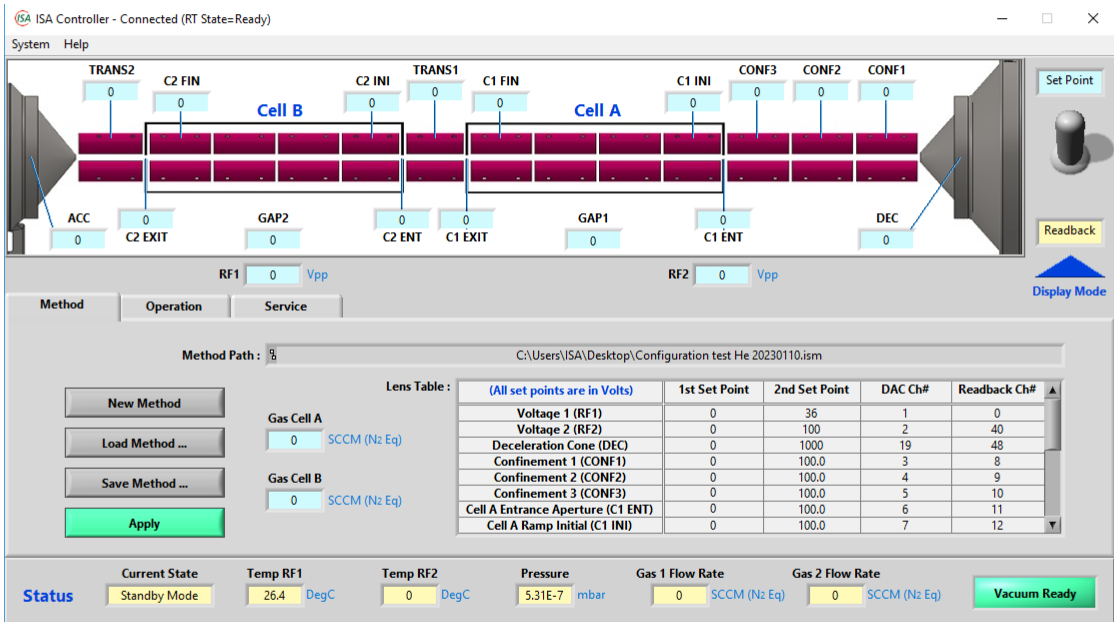

TRANS2: 0
C2 FIN: 0
C2 INI: 0
TRANS1: 0
C1 FIN: 0
C1 INI: 0
CONF3: 0
CONF2: 0
CONF1: 0
ACC: 0
C2 EXIT: 0
GAP2: 0
C2 ENT: 0
C1 EXIT: 0
GAP1: 0
C1 ENT: 0
DEC: 0
RF1: 0 Vpp
RF2: 0 Vpp

Method Path : C:\Users\ISA\Desktop\Configuration test He 20230110.ism

Gas Cell A: 0 SCCM (N2 Eq)
Gas Cell B: 0 SCCM (N2 Eq)

Lens Table :

(All set points are in Volts)	1st Set Point	2nd Set Point	DAC Ch#	Readback Ch#
Voltage 1 (RF1)	0	36	1	0
Voltage 2 (RF2)	0	100	2	40
Deceleration Cone (DEC)	0	1000	19	48
Confinement 1 (CONF1)	0	100.0	3	8
Confinement 2 (CONF2)	0	100.0	4	9
Confinement 3 (CONF3)	0	100.0	5	10
Cell A Entrance Aperture (C1 ENT)	0	100.0	6	11
Cell A Ramp Initial (C1 INI)	0	100.0	7	12

Current State	Temp RF1	Temp RF2	Pressure	Gas 1 Flow Rate	Gas 2 Flow Rate
Standby Mode	26.4 DegC	0 DegC	5.31E-7 mbar	0 SCCM (N2 Eq)	0 SCCM (N2 Eq)

Figure 2.4: The user interface for the *Isobarex* Isobar Separator for Anions.

The user interface allows you to adjust the voltage on each component within the ISA with a resolution of 0.1 V and the gas flow has a resolution of 0.01 SCCM. The user interface allows the user to read back the voltage. The temperature of the RFQ and the pressure of the vacuum chamber can be monitored. The settings can be saved and recalled later.

2.3.1.2 Two Einzel lens focusing

The column of the ISA may be removed from the vacuum chamber and the Research Line can be used as an injection line without the ISA. The alignment of the ISA is controlled by the baffles when clamped in place in the vacuum chamber. When the clamps are released, the ISA may easily slide in and out of the chamber. The Einzel lens pair remaining in the ISA vacuum chamber may be used in telescopic mode to focus the beam as a single Einzel lens [71, 72].

2.3.2 Electronic Controls

Figure 2.5 shows a schematic of the Research Line and the power supplies that control them. These power supplies also connect to HVEE controlled area network (CAN)nodes, programmable logic controllers used to monitor and control elements in a local area on the 3 MV system. CANnode boxes have multiple functions, including Digitial and Analog Input and Output. They have fibre links to the 3 MV control computer. As discussed in Section 2.3.1.1, the ISA components are controlled by a separate computer.

In Figure 2.5 red dashed lines indicate the output on components connected to power supplies. Blue solid lines indicate an input and output (I/O) connection between components. Finally, a green dash-dotted line indicates that an interlock is connected to that component.

The voltage of the majority of the components are controlled by Glassman EH or ER Series 100 Watt high voltage DC power supplies. The ISA deck voltage is controlled using a negative 0-40 kV power supply, the central electrodes of each Einzel lens is controlled using a negative 0-30 kV power supply, and the ESA is controlled by two ± 20 kV power supplies. The steerers are controlled by homemade power supplies from 0-1000 V. The injection magnet uses a pair of 0-70 V, 0-90 Delta Elektronika power supplies. The final Einzel lens has a -30 kV power supply attached to its main body. Due to an external high voltage connection between the electrodes and power supplies, the voltage is currently limited to less than 20 kV. This will be modified to reach the normal operation voltage of the ion source. In turn, this limited the incoming beam energy to -20 keV despite a deck voltage tested to -40 kV.

2.3.3 Additional components

The Research Line also contains steering electrodes, focusing electrodes, and slits, indicated in Figure 2.6. At the source, there is an Einzel lens for focusing the beam into the ESA. Following the Einzel lens there are a pair of x- and y-steerers. An additional pair of x- and y-steerers are located between the ESA and the injection magnet. Just prior to these steerers, at the image plane of the ESA and the object point of the injection magnet, are

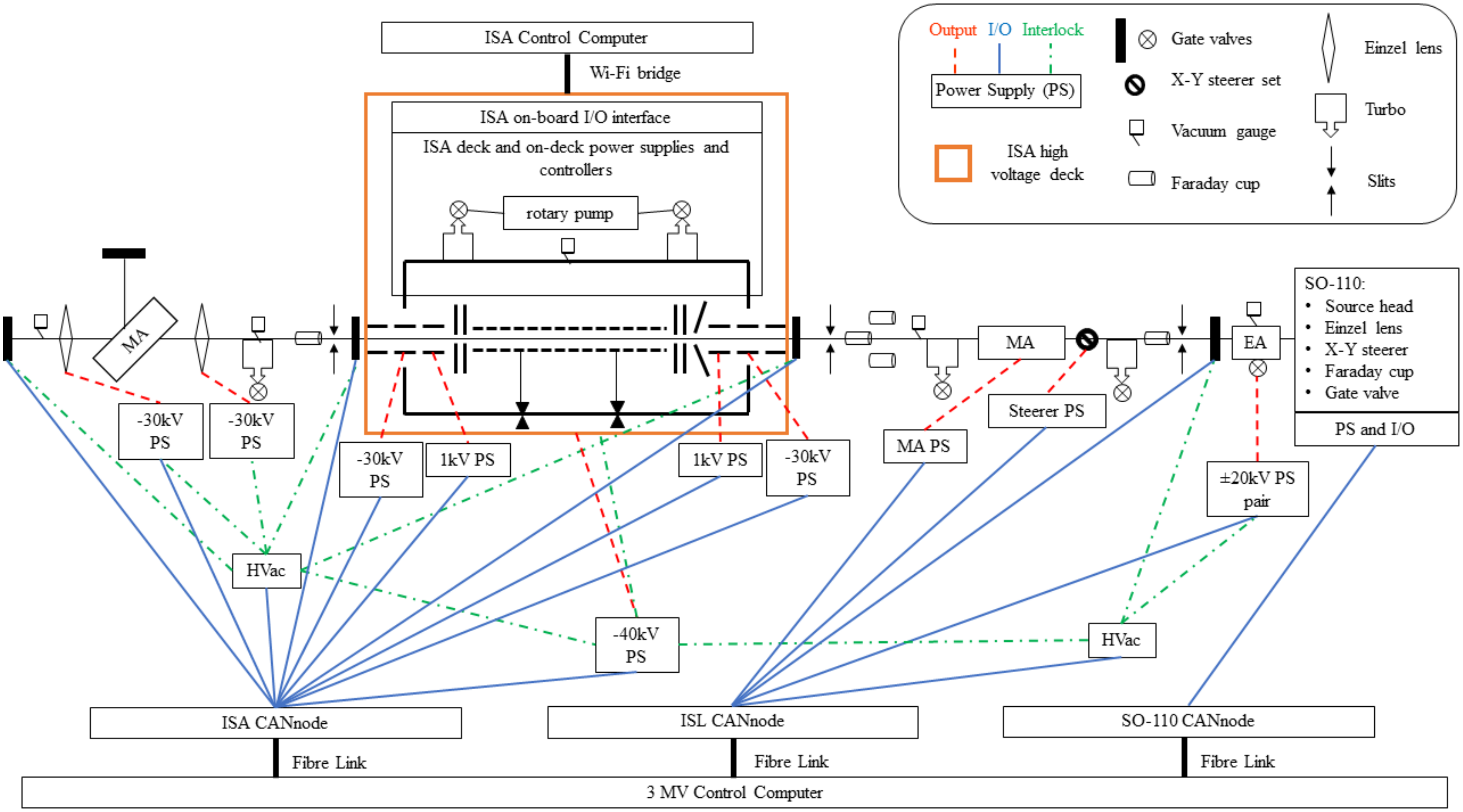

Figure 2.5: The electronic controls and logistics of the Research Line. The ISA deck is indicated by an orange box. A simplified schematic of the ISA is included. The schematic is not to scale.

a set of adjustable x- and y-slits. Following the injection magnet, there is an injectable 3 mm aperture and a pair of adjustable x-slits, located at the image of the 120° magnet and which define the object point of the ISA decelerating lens. These are followed by an insertable Faraday cup, addressed in detail in Section 2.6.1. Following the ISA, are a pair of adjustable x- and y-slits, which define the object point of the ISA acceleration lens and are followed by another insertable Faraday cup. Next comes an Einzel lens which is kept externally grounded for analysis on the full AMS system and will be used to focus the beam during analysis with the 45° magnet discussed in Section 2.2.3. The addition of adjustable x- and y-steerers following the Einzel lens are planned for analysis with the 45° magnet. Finally, an Einzel lens is located following the 45° magnet for focusing into the main line.

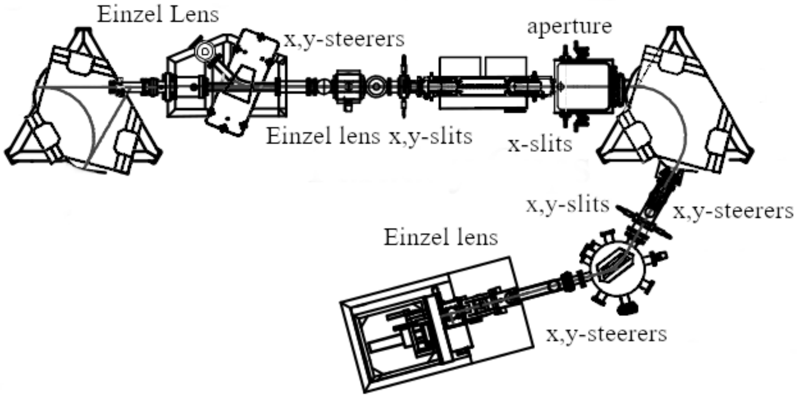

Figure 2.6: A schematic overview of the Research Line. The locations of steering electrodes, Einzel lenses, slits, and apertures are indicated on the line.

2.4 3 MV tandem accelerator

The HVEE 3 MV tandem is considered a medium-sized system; small systems have terminal voltages less than 1 MV compared to large systems with terminal voltages 5 MV or greater [73]. A high voltage, up to +3.0 MV, is applied to the centre of the accelerator terminal and is distributed evenly, using resistor divider networks along the electrodes of the low and high energy vacuum tubes. The anion beam is accelerated by this electric potential. When the beam has reached the terminal, it is injected into a stripper canal filled with argon gas. Collisions with the gas strip the anions of some of their electrons, resulting in a cation beam. The charge state of the beam can then be selected during tuning of the HE mass spectrometer components. A charge state of greater than or equal to 3+ will dissociate molecular isobars that energy and mass analysis have not removed [2]. The cation beam is then accelerated away from the accelerator terminal and injected into the HE mass spectrometer.

2.5 High energy mass spectrometer

Following the accelerator in Figure 2.1, there is an additional analyzing magnet, an ESA, and a switching magnet. The analyzing magnet separates the beam by momentum in the same way as described in Section 2.2.3 but in this case, no bouncer is necessary. It is a 90° magnet with a radius of curvature of 2000 mm and a bending power of 351 MeV-amu [64]. The magnet is tuned to allow the rare beam to travel the full 90° while the stable isotopes are dispersed at different angles into the Faraday cup box detailed in Section 2.6.1.

The HE ESA separates a beam by energy as described in Section 2.2.2. A 65° cylindrical ESA with a radius of curvature of 1.700 m, a plate separation of 0.040 mm and an energy resolution of 3000 can be seen following the Faraday cup box in Figure 2.1.

Finally, a switching magnet with nine detection ports follows the ESA. The GIC is connected to the 20° port, with no other ports currently being used. This magnet further minimizes the background entering the detector.

2.6 Detectors

Two types of detectors are currently used on the 3 MV AEL-AMS system based on the sensitivity required. Faraday cups (Section 2.6.1) are used to measure stable beams with high currents. The rare radioisotope, with single atom counts, are measured using a GIC (Section 2.6.2). Ports are available after the switching magnet for additional detectors or analysis lines.

2.6.1 Faraday cups

Faraday cups are metal cups that capture the charged particle beam and record the resulting current. The number of ions can be determined based on the charge state of the beam. The Faraday cups are distributed throughout the beamline to measure the current of the stable isotopes during tuning. They are then retracted during measurement to allow the beam to pass through for final measurement.

In the HE end of Figure 2.1, a Faraday cup chamber contains two off-axis adjustable Faraday cups, an inner and an outer cup. Similarly, following the injection magnets of the Research Line and the LE end of the main line have Faraday cup boxes with off-axis adjustable Faraday cups. The position of the Faraday cups are optimized to capture the stable beam during the measurement of the rare isotope. The two HE cups allow measurement of two stable beams in cases where two stable isotopes are available, for example, the measurement of ^{12}C and ^{13}C when studying ^{14}C. These Faraday cups have higher precision than the on-axis cups along the beamline and are typically used to calculate the isotopic ratio of samples. In the case of chlorine measurements in this work, the Research Line off-axis Faraday cups are used for the stable ^{35}Cl and ^{37}Cl beams prior to injection into the ISA. The reasons for this unusual stable beam measurement technique are discussed in Section 4.2.

2.6.1.1 Electron suppression

When the anions of the beam hit the surface of the Faraday cup secondary electrons will be liberated from the material or the anions themselves. If these secondary electrons are backscattered out of the Faraday cup, the current read from the Faraday cup will decrease and therefore be less accurate. Multiple techniques are used to reduce the losses from backscattered secondary electrons [74]. The most common of those techniques is the use of a suppression plate at the entrance of the Faraday cup. A negative voltage is placed on the suppression plate to repel the electrons back into the cup without repelling the incoming higher energy beam. Electron suppression is applied to all Faraday cups along the main 3 MV line and was added to all of the Faraday cups on the Research Line. To determine the required voltage, the current was measured in the cup while the voltage on the suppression

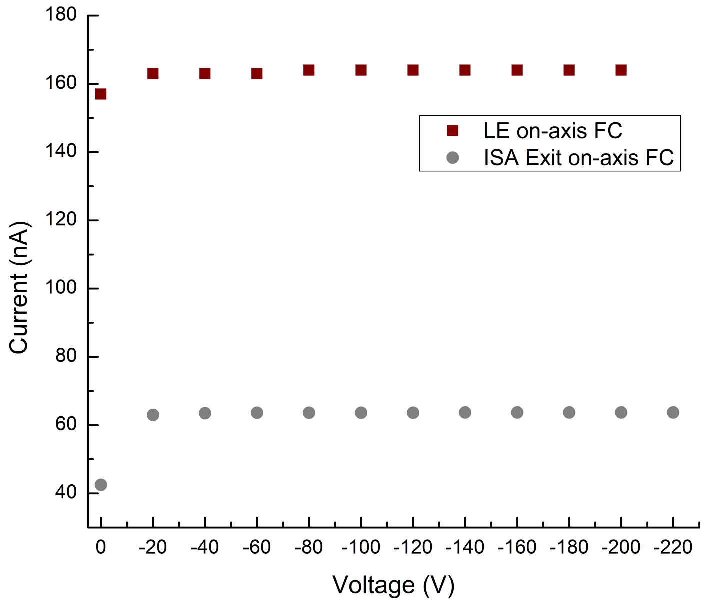

Figure 2.7: The voltages required for electron suppression on the ISA entrance (LE on-axis) and exit (ISA exit on-axis) Faraday cups. The LE on-axis Faraday cup is indicated by the square symbols. The ISA exit on-axis Faraday cup test is indicated by the circle symbol. The current increase can be seen after -20 V is applied to the suppression plate.

plate was gradually increased, shown in Figure 2.7. Setting the voltage on the suppression plate showed an immediate increase in the current in both cups. A voltage of -140 V was selected for the final suppression voltage, as it showed a small increase over lower voltage settings but no improvement was seen at higher voltage settings.

2.6.2 Gas ionization chamber

Rare radioisotopes are measured by single-atom counting in the GIC at the end of the beamline. Before entering the detector, the beam passes through a 75 nm thick Si_3N_4 foil window. This isolates the isobutane gas that fills the GIC from the vacuum of the line. The cation beam collides with the isobutane, producing ion-electron pairs. These electrons are collected on anodes within the detector. The detector on the 3 MV AEL-AMS system has two anodes, shown in Figure 2.8, with the anodes kept at approximately +300 V and the cathode at approximately -200 V. Additional anodes in GIC detectors can be used to

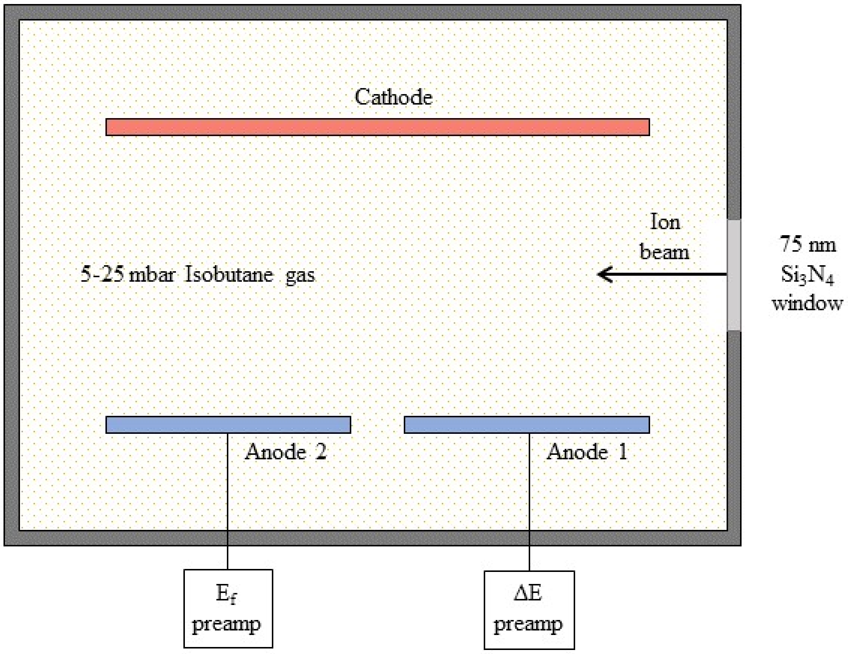

Figure 2.8: A schematic of the internal set up of a gas ionization detector. The beam enters through a 75nm thick Si_3N_4 window. The detector is filled with 5-25 mbar isobutane gas (15 mbar for ^{36}Cl).

provide extra discrimination between isobars for systems with higher energy accelerators. The energy lost by the ions in the detector corresponds to the number of electrons measured by the first anode. The shower of electrons that hit the anode causes an electronic pulse, the area of which is proportional to the energy lost under the anode. The second anode measures the final energy of the ions.

The pressure in the GIC is chosen based on the mass of the isotope being studied, the energy of the ions, and the SRIM stopping tables for isobutane [75]. The pressure should be high enough that the ions do not reach the end of the second anode.

In the energy spectrum, the final energy of the ions from the second anode is presented on the y-axis and the x-axis measures the energy loss measured from the first anode. FAST ComTec GmbH's MPANT software [76] allows the user to freely draw the region of interest (ROI). Only the ions that fall within the ROI are included in the count for the rare radioisotope of interest. Counts outside of the ROI are considered background. The software is then able to report a ratio of the stable isotopes measured by the Faraday cups discussed in Section 2.6.1 and the rare radioisotope counted by the GIC.

Chapter 3

Characterization of the Isobar Separator for Anions

The configuration of apertures within the ISA cell, the selection of the cooling and reaction gases, and the voltage and RF settings of the ISA components need to be characterized prior to its application to standards and samples. These characteristics will depend on the isotope of interest; this work studied the trace isotope, ^{36}Cl. For the initial measurements, small currents (100-300 nA) of ^{35}Cl and ^{37}Cl were used to represent the behaviour of ^{36}Cl because it is not practical to characterize the ISA using counts from a rare radioisotope. The targets were a mixture of AgCl and Nb at a 1:3 volume. Details on the preparation of targets can be found in Appendix B.

The main goals of the characterization of the ISA are to determine the conditions that provide the highest transmission of Cl anions while also suppressing the S anions. It is important that the transmission of Cl anions remains high when studying trace amounts because low transmission will lead to a decrease in count rate, precision, and accuracy. Low transmission may eliminate the possibility of measuring lower ratio samples that are often found in ^{36}Cl applications. These lower counts may also necessitate an increase to the counting time required for each target and thus a large increase in overall accelerator time.

3.1 Cell configuration evolution

As mentioned in Section 2.3.1, the *Isobarex* ISA consists of 13 RFQ modules, which can be altered to provide various cell configurations. Four main configurations were studied in this work. Schematics of these configurations, referred to as 1, 2, 3, and 4, are shown in Figure 3.1. The configurations differ in the location and number of apertures within the cell. The acceleration and deceleration optics and the number of RFQ segments remained constant throughout the configuration tests. The transmission of $^{37}\mathrm{Cl}^-$ through each configuration was tested and this parameter was used to determine the viability of that configuration. These configurations changes were completed in tandem with the tests discussed in Section 3.2, which tests the transmission of Configuration 3 in vacuum, with a cooling gas, and with a reaction gas filling the ISA cell. Therefore, many of these transmission tests look at transmission either in vacuum or with He gas.

3.1.1 Configuration 1

Configuration 1, shown in Figure 3.1a), uses four apertures to create a separate cooling and reaction cell. The first aperture was placed after three RFQ segments. An additional aperture was placed four RFQ segments after the first; these four segments make up the cooling cell. Following another RFQ segment there is an aperture, which makes the entrance to the reaction cell. The reaction cell is four RFQ segments long, with an aperture making the exit. There is one RFQ segment prior to the acceleration optics. Reaction and cooling gases, discussed in Section 3.2, are feed separately into their respective cells. The cells not boxed in by an aperture are open, such that they are being pumped by the vacuum system. Tests were completed using apertures with a 2.5 mm diameter.

In this configuration, tests did not result in transmission through the ISA for either $^{12}\mathrm{C}_3$ or $^{37}\mathrm{Cl}$ anions. To determine where the current was lost, tests were completed using Faraday cups or current measuring plates inside of the ISA. Because these devices were inside the high voltage deck of the ISA, the ammeter used to measure the impinging current also needed to be at this high voltage. They were not electron suppressed.

The first test removed the RFQ segments from the ISA to allow for placement of a Faraday cup directly after the deceleration cone. The ratio of the current entering the Faraday cup to the current measured before the ISA vacuum chamber was 90% or higher. This implies that the majority of the current was entering the first RFQ segment, as expected.

a) Configuration 1

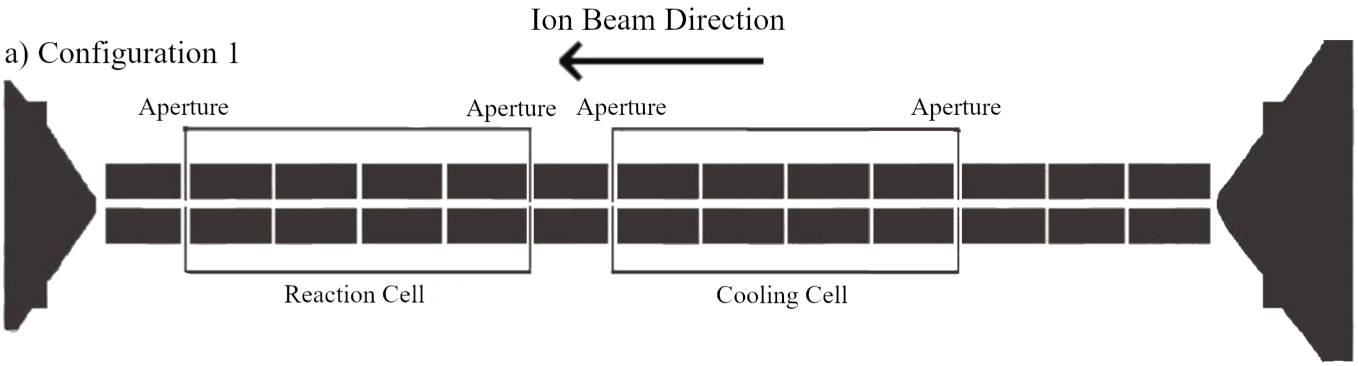

b) Configuration 2

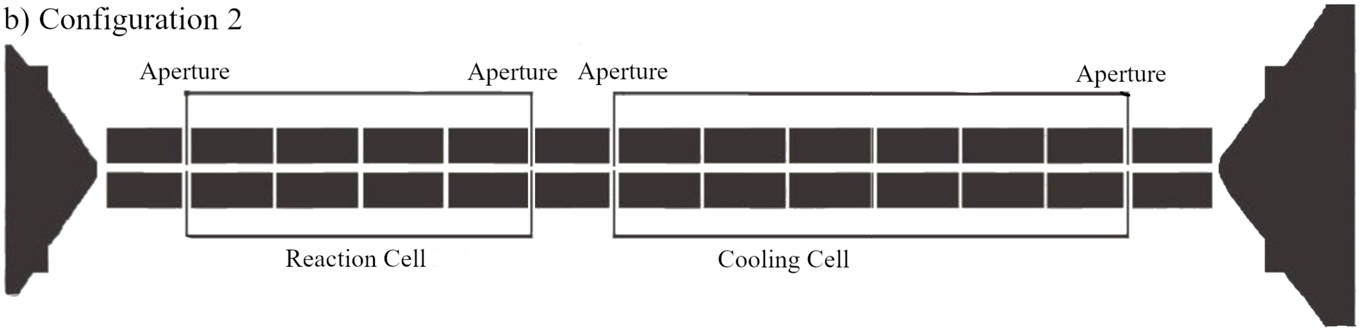

c) Configuration 3

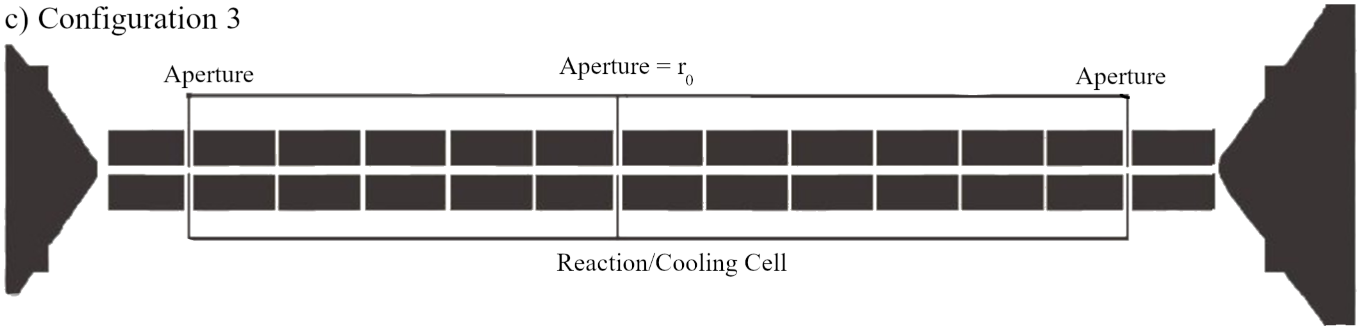

d) Configuration 4

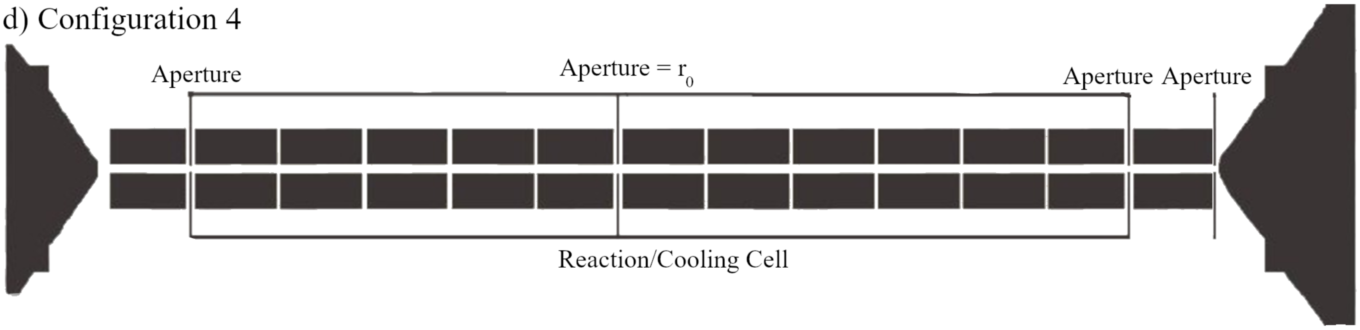

Figure 3.1: Schematics of the ISA configurations studied for best Cl^- transmission. The configurations changed the location and number of apertures within the cell. The number of RFQ segments and acceleration and deceleration optics remained constant. r_0 is defined in Section 2.3.1

The aperture at the entrance of the cooling cell in Configuration 1 of Figure 3.1a) was replaced with a metal plate to measure the current. This showed that 85% of the incoming current was making it past the first three RFQ segments. However, this could not determine if the beam had a low enough energy to be contained by the RFQs or if the beam could be sufficiently captured by the RF field to continue through the first 2.5 mm aperture. A plate was placed at the end of the cooling cell but no cooling gas was added. With only 7% transmission to this plate, the configuration was changed to Configuration 2 for further tests.

3.1.2 Configuration 2

Configuration 2, Figure 3.1b), kept separate reaction and cooling cells but moved the aperture at the entrance of the cooling cell to just one RFQ segment from the deceleration optics. This would allow for the anions to travel a shorter distance through the ISA before colliding with a cooling gas and losing further energy. With a plate at the end of the cooling cell, this improved transmission from 7% to 9% with no cooling gas.

Increasing the diameter of the first aperture to 4 mm provided minimal improvement to the transmission but the addition of He gas to the cooling cell improved transmission to 25%. Further increasing the first aperture to 6 mm diameter increased the transmission to 48% to the plate at the end of the cooling cell. Finally, testing an 8 mm diameter at the first aperture resulted in a decrease to the transmission to 42%. This is likely a result of a lower gas pressure in the cooling cell, resulting in fewer collisions between the anions and the gas.

These promising results led to a transmission test through the ISA. In Configuration 2, a maximum transmission of 2% was found. While this was an improvement over Configuration 1, where no current could be transmitted, additional adjustments to the configuration were made.

3.1.3 Configuration 3

Configuration 3, shown in Figure 3.1c), merged the two cell configurations into a joint cooling and reaction cell. This resulted in a configuration with an entrance aperture at one RFQ

Aperture diameters (mm)	6-13-2.5	6-13-4	8-13-2.5
He pressure (μ bar)	13.5	13.7	10.2
Incoming Current (nA)	281	360	180
Transmission (%)	44	47	49
DC Voltage on Entrance Aperture	74	80	90
DC Voltage on Central Aperture	-6	-5	-2
DC Voltage on Exit Aperture	37	12	39

Table 3.1: Transmission of ^{37}Cl anions for three aperture tests in Configuration 3. The aperture diameters are given as: entrance aperture-central aperture-exit aperture. The incoming current and optimized He gas pressure (calculated based on the method described in Section 3.2.2) are included.

segment from the deceleration optics, a large aperture six RFQ segments from that, and an exit aperture five RFQ segments from the centre aperture and one RFQ segment from the acceleration optics. The central aperture was maintained to divide the load from the two RF amplifiers but would allow the flow of both gases through the entire 'one cell' configuration.

The final aperture diameters chosen were 6 mm at the entrance, 13 mm at the centre, and 4 mm at the exit. The best transmission achieved with this configuration was 47%. Additional aperture test comparisons can be found in Section 3.1.3.1. If not otherwise stated, work in this thesis used Configuration 3 with these aperture sizes. For a more detailed label refer to Figure 2.3.

3.1.3.1 Aperture size determination

Multiple aperture sizes were tested in Configuration 3. The transmission of ^{37}Cl anions for three aperture tests are shown in Table 3.1. The aperture sizes are given in the format entrance aperture diameter-central aperture diameter-exit aperture diameter. These tests used only He gas; the pressures provided are optimized for the maximum current through the ISA and are calculated based on the method described in Section 3.2.2. The incoming current is given as reference. Due to the transmission dependence on current discussed in Section 4.2.6, the test for the 6-13-4 aperture set will have a slightly lower transmission than if an incoming current less than 300 nA was used.

The transmission is further improved from 44% to 47% when increasing the exit aperture diameter from 2.5 mm to 4 mm. The He pressure of the 8-13-2.5 aperture set corresponds to the maximum setting on the mass flow controller that provide gas to the cell. Therefore, this aperture setting may be capable of higher transmission if a higher He gas pressure was possible. Using the mass flow controllers currently on the ISA, the 6-13-4 aperture set was chosen for the work completed in this thesis. With a lower incoming current, it will have a comparable transmission to the 8-13-2.5 set but the higher He pressure may result in lower energy anions that are more likely to react with the reaction gas when it is added to the cell.

3.1.3.2 SIMION 8.1 simulations of deceleration region

The field and particle trajectory simulator, SIMION 8.1 [77], was used in this work to model the deceleration optics and first two RFQ segments of Configuration 3 of the ISA. A 2D image of the 3D SIMION ISA simulation is shown in Figure 3.2. This was created by converting STL files from the SolidWorks software to the Potential Array (PA) files required in SIMION. These simulations used 2 grid units per physical mm. A higher density of grid units would be preferred but this was sufficient for these studies and limited the time per simulation [78].

The programming language LUA was used to control electrode voltages and to import a hard-sphere, elastic ion-neutral gas atom collision model for interactions with up to two gases using a modified Hard Sphere scattering code (HS1) included in SIMION. It did not model reactions between the ion and neutral gas atoms or molecules. The mass of the gas, temperature, pressure, velocity and collisional cross section are adjustable. In these simulations, a gas pressure of 12 μbar was only included after the first aperture. However, the code allows for the user to set a pressure gradient along the entire region being simulated. For He and Cl anion interactions, the cross section was estimated as 3.0 x 10^{-19} m^2 based on the equation:

$$\sigma = \pi(r_{He} + r_{Cl})^2 \tag{3.1}$$

Simulations done in this work used ten thousand mass 36 anions flown from a circular

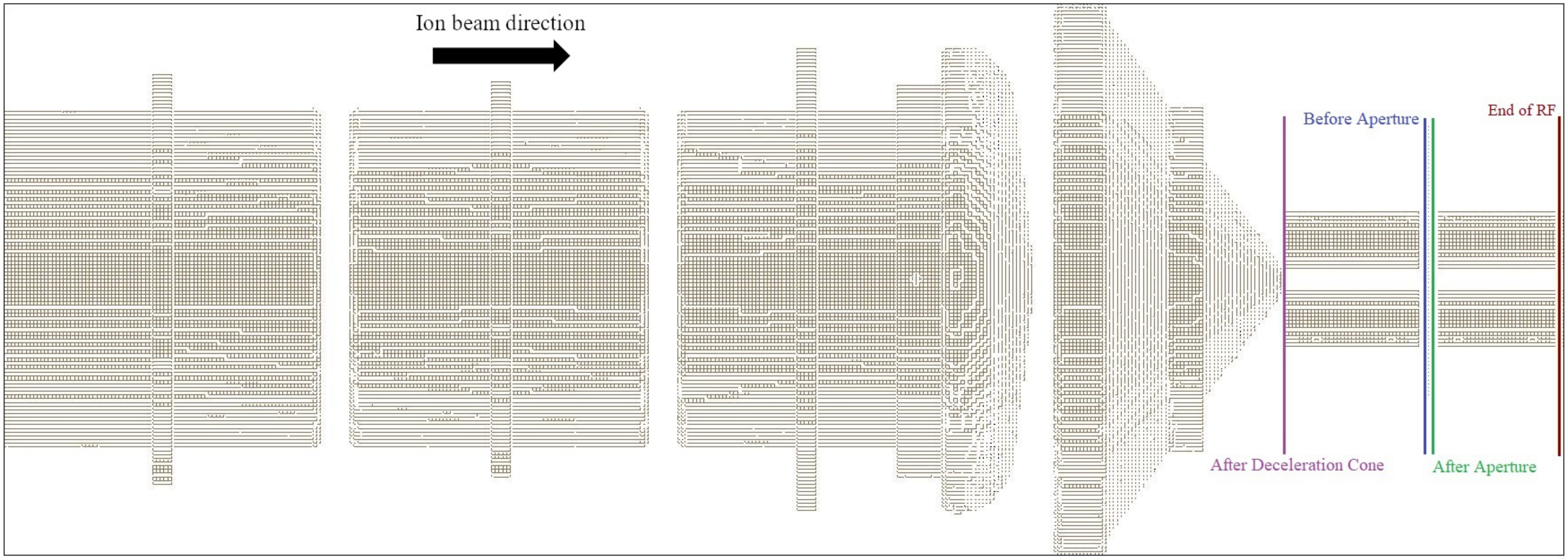

Figure 3.2: SIMION 8.1 simulation of the deceleration optics and two RFQ segments in the ISA. The 3D structure was converted from STL files and uses 2 grid units per mm. The view is of the x- and y-axis but it is symmetrical in the z-axis. The planes that transmission and anion energy were measured in the simulations are indicated with coloured lines.

source with a 2 mm radius. The source was placed at the edge of the simulation (0, 0, 0) with a normal of (1, 0, 0) (flown along the x-axis in Figure 3.3). It was given a filled cone distribution with a half angle of 1.5°. The starting kinetic energy of the beam was -20.00 keV with an energy range up to -20.01 keV.

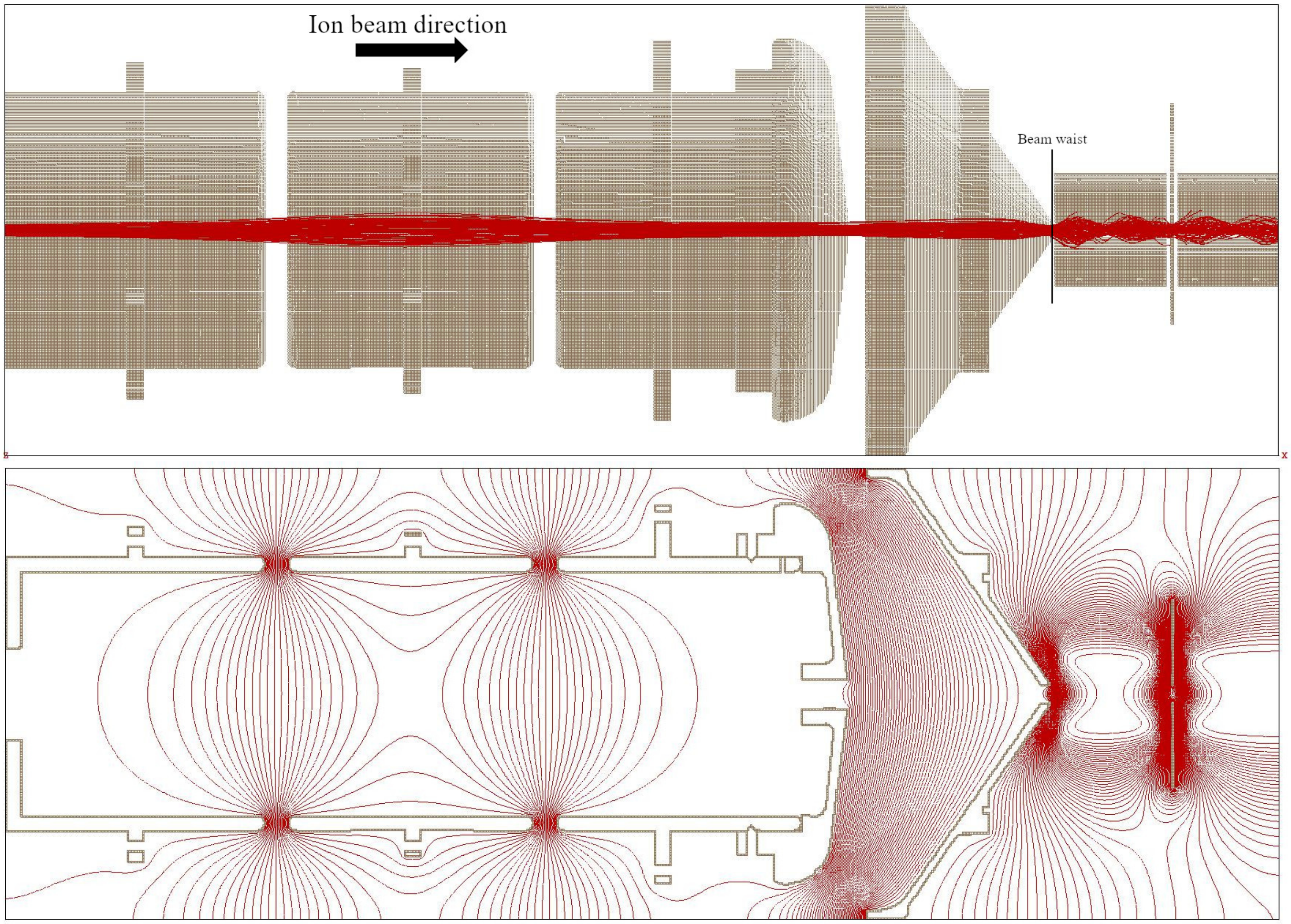

Figure 3.3: SIMION 8.1 3D simulation of the ISA deceleration optics and first two RFQ segments. The upper panel shows the simulated beam envelope traveling in the x-direction. The bottom panel is the field lines for the ISA settings used in this simulation.

Figure 3.3 shows the beam envelope and the potential field lines for the electrode settings listed in Table 3.2. This shows that the beam waist is located just inside the first RFQ segment, as predicted as the optimal location in Kieser et al. [34]. This allows the RF field to capture the diverging beam. Table 3.2 compares the settings used to generate these results to the average settings optimized for experimental transmission. The average experimental

Element	Simulation Setting	Average Experimental Setting
Beam Energy (eV)	-20,000	-20,113
ISA Deck Voltage (V)	-19,950	-20,083
Einzel Lens Electrode 1 (V)	0	0
Einzel Lens Electrode 2 (V)	-18,000	-16,500
Einzel Lens Electrode 3 (V)	300	0
Deceleration Cone (V)*	0	326
Frequency (MHz)	2.5	2.5
RF Amplitude (V_{pp})*	1100	1150
RFQ Rod 1 Offset (V)*	15	43
Aperture (V)*	20	62
RFQ Rod 2 Offset(V)*	25	-16

Table 3.2: The settings of the electrodes used in SIMION 8.1 simulations of the ISA's deceleration optics and first two RFQ segments. *Voltages are relative to the deck voltages; others are with respect to the lab ground.

settings were obtained after simulation work and therefore there are some differences in the values.

SIMION exports an axial velocity, v_x, and the components of transverse velocity, v_y and v_z. Using v_x a kinetic energy can be determined. This will be referred to as the 'axial' kinetic energy. The y- and z- component velocity can be used to find the total transverse component velocity that can then be used to find a kinetic energy. This will be referred to as the 'transverse' kinetic energy. Figure 3.4 shows the simulated distribution of ion energies associated with the transverse and axial components of the ion motion that reach the end of the second RFQ segment. This location is indicated by a red line in Figure 3.2. The starting energy of the ions was -20 keV. Row a) of Figure 3.4 shows the energy distribution with no cooling gas in the reaction cell. Row b) shows the energy distribution with 12 μbar of He.

Without a gas in the cooling cell the average 'transverse' component kinetic energy was 19 eV and the maximum was 207 eV. When 12 μbar of He is added to the reaction cell of the ISA in the simulations, the average 'transverse' component kinetic energy is slightly reduced to 17 eV and the maximum is increased to 230 eV. The difference in the 'transverse' kinetic energy between the two simulations is minimal, as expected. The average 'axial' energy of the ions with no cooling gas is 119 eV and the maximum is 230 eV. When 12 μbar of He

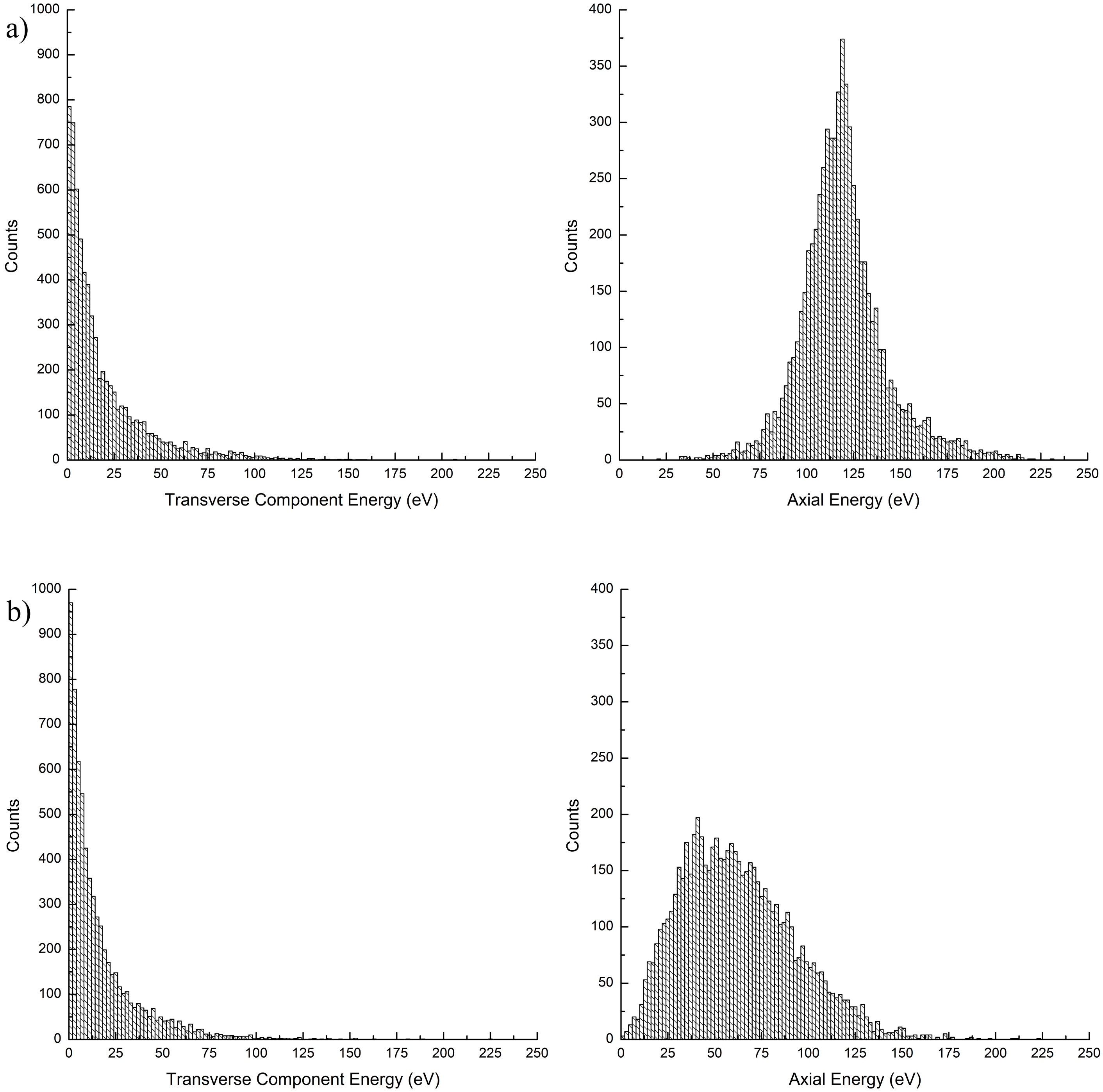

Figure 3.4: SIMION 8.1 simulation of the 'transverse' component and 'axial' energy (eV) distribution for ions with a -20 keV starting energy. The energy was measured at the end of the second RFQ segment (red line indicated in Figure 3.2). Row a) shows the energy distribution with no cooling gas in the reaction cell. Row b) shows the energy distribution with 12 μbar of He.

is added, the average ‘axial’ energy is reduced to 62 eV and the maximum is decreased to 222 eV. The large decrease in the average ‘axial’ energy is expected, as collisions with gas should directly impact this energy. An ion energy of 62 eV would result in a center of mass energy of:

$$E_{cm} = \frac{E_{lab} m_n}{(m_n + m_i)} = \frac{62eV * 4amu}{(4amu + 36amu)} = 6.2eV \tag{3.2}$$

An E_{cm} of 6.2 eV is higher than the electron affinity of Cl (3.61 eV). Therefore, a reduction in incoming ion energy would be beneficial to chlorine transmission through the ISA.

Simulations were also run to determine if the starting parameters of the ions affected which ions travelled to the end of the second RFQ segment. The starting location and energy of the ions with no transverse component motion did not have a noticeable effect. However, a smaller starting angle (lower energy of the ‘transverse’ component) increased the probability that the ion would reach the end of RFQ segment 2. Figure 3.5a) shows the starting ‘transverse’ energy for all ions flown through the SIMION 8.1 simulation. These energies ranged from 0-14 eV. Figure 3.5b) shows the same energy for those ions that were transmitted to the end of the second RFQ segment. The energy range of 0-14 eV remains the same. However, it is clear that the majority of the low energy ions are transmitted, while only approximately 50% of the ions with starting ‘transverse’ component energies from 10-14 eV were transmitted to this point. The average starting ‘transverse’ energy of all of the ions was 7 eV. The average starting ‘transverse’ energy of the ions that were transmitted to the end of the second RFQ segment was decreased to 6 eV. It is beneficial to keep the ‘transverse’ energy of incoming ions relatively low. However, the incoming ‘transverse’ energy can only be modified by altering the angles of the deceleration cone. This value is fixed and would require further simulation to determine if it would be beneficial to alter this parameter in future versions of the ISA.

Table 3.3 shows transmission and ion energy at four points along the deceleration pathway, indicated in Figure 3.2. The settings used were those in Table 3.2. The transmission results show that all of the initial ions will make it through the deceleration cone. This agrees with experimental measurements discussed in Section 3.1.1. Approximately 13% of

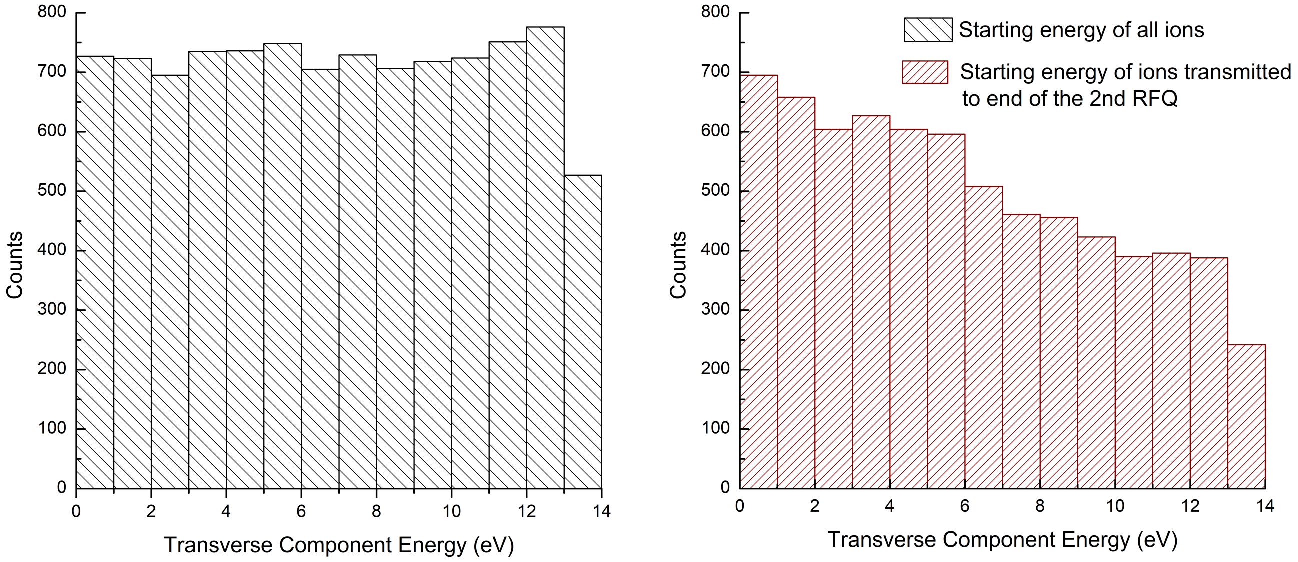

Figure 3.5: SIMIONS 8.1 simulation of starting 'transverse' component energy for ions transmitted to the end of the second RFQ segment. Plot a) shows the energy of the 'transverse' component for all ions flown through the simulation. Plot b) shows the same energy for those ions that were transmitted to the end of the second RFQ segment.

the ions are lost to the first RFQ segment to just before the first aperture. This is likely due to the deceleration cone voltage attracting ions away from the first segment or with higher energy ions not being confined by the RF. The transmission further decreases to 74% making it through the first aperture. If ions are not properly controlled by the RF at this point, they may not be guided through the 6 mm aperture, leading to transmission losses. Finally, the transmission is further decreased to 66% at the end of the final RFQ. These transmission values align with experimental transmissions through the deceleration cone and to the first aperture.

At all four measurement locations in Figure 3.2, the average 'transverse' energy of the ions remains in the 10-17 eV range but may slightly increase due to the RF field [79]. The 'axial' energy begins at an average of 86 eV after the deceleration cone. This energy is increased to approximately 115 eV after the first RFQ segment. The increase in energy is from the DC voltage on the RFQ segment and first aperture plate. The collisions with He gas reduces the 'axial' energy signficiantly, to 62 eV at the end of the second RFQ segment.

Location	Transmission (%)	Transverse E_{avg} (eV)	Axial E_{avg} (eV)
After Decel Cone (6 mm)	100	12	86
Before 1st Aperture (6 mm)	86.8	15	116
After 1st Aperture (6 mm)	74.1	11	114
End of 2nd RFQ	66.1	17	62

Table 3.3: SIMION 8.1 simulation of the average 'transverse' component and 'axial' energy (eV) for ions with the electrodes set at those listed in Table 3.2. The size of the deceleration cone aperture and first aperture plate are listed in brackets. The four locations are indicated in Figure 3.2.

Simulations of Configuration 1 were tested and showed that by the second RFQ segment, the ions had gained too much energy to be properly captured by the RF field. By the third RFQ segment, and thus the first aperture, most were too energetic to be transmitted through the aperture and into the cooling cell. This may explain why no outgoing current was measured in this configuration. Future work will compare the SIMION 8.1 simulated ion energies and transmission of the same region in Configuration 4, discussed in Section 3.1.4, to improve understanding of the experimental increase in transmission.

3.1.3.3 Simulations using experimentally determined settings

Experimental measurements with the ISA were performed after the simulation tests described above. The optimized electrode settings were determined experimentally and are listed in Table 3.2. These electrode settings were used in the SIMION 8.1 simulation of the ISA deceleration region to compare the results to those found with the previous electrode settings. Additionally, the starting energy of the beam was changed to a uniform distribution from -20.123 keV to -20.083 keV. A plot of the beam trajectory is shown in Figure 3.6. It is comparable to the trajectory shown in the upper panel of Figure 3.3. However, the increase in deceleration cone voltage attracts some ions away from the entrance of the RFQs and back towards the cone. The beam waist is slightly further into the first RFQ.

The transmission and average energy at each point along Figure 3.2 for these experimental settings are listed in Table 3.4. The transmission from the cone is now 4.3% lower than the original simulation settings. This agrees with experimental transmission measurements

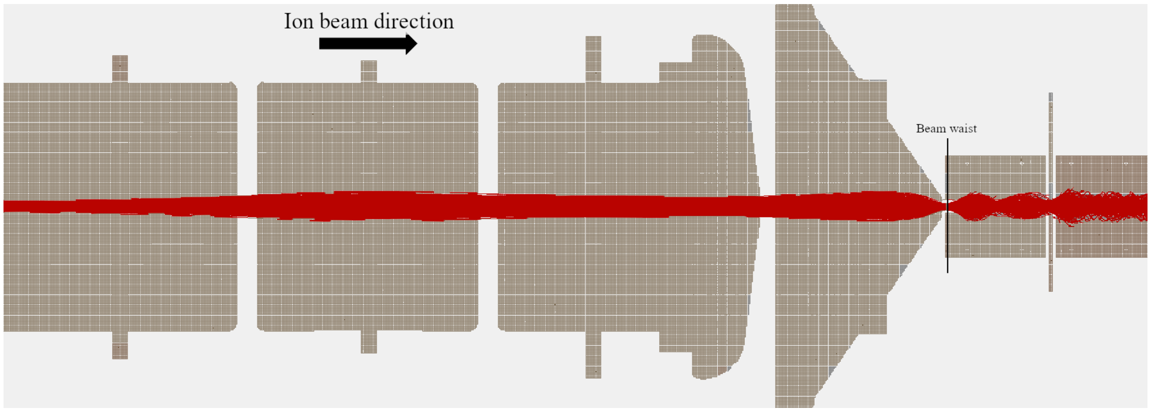

Figure 3.6: SIMION 8.1 3D simulation of the ISA deceleration optics and first two RFQ segments using the experimentally optimized ISA settings from Table 3.2. The simulated beam envelope is traveling in the x direction.

of 90% or greater through the deceleration cone, discussed in Section 3.1.1. Before and after the first aperture the transmission values are comparable between the two electrode settings. The agreement in transmission at these locations, despite the lower transmission to the exit of the deceleration cone, indicates that the transmission from the deceleration cone to before the first aperture is improved with the experimental settings. At the end of the RFQ the transmission is 11% lower for the experimental settings.

Location	Transmission (%)	Transverse E_{avg} (eV)	Axial E_{avg} (eV)
After Decel Cone (6 mm)	95.7	18	291
Before 1st Aperture (6 mm)	86.6	17	108
After 1st Aperture (6 mm)	74.2	15	97
End of 2nd RFQ	55.0	24	27

Table 3.4: SIMION 8.1 simulation of the average ‘transverse’ component and ‘axial’ energy (eV) for ions with the electrodes set at those listed under experimental settings in Table 3.2. The size of the deceleration cone aperture and first aperture plate are listed in brackets.

Due to the increase in starting kinetic energy of the beam, all locations have a slightly larger ‘transverse’ component energy than the initial simulation results. The axial energy exiting the cone is significantly larger due to the increased voltage on the deceleration cone. However, after travelling through the first RFQ the axial energy is reduced to less than the values found with the original simulation settings.

3.1.3.4 Deceleration cone voltage range

The deceleration cone was programmed to have a voltage adjustment from -6000 to 6000 V. During transmission tests, it was often optimized to approximately 600 V. Because this voltage range is large, it may be hard to achieve stable voltages at low settings. The voltage placed on the deceleration cone will increase or decrease the energy of the anions. Depending on the energy of the anions and the setting of the deceleration cone, it may also attract anions towards the exit side of the cone and away from the first RFQ segment. Therefore, it is important to have fine control in the low voltage region.

To test if a setting of 0 V was beneficial to transmission, the cone was externally grounded and the ISA settings were optimized for best transmission. With the cone grounded, the transmission dropped from 47% to 28%. A voltage divider was then added to the deceleration cone. This changed the range to -400 to 400 V but allowed for finer control of the voltages in this range. This improved the transmission very slightly (approximately 1-2%). The new setting for the cone is used in the majority of the work in this thesis. The optimized cone values typically fall with the 300-400 V range.

3.1.4 Configuration 4

While other tests (Chapters 4 and 5) of the ISA continued with Configuration 3, transmission above 50% is still desirable and configuration changes to achieve this were further investigated. Configuration 4, Figure 3.1d), has an additional aperture placed before the first RFQ segment, immediately following the deceleration cone. This RFQ segment is still open to the ISA vacuum chamber and so should not contain high gas pressures even when the reaction and cooling cell is at higher pressures. The aperture was placed here to counteract the attractive potential field exerted on the anions by the deceleration cone after they have exited it and block the ions from seeing the RF field prior to being captured by it. Placing a DC voltage of 240 V on the new aperture (with a maximum of 250 V in this system), a transmission of 81% of the beam was observed through the ISA when filled with He gas.

The approximately 35% increase in transmission between Configuration 3 and Configuration 4 is promising for increasing count rate in Cl runs. While the studies in Chapter 4 and Chapter 5 were completed prior to this transmission improvement, plans are in place to repeat these studies with Configuration 4.

3.2 Transmission based on cooling and reaction gas pressures

The gas cell of the ISA is filled with two gases: an inert cooling gas and a reaction gas. Prior to injection into the cell, the beam is first decelerated using the deceleration cone of the ISA. This reduces electron detachment losses from initial collisions between the anions and the gases [30]. The cooling gas is used to further lower the ion energy through collisional cooling. This should improve the transmission of the Cl^- beam because a lower energy beam will be better confined by the potential well of the RFQs. The reaction gas is used to preferentially react with the interfering isobar. It is chosen on the basis that its reaction rate with the interfering isobar is maximized and that rate with the isotope of interest is minimized.

3.2.1 Transmission in vacuum

The transmission of the anions through the ISA with no gas in the cell was tested. Figure 3.7 shows the transmission at 0 μbar of incoming gas; this corresponds to a vacuum in the reaction and cooling cell in the range of 10^{-6} μbar. The transmission values are a ratio of the incoming and outgoing current measured in on-axis Faraday cups at the entrance and exit of the ISA, respectively. The best transmission achieved was 5% of the incoming beam. With no cooling gas to decrease the anion energy, the low transmission is likely due to the anions being too energetic (hundreds of eVs) to be contained by the RFQs.

3.2.2 Gas pressure determination from flow rate

As described in Section 2.3.1.1, the user sets the flow of both a cooling and a reaction gas using two mass flow controllers. The user sets the flow rate in units of SCCM and the ISA cell does not contain a vacuum gauge. Therefore, the pressure of the two gases in the cell cannot be directly measured and needs to be mathematically determined. All cooling and reaction gas pressures presented in this work are approximate pressures calculated by a formula provided by *Isobarex*. It is based on the user-set flow rate and includes correction

Element/Molecule	Mass (AMU) [42]	Electron Affinity (eV) [80]	Ionization Energy (eV) [42]
He	4.00	-21.80	24.59
CH_4	16.04	-0.25	12.61
Ne	20.18	-4.39	21.56
N_2	28.01	-2.006	15.58
S	32.06	2.08	10.36
Cl	35.45	3.61	12.97
F_2	38.00	3.00	15.70
Ar	39.95	-2.08	15.75
NO_2	46.01	2.27	9.59
BF_3	67.81	2.65	15.70

Table 3.5: The mass, electron affinity, and ionization energy of the various atoms and molecules studied as anions or gases in the ISA.

factors from the mass flow controller supplier, based on the gas type being used. It is dependent on the aperture sizes of the ISA configuration being used, the pumping speeds of the turbo pumps, and a conductance correction factor.

3.2.3 Cooling gas selection

The cooling gas selection was completed by measuring the transmission of Cl anions through the ISA with the reaction cell filled with a range of pressures of each gas studied. The cooling gas should be non-reactive with Cl and therefore is selected based on the best transmission achievable. The gases He, Ne, and Ar were tested as possible cooling gases for the measurement of Cl. The mass, electron affinity, and ionization energy of these elements can be found in Table 3.5.

Figure 3.7 shows the transmission of a 190 nA ^{37}Cl anion beam through the ISA filled with He, Ne, or Ar at a range of pressures. The points on the plot connected by a line used ISA component settings tuned for optimal transmission at 13.7 μbar (9.99 SCCM) of He. The same voltage settings were used to scan the pressures for transmission of Cl anions through only He, NO_2, Ne, Ar, or a mixture of 11 μbar He and NO_2. The individual triangle point and individual square point correspond to the best transmission achievable with Ne (7.2 μbar or 2 SCCM) and Ar (3.6 μbar or 1 SCCM), respectively. In these two cases, the ISA components were tuned for these gas pressures. The maximum transmission achieved with Ne was 22% and 5% with Ar.

Early tests also measured Cl transmission using N_2, CH_4, and a mixture of Ne and He. Mixing any Ne into a He-filled cell reduced the transmission to values comparable to a cell with only Ne gas. The transmission through N_2 and CH_4 was comparable to NO_2 with best transmission at 11% and 8%, respectively.

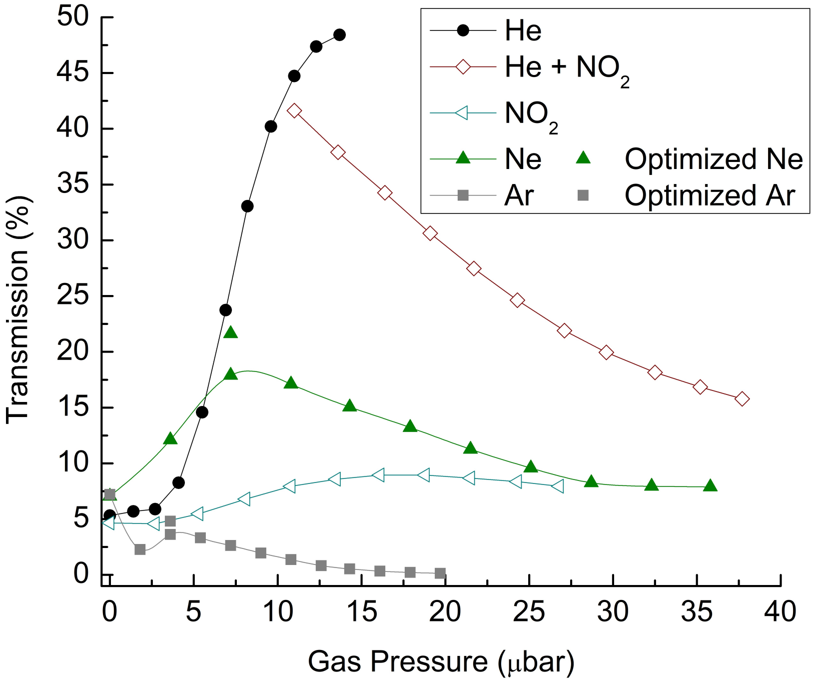

Figure 3.7: Transmission of ^{37}Cl through the ISA using various cooling and reaction gases at a range of pressures. Connected points used voltage settings optimized for 13.7 μbar He. The He + NO_2 points are a measure of the total pressure of the two gases with a constant 11 μbar He. The individual points use voltage settings optimized for the respective gas being tested. The extent of the He curve is limited by the maximum flow rate of one mass flow controller. [81]

The best transmission with Configuration 3, detailed in Section 3.1, was 50% of the incoming beam at 13.7 μbar (9.99 SCCM) of He. This pressure corresponds to the maximum flow rate allowed by one mass flow controller. A test was completed with He flowing through both mass flow controllers to provide a higher pressure of He within the ISA but a plateau was observed and additional He did not improve the transmission.

All of the possible cooling gases chosen have low electron affinities, listed in Table 3.5, but low transmission was still observed due to the mass ratio between the gas and Cl. Ar was the only gas tested with a larger mass than Cl. The transmission achieved with Ar is lower than the transmission with no cooling gas.

Although small angle elastic collisions between heavier gas atoms and Cl^- would result in greater energy loss and more controllable ions, initial large angle collisions would result in significant scattering losses and electron detachment. To achieve the same beam cooling with the lighter gas, He, higher pressures than the heavier gases are required. This is shown in Figure 3.7, with the best transmission of He occuring at higher pressures than with the heavier gases.

3.2.4 Reaction gas selection

The ISA is filled with a reaction gas that exploits the difference in reaction rate between an isotope and its isobar. For Cl^-, this gas is chosen such that an anion-neutral gas atom reaction will be energetically favourable for the interfering isobar but not for the isotope of interest. In the case of ^{36}Cl, the difference in electron affinity between Cl and S, shown in Table 3.5, means a gas with an electron affinity between these two could produce a charge transfer reaction with S^- that would be exothermic but would be endothermic with Cl^-.

Previous work by Dunkin et al. [32] found the following pressure-dependent reaction rates, k, for the charge change reactions:

$$Cl^- + NO_2 \rightarrow Cl + NO_2^- \qquad k =< 6\text{x}10^{-12} cm^3/s \tag{3.3}$$

$$S^- + NO_2 \rightarrow S + NO_2^- \qquad k = 1.3\text{x}10^{-9} cm^3/s \tag{3.4}$$

With an electron affinity of 2.27 eV (Table 3.5), NO_2 gas will have an exothermic reaction with S^- and an endothermic reaction with Cl^- and was a good candidate for a reaction gas. Using a pre-commercial ISA, NO_2 was tested by Litherland et al. [35] and Eliades et al. [36] with over six orders of magnitude suppression in S^- compared to Cl^-. Suppression in O_2 was also tested but only a weak attenuation was observed. Suppression of S^- in this work is discussed in Section 3.5.

The transmission of Cl^- in a range of NO_2 pressures or a mixture of 11 μbar He and a range of NO_2 pressures are also included in Figure 3.7. Poor transmission is seen with all pressures of NO_2 when tested without the addition of He as a cooling gas. While the addition of NO_2 reduces the transmission from pure He gas, the reaction gas only reduces the Cl^- transmission to 20%, higher than any of the heavier cooling gases tested.

3.2.5 Transmission in Configuration 4

Figure 3.8 shows the transmission of $^{37}Cl^-$ through Configuration 4 of the ISA with 11 μbar of He and an increasing NO_2 pressure. This is compared to the transmission found in Configuration 3 with the same He pressure and increasing NO_2. Not only is the overall transmission improved by over 25%, the addition of NO_2 does not decrease the transmission at the same rate. At approximately 24 μbar of He and NO_2 in the ISA cell, corresponding to usual running conditions, the transmission differs by over 30%.

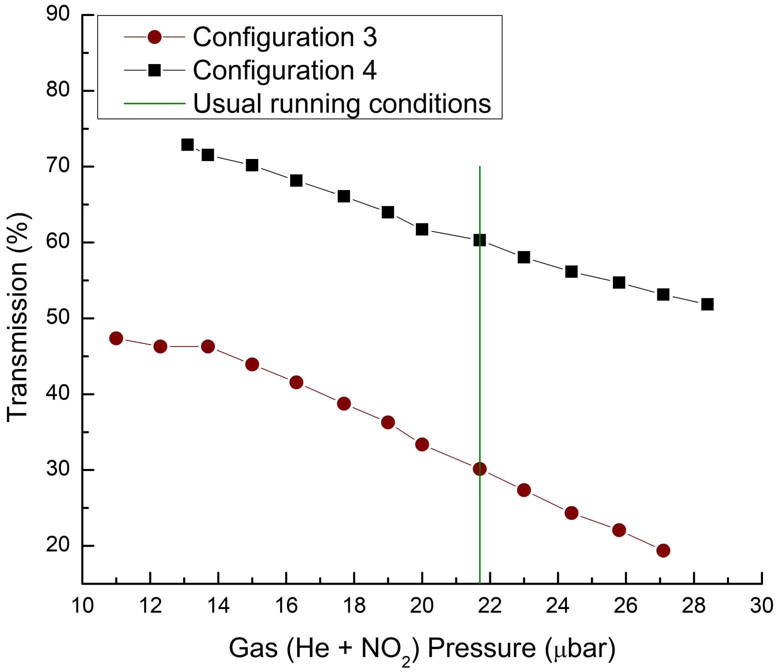

Figure 3.8: Transmission of ^{37}Cl with 11 μbar of He and a varying NO_2 pressure through the ISA in two configurations. The red circles are data from Configuration 3, used for the majority of the measurements in this work. The black squares are from Configuration 4. The green line indicates typical running pressures.

3.2.6 Equilibrium between NO_2 and N_2O_4

NO_2 undergoes a reversible reaction with itself to form N_2O_4. At room temperature and atmospheric pressure, there will be more N_2O_4 than NO_2. In a gas cylinder, the N_2O_4 will condense as a liquid [82]. It is important that the majority of gas flowing through the mass flow controllers and in the reaction cell is NO_2. This can be calculated for room temperature at a range of pressures to determine the ratio of NO_2 to N_2O_4. The pressure within the cell is measured in the 0-40 μbar range, much smaller than the 1 atm (1.01 x 10^6 μbar) where N_2O_4 is dominant. This ratio can be determined using the partial pressures and equilibrium constant, K_p [83].

$$K_p = \frac{(P_{NO_2})^2}{(P_{N_2O_4})} = \frac{(P_{NO_2}/P_0)^2}{P_0 - (P_{NO_2}/P_0)} \tag{3.5}$$

where P_0 is 1 atm. Using the room temperature K_p of Roscoe and Hind [82] of 0.137, P_{NO_2} in Equation 3.5 can be solved using the quadratic equation. At 1 μbar in the ISA reaction cell, more than 99.99% of the nitrogen oxides are in the NO_2 form. At the maximum cell pressure of 40 μbar, the nitrogen oxides are still 99.97% NO_2.

3.3 Transmission dependence on ISA deck voltage

To facilitate the deceleration of the anion beam, the entire ISA vacuum chamber, referred to as the ‘deck’, is kept at a voltage close to the energy of the beam. In this work, the source voltage, and thus the ion beam energy, is set to a nominal -20 keV. To determine the actual voltage, a Fluke-189 True RMS Multimeter was connected to the external portion of the source head using a Fluke 80K-40 High Voltage Probe, with the voltage set to -20 kV. An actual voltage of -20,113 V ± 10 V was measured.

Because the ISA deck voltage will be scanned during tuning, a calibration curve between the voltage set on the control computer and the actual voltage measured by the Fluke multimeter and high voltage probe was used to measure the deck to lab ground voltage. The ISA deck voltage was scanned and the outgoing current was measured in the Faraday cup at the exit of the ISA (ISA exit on-axis).

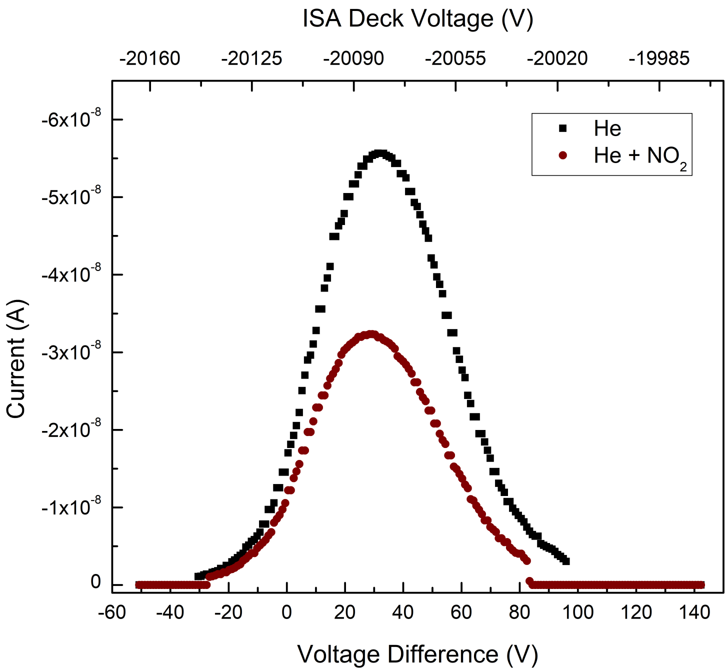

Figure 3.9: The outgoing current of ^{37}Cl as the deck voltage of the ISA is changed. The upper x-axis provides the voltage setting of the ISA. The lower scale is the difference between the ISA deck setting and the energy of the beam. Tests were completed in 13.7 μbar He and a mixture of 11 μbar He and 10.8 μbar NO$_2$.

Figure 3.9 shows the measured currents in Amperes with the calibrated ISA deck voltage on the top x-axis. The bottom x-axis is the voltage difference between the source voltage and the voltage of the ISA given by:

$$\Delta V = V_{ISA} - V_{source} \tag{3.6}$$

Figure 3.9 shows that non-zero transmission only occurs over a range of 110 V, with the highest transmission at a voltage difference of 27-33 V. However, this measurement range has a large error of 14 V. A voltage-divider system has been designed to measure the voltage difference between the two systems more accurately and during use of the ISA.

Previous work on an RFQ ion beam cooler by Liu et al. [30] found the best transmission of anions at -20 keV was at a deck voltage difference of 40 V. Using an ISA prototype, Eliades et al. [84] found the best transmission at a deck voltage difference of approximately 60 V.

3.4 Transmission dependence on the Mathieu q_2 parameter

The dimensionless RFQ stability parameter, q_2, was discussed in Section 2.3.1 and defined by the equation:

$$q_2 = \frac{qV_{pp}}{2m(\pi f r_0)^2} \tag{3.7}$$

The region of stability for ion trajectories through an RFQ ion guide is $q_2 < 0.908$ [85]. Low transmission is seen at $q_2 < 0.2$. The best transmission in the ISA is typically found around $q_2 = 0.55$-0.8.

The ISA has a fixed inscribed radius and the frequency is fixed to 2.5 MHz. Tests were completed using a ^{37}Cl beam. With all other values fixed, the q_2 is proportional to the V_{pp} set by the user. Figure 3.10 shows the current measured in the ISA exit on-axis Faraday cup with a fixed incoming current. The V_{pp} on the bottom x-axis was scanned, and the q_2 parameter on the top x-axis was calculated from the varied V_{pp}. While typical ISA measurement tune the V_{pp} of the first 7 segments and last 6 segments separately for best transmission, this test applied the same V_{pp} to both sets of RFQ segments.

Two methods were used to measure the dependence of the outgoing current on q_2 of the ISA. The red circles in Figure 3.10 optimized all components of the ISA for best transmission. The DC offset voltages on the RFQ segments and apertures were adjusted for each V_{pp} value. The black squares in Figure 3.10 used the same ISA settings for each value of V_{pp}. In this case, all voltages were optimized for the best transmission, including V_{pp}. V_{pp} was then scanned with all other settings remaining constant. The two peaks in the black square curve indicate that these voltage settings worked well at multiple q_2 values.

The use of cooling and reaction gases may keep the energy of the ions sufficiently low despite them gaining energy from the field at higher V_{pp}. Our measurements show that transmission remains relatively high until $q_2 = 1.2$, after which it begins to rapidly decrease. The incoming beam may have a large energy spread that cannot be sufficiently trapped by low V_{pp}, resulting in better transmission at higher q_2.

The apertures in place to contain the gas inside of the ISA reaction cell may also decrease

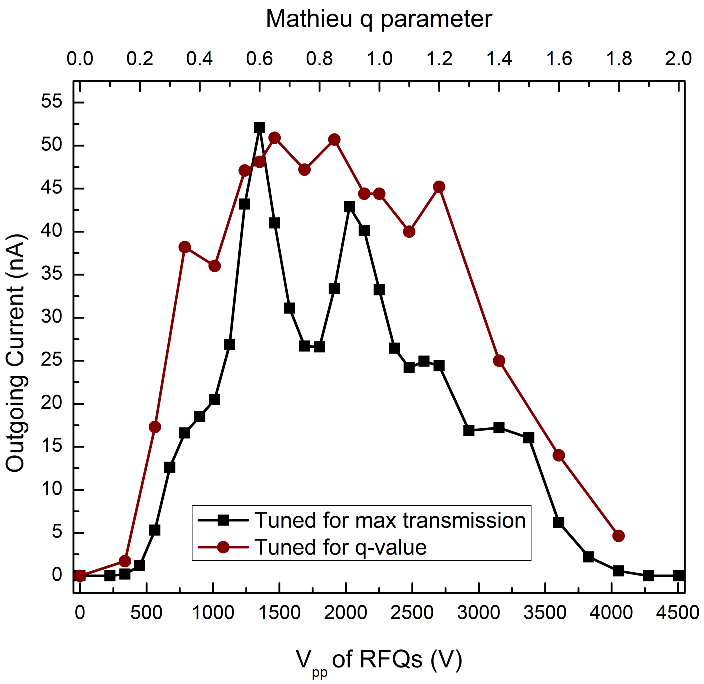

Figure 3.10: The outgoing current of ^{37}Cl from the ISA as a function of the RFQ V_{pp} and the q_2 parameter calculated from it. The black squares were using ISA settings optimized for the maximum transmission. The red points used ISA settings retuned for maximum transmission at each V_{pp}.

transmission depending on the q_2 parameter. If the amplitude of the ion trajectory is larger than the aperture at the exit of the ISA reaction cell, then transmission could be decreased. However, the tests discussed in Section 3.1.3.1 show that increased aperture diameter at the end of the ISA do not have large effects on the transmission. This indicates that the ions are at a sufficiently low energy that they can be focused through the aperture with a small DC voltage applied. The amplitude of ion trajectory at this point should not have large effects on the transmission.

3.5 Cl^- and S^- attenuation in NO_2 in Configuration 3

It is important that the reaction gas, NO_2, attenuates the S^- while allowing the Cl^- to pass through the reaction cell. In Configuration 3, the count rate of $^{34,36}S^-$ and the current of $^{35,37}Cl^-$ were measured as the NO_2 pressure in the reaction cell was increased. Figure 3.11 shows the results using an AgCl and Nb target. For these tests, the ISA settings were tuned for the highest transmission of a stable Cl beam, which uses approximately 15 μbar of He. However, during the measurements in Figure 3.11 approximately 11 μbar of He was used. Higher He pressures resulted in lower transmission when NO_2 is also present. The data taken in each measurement are normalized to the highest current or count rate measured in the Faraday cup or GIC of the measurement date.

The data recorded in August 2020 and July 2021 used $^{36}S^-$, while the October 2021 data used $^{34}S^-$ as a proxy for $^{36}S^-$. The higher abundance (4.25%) of $^{34}S^-$ provides a starting current two orders of magnitude greater than $^{36}S^-$ without using a target with a high S concentration that could lead to contamination in the source or ISA and affect future data collection. $^{34}S^-$ also does not have any interfering isobars that would affect the measurement. Both $^{36}S^-$ and $^{34}S^-$ counts were measured in the GIC. However, with no NO_2 in the reaction cell the $^{34}S^-$ had currents of 2-500 fA, too high for the GIC. These were measured in the Faraday cup before the GIC.

The Cl measurements used $^{35,37}Cl^-$ as a proxy for total Cl, including $^{36}Cl^-$, and were measured in the GIC on-axis Faraday cup. The $^{37}Cl^-$ had input currents ranging from 50 to 300 nA. $^{35}Cl^-$ was measured in July 2021 and had an input current of approximately 700 nA. No difference in the suppression of $^{35}Cl^-$ and $^{37}Cl^-$ was found. Variations in the source were monitored using the incoming stable chlorine current. This current was measured at the beginning and end of the tests; the variations were <2 nA, so no corrections were applied.

More than seven orders of magnitude reduction in the S^- to Cl^- was achieved with approximately 13 μbar of NO_2, shown in Figure 3.11. The Cl^- was only reduced to 25-40% of the original outgoing current. In Figure 3.11, the weighted average of multiple days of data collection is shown in the fit line.

The loss of Cl^- may be due to electron detachment and scattering at the relatively high energies that the anions enter the ISA cell. The initial collisions between Cl^- and NO_2 may also have a high enough centre of mass energy to overcome the energy difference in electron affinity, causing a charge change reaction.

Each test showed an increase in S counts at 14.7 μbar of NO_2. The previous measurements by Eliades et al. [38] on a pre-commercial ISA noticed a plateau in S suppression.

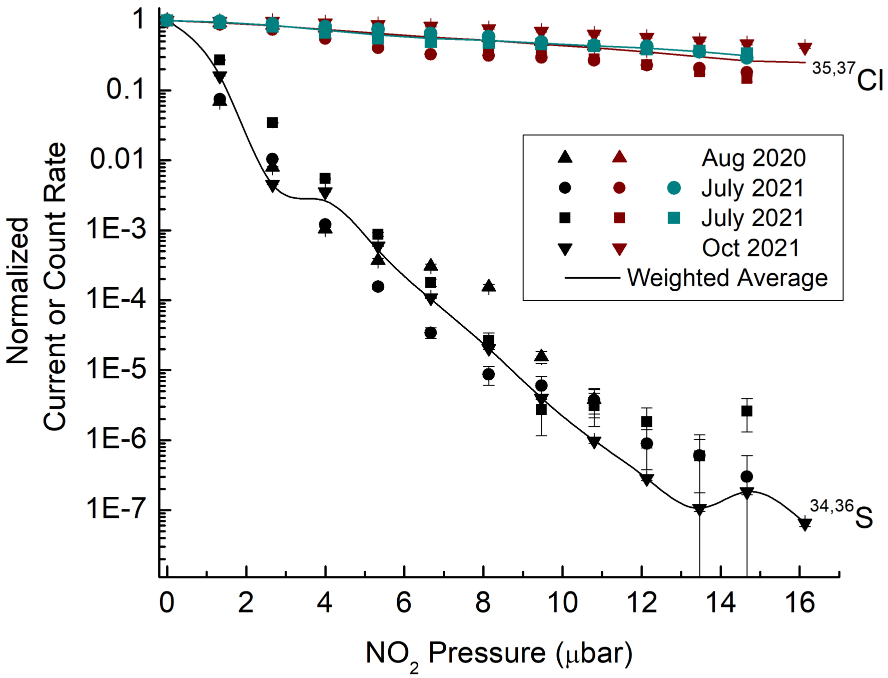

Figure 3.11: The suppression of S and Cl based on the pressure of NO_2 within the ISA reaction cell. ^{34}S was used for the Oct 2021 points and ^{36}S was used Aug 2020 and July 2021 points. ^{37}Cl was measured Aug 2020, July 2021 and Oct 2021. ^{35}Cl was measured in July 2021. The currents and count rates were normalized to the maximum current on their respective measurement date. [81]

This bump and plateau in the data in Figure 3.11 may be due to a reverse reaction with the neutral S that remains in the cell after the charge change reaction with NO_2 or to the creation of molecular anions that will dissociate in the accelerator terminal and add to the mass 36 beam. Eliades et al. [86] found that the S^- that neutralized and then gained an electron within the ISA cell accounted for 10-30% of the increased S counts. Future work may study the reaction products leaving the ISA using a detector system placed after the 45° magnet discussed in Section 2.3. This may help to clarify the process behind the plateau and bump seen in the S suppression curve in Figure 3.11.

3.6 Conclusion

The *Isbarex Corp.* ISA has been integrated into the AEL-AMS 3 MV system and characterized for best transmission of Cl anions and suppression of S anions. The configuration of gas cells and apertures have been studied and found that a transmissions of 80% for $^{37}Cl^{-}$ in He and 62 % in normal pressures of He and NO_2 are possible using Configuration 4. This is comparable to the ILIAMS at VERA. Lachner et al. [63] and Martschini et al. [17] found an average Cl transmission of 64% and a maximum transmission of 80%. The pre-commercial ISA studied by Eliades showed tranmission comparable to Configuration 3 [84].

He has been selected as the cooling gas and NO_2 the reaction gas for Cl studies. The use of NO_2 as the reaction gas showed more than 7 orders of magnitude reduction in S. In comparison, the ILIAMS has achieved 10 orders of magnitude suppression of S using a 532 nm laser with 10 W of power [63, 17]. The pre-commercial ISA achieved 5-6 orders of magnitude S suppression [84]. Work is continuing to enhance the suppression further. The addition of a detector system after the 45° magnet following the ISA may help to characterize the interference produced in the ISA reaction cell. Table 3.5 indicates that the gases F_2 and BF_3 have electron affinities that will produce exothermic reactions with S anions but endothermic reactions with Cl anions. The decrease in mass from NO_2 to F_2 may result in fewer collisional losses. However, all reaction gases listed are toxic and may not be possible to use in routine tests.

Chapter 4

ISA-AMS measurements of ^{36}Cl/Cl reference standards

With Configuration 3 (Section 3.1) tested for the best transmission of ^{36}Cl and the attenuation of ^{36}S in NO_2, the ^{36}Cl analytical capabilities of the ISA were tested using standards of known ^{36}Cl/Cl ratios. In the following chapter, the measurement technique and accelerator settings used to measure ^{36}Cl/Cl standards are detailed. The ISA-AMS measured ^{36}Cl/Cl ratios can then be compared to the nominal values of a standard set and a dilution series. Using these measurements, the stability of the system and the ^{36}Cl blank level of ISA-AMS can be determined.

4.1 Chlorine standards

One set of reference standards and one dilution series were used to test the ^{36}Cl analytical capabilites of the ISA. The ^{36}Cl reference standards were previously used in the thesis work of Eliades [84] and were provided by Dr. Mark Caffee of Purdue Rare Isotope Measurement (PRIME) Lab, Department of Physics, Purdue University. The four standards, listed in Table 4.1, were in solid AgCl form. They had not been stored in a dry, dark environment, causing them to undergo photodecomposition. This produces Ag metal and Cl_2 gas, changing the colour of the standards to a purple/grey. The standards were dried prior to mixing with Nb but were still sticky and difficult to break into powdered form. This produced less homogenous AgCl:Nb mixtures and reduced the Cl^- current that the targets could produce.

The National Institute of Standards and Technology (NIST) standard reference material

^{36}Cl/Cl Ratio	Standard Supplier
4.16 x 10^{-11}	PRIME Lab[a]
4.42 x 10^{-12}	PRIME Lab[a]
1.20 x 10^{-12}	PRIME Lab[a]
4.08 x 10^{-13}	PRIME Lab[a]
1.48 x 10^{-11}	NIST[b]
1.52 x 10^{-12}	NIST[b]
7.18 x 10^{-13}	NIST[b]
1.59 x 10^{-13}	NIST[b]
7.3 x 10^{-14}	NIST[b]
1.2 x 10^{-14}	NIST[b]
3 x 10^{-15}	NIST[b]

Table 4.1: ^{36}Cl/Cl standards and dilution series measured by ISA-AMS. The supplier of the standards are listed. [a]PRIME labs AMS standard reference [51], [b]SRM 4943 [87]

(SRM) 4943 NaCl solution [87] was used for the dilution series to extend the ^{36}Cl/Cl ratios measured by the ISA beyond the 10^{-13} provided by the PRIME standards. The six ^{36}Cl/Cl ratios in the dilution series are listed in Table 4.1. This series also includes one blank material with a ^{36}Cl/Cl ratio in the 10^{-15} range. The preparation of the dilution series is detailed in Appendix A. The ratios were externally validated by 6 MV AMS measurement at Eidgenössische Technische Hochschule (Zurich, Switzerland) (ETH). The details of these measurements are in Section 4.1.0.1.

For all work in this chapter, the targets were an AgCl + Nb mixture at 1:3 ratio by volume. The AgCl precipitation and target preparation method are detailed in Appendix B

4.1.0.1 ETH measurements

The NIST SRM 4943 dilution series was sent to ETH for external measurement. At the ETH AMS facility, ^{36}Cl is measured on a 6 MV EN tandem accelerator [88]. It is measured with a terminal voltage of 5.8 MV and in the 7+ charge state. The blank level is a ^{36}Cl/Cl ratio of 2 x 10^{-15}.

Figure 4.1 compares the calculated ^{36}Cl/Cl ratio to the ratios measured by ETH. The theoretical ^{36}Cl/Cl ratio was calculated based on the calculated NIST SRM 4943 ratio of 7.28 x 10^{-2} [89] and the Pugwash chlorine ratio provided by Dr. John Gosse 5.05 x 10^{-15} [90]. This calculation is detailed in Appendix A.

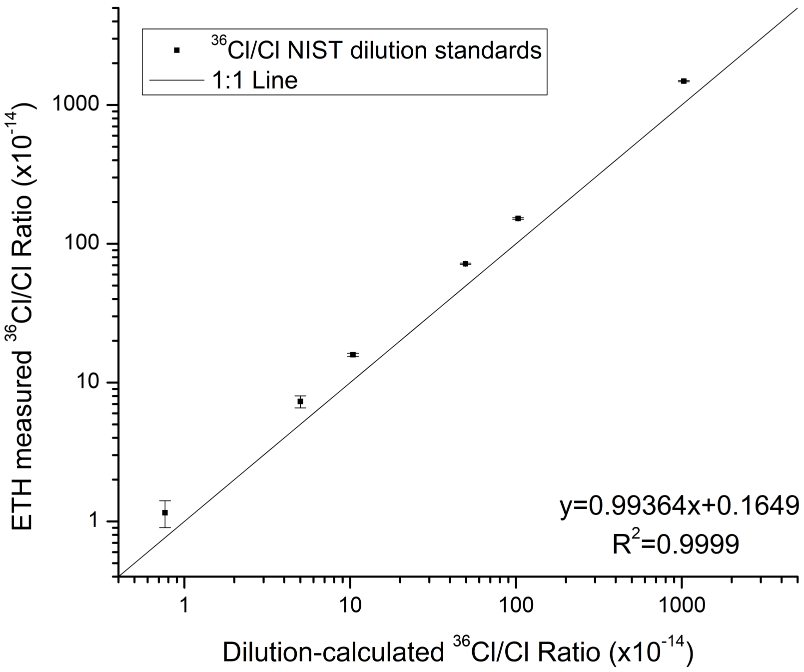

Figure 4.1: A comparison of the expected and the ETH measured values of the NIST SRM 4943 dilution series. The error bars are the standard deviation provided by ETH. The solid line represents the 1:1 agreement between the measured and expected value.

Figure 4.1 shows a systematic disagreement between the measured ratios and those calculated. The ETH measurements are consistently 30-40% higher than the ratios calculated from the parameters used in the dilution procedure detailed in Appendix A. This systematic difference could be due to the presence of excessive ^{36}S in the spectra. ETH has reported that their sample preparation method includes the chemical removal of excess S [91]. This is necessary to achieve their usual accuracy. The standards were simply precipitated using $AgNO_3$ and did not undergo chemical removal of S, so may contain excess ^{36}S. A mismeasurement of the mass of one of the high ratio dilutions, which required very small volumes of NIST SRM 4943, could also provide a systematic discrepancy in the calculated ^{36}Cl/Cl ratio.

4.2 Measurement method

Before measurement of ^{36}Cl standards, the method of measuring the stable isotopes needs to be determined. There are two relevant measurement modes available for batch analysis of samples on the AEL-AMS 3 MV system: slow sequential injection (SSI) and fast sequential injection (FSI). The injection timing of both methods is described in Section 2.2.3.1. In Sections 4.2.1- 4.2.2 their application to Cl measurement is discussed. Multiple criteria were used to test the suitability of each method. These include the predictability of the transmission through the beamline, the reproducibility of the technique across multiple targets of the same material, the precision on a single target, and the final ^{36}Cl/Cl ratios dependence on the ISA input current.

4.2.1 Slow Sequential Injection

SSI is the bouncing technique that allows seconds of time between the measurement of each isotope. To limit the total measurement time and the current injected into the ISA, only one stable beam was injected in each study. In the following sections, HE-SSI is used to designate the use of SSI with the stable Cl beam (either ^{35}Cl or ^{37}Cl) measured in the HE off-axis Faraday cups. These Faraday cups are included in Figure 4.2. In this case, one of the stable beams and the ^{36}Cl beam would both be injected into the ISA with 7.5 seconds of switching time between the two masses. LE-SSI, in which SSI would be used with the stable beam measured in a LE off-axis Faraday cup, was not tested as it is an inefficient data acquisition method and would likely provide no benefit over LE-FSI in the case of Cl measurements. The location of both sets of Faraday cups can be found in Figure 4.2.

4.2.2 Fast Sequential Injection

FSI is the bouncing technique that switches isotopes on a hundred of microsecond scale. Tests were completed with various bouncing schemes: injecting all three Cl isotopes, injecting just one stable and the rare isotope, and injecting only the rare isotope into the ISA. In the following sections, HE-FSI is used to designate the use of FSI with the stable beams (both ^{35}Cl and ^{37}Cl) measured in the HE off-axis Faraday cups. Similarly, LE-FSI is the

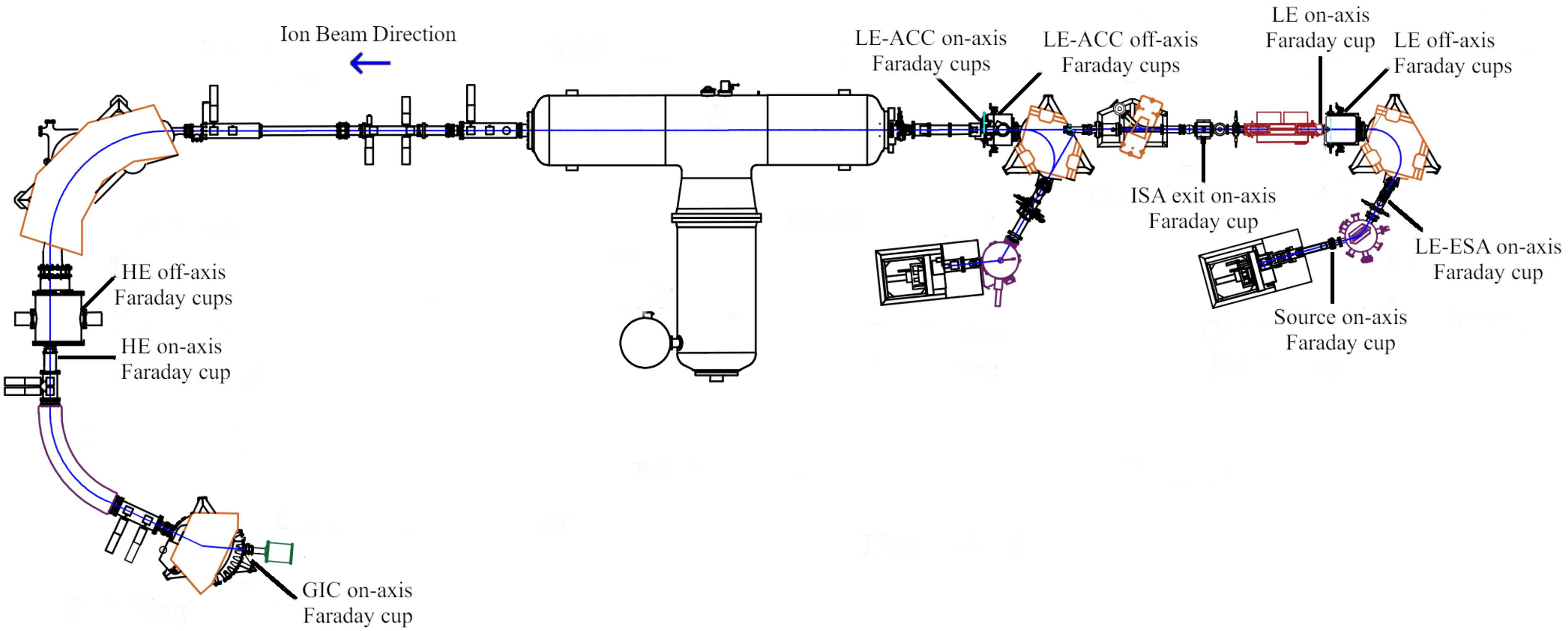

Figure 4.2: A schematic overview of the Faraday cups on the AEL AMS 3 MV system. All on-axis Faraday cups are retractable. The off-axis Faraday cups are mounted on rails such that the location of the cups is is externally adjustable using a hand wheel.

use of FSI with the stable beams measured in a LE off-axis Faraday cup, immediately after the injection magnet of the Research Line. In the case of LE-FSI, the stable beams are not injected into ISA. Instead, all bouncer voltages are set to inject ^{36}Cl into the ISA. Finally, HELE-FSI is used to designate when the stable beams are sequentially measured in both sets of Faraday cups and the ^{36}Cl/Cl ratio can be determined using the current from either Faraday cup set. Therefore, the stable Cl current is still injected into the ISA. All Faraday cups mentioned are included in Figure 4.2.

The use of the LE off-axis Faraday cups for the calculation of an isotopic ratio may be unique to the AEL-AMS 3 MV system. It is only possible to use these cups with FSI because the dispersion of the injection magnet is just sufficient to inject the ^{35}Cl^{-} and ^{37}Cl^{-} into their respective off-axis Faraday cups without blocking the ^{36}Cl^{-} counts.

4.2.3 Transmission analysis of measurement methods

If the percentage of beam transmitted through each portion of the beamline is known, it can be used to manually correct the raw ^{36}Cl/Cl ratio measured by each data acquisition method. The known transmission through the beamline, measured in DC mode (the bouncer is held at one voltage), and injection of only ^{37}Cl is detailed in Section 4.4. An approximate percentage of the ^{36}Cl^{3+} counts included in the ROI in the GIC is also needed. Some ^{36}Cl^{3+} counts are lost, due to the ROI being selected to gain additional separation from ^{36}S^{3+}. This can be seen in Figure 4.9.

ISA-AMS runs measuring the ^{36}Cl/Cl ratio of the 4.16 x 10^{-11} PRIME Lab standard were completed using a variety of data acquisition modes. The measurement methods detailed in Sections 4.2.1 and 4.2.2 were each used. At the ISA entrance, the ^{35}Cl beam was typically in the 1-12 μA range and the ^{37}Cl was in the 0.5-4 μA range.

To determine if the beam is behaving as expected, the raw ^{36}Cl/Cl ratio must simply be multiplied by the percent transmission of each section that the ^{36}Cl counts traverse but the stable Cl does not. Therefore, for the methods in which the stable beam is measured in the HE Faraday cups, the raw ^{36}Cl/Cl ratio needs to be multiplied by the 92% transmission from the HE Faraday cups to the GIC detector and the estimated 75% of the ^{36}Cl^{3+} counts included in the GIC ROI. For the measurement methods in which the stable beams are

Data Acquisition Mode	Average Raw ^{36}Cl/^{35,37}Cl Ratio (x10^{-11})	Transmission Corrected ^{36}Cl/Cl Ratio (x10^{-11})	$\frac{Corrected}{4.16x10^{-11}}$
HE-FSI (35)	2.4 ± 0.4	2.7 ± 0.4	0.6 ± 0.1
HE-FSI (37)	5.4 ± 0.8	1.9 ± 0.3	0.45 ± 0.07
HELE-FSI (HE-35)	1.3 ± 0.1	1.5 ± 0.1	0.35 ± 0.03
HELE-FSI (HE-37)	4.3 ± 0.4	1.5 ± 0.1	0.36 ± 0.03
HELE-FSI (LE-35)	0.64 ± 0.02	6.7 ± 0.2	1.60 ± 0.04
HE-SSI (35)	1.64 ± 0.05	1.80 ± 0.05	0.43 ± 0.01
HE-SSI (37)	3.08 ± 0.05	1.08 ± 0.02	0.260 ± 0.004
LE-FSI (35)	0.40 ± 0.02	4.1 ± 0.2	0.99 ± 0.05

Table 4.2: The transmission analysis of data acquisition modes. Each mode is listed with the isotope used to calculate the raw ratio included in brackets. When both the HE and LE Faraday cups were used to measure the stable beam, the Faraday cup set used is also listed. At the ISA entrance the ^{35}Cl beam was typically in the 1-12 μA range and the ^{37}Cl was in the 0.5-4 μA range. The fourth column is the ratio of the third column over the known ^{36}Cl/Cl ratio of the standard being measured.

measured in the LE Faraday cups, the ratios need to additionally be multiplied by the 30% transmission through the ISA and the 35% transmission through the accelerator.

The raw and transmission corrected ratios of each of the data acquisition techniques are listed in Table 4.2. Next to each data acquisition mode the stable isotope used to calculate the raw ratio is included in brackets. When both the HE and LE Faraday cups were used to measure the stable beam, as in the case of the HELE-FSI method, the Faraday cup set used is also listed in brackets. This method still has the stable beam injected into the ISA, so is similar to the HE-FSI method. However, both the HE and LE Faraday cups were positioned to measure the stable beam. Both cups could then be separately used to determine a ^{36}Cl/Cl ratio.

Table 4.2 compares the transmission corrected ratio to the nominal value of the standard; these numbers should be in close agreement if the measurement method is behaving in a predictable way. In each data aqcuisition mode that measures the stable Cl beam after it passes through the ISA, the corrected value does not agree with the nominal value. The only measurement method that behaves in a predictable way is the LE-FSI, where the stable beam is not injected into the ISA, with a ratio of ‘Transmission Corrected’ to Standard value of 0.99.

4.2.4 Reproducibility of measurement methods

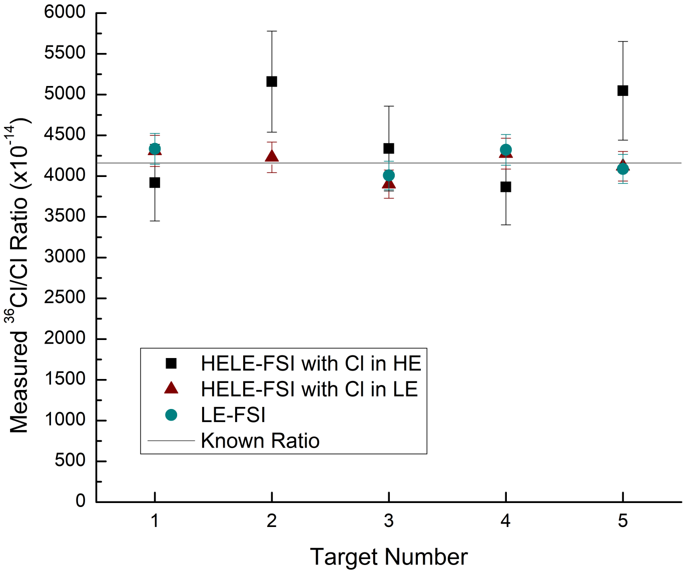

Figure 4.3: The reproducibility of the data acquisition modes. The ratio of four or five targets of the same material are compared. The straight line is the nominal ratio of the 4.16 x 10^{-11} PRIME Lab standard. For measurement details see text.

Four or five different targets (depending on the data acquisition mode) of the 4.16 x 10^{-11} PRIME Lab standard were measured using three FSI methods to measure ^{35}Cl. Figure 4.3 shows the calibrated ^{36}Cl/Cl ratio measured by each method. The black squares used ^{35}Cl^{3+} measured in the HE cup to determine the ratio. The red triangles use the same HELE-FSI measurement method but the ^{35}Cl^{-} measured in the LE Faraday cup is used. Finally, the blue circles do not have any stable current entering the ISA and use the ^{35}Cl^{-} measured in the LE Faraday cup.

Figure 4.3 shows larger scatter between each target of the same material when the Cl current is measured through the ISA in the HE Faraday cup. Table 4.3 shows these same values, along with the measurement precision on each target. The error on a single target is again higher when the Cl current is measured in the HE Faraday cup.

Mode of data acquisition	Single target measurement precision (%)	Intertarget scatter (%)
HE-FSI (HE 35)	12	24
HELE-FSI (LE 35)	4.5	6.5
LE-FSI (LE 35)	4.5	4.5

Table 4.3: The reproducibility of the data acquisition modes through the precision on a single target and the scatter between four or five targets of the same material. Each mode is listed with the isotope and Faraday cup used to calculate the ratio included in brackets. The second column is represented by the error bars in Figure 4.3 and the third column is represented by the difference between each point in the same figure.

4.2.5 Current dependence of measurement methods

It is important that the amount of current injected into the ISA does not affect the measured ^{36}Cl/Cl ratio. Samples can produce targets with variable currents and therefore a range of injected currents must produce the same ratio. To test this, three sets of targets were made with a variable mixture of 4.16 x 10^{-11} PRIME lab standard and Nb. These ratios were 1:2, 1:11, and 1:43 by volume.

The results of the measurement of these targets are shown in Table 4.4. The input current of ^{35}Cl^{-} was not measured in the HE-FSI and HE-SSI measurements, so the ^{35}Cl^{3+} value is provided. However, the current used to determine the ^{36}Cl/Cl ratio can be used to indicate an increase in input current. In both FSI measurements, the ^{37}Cl current was recorded in the same location as the ^{35}Cl and was used to determine the ^{37}Cl/^{35}Cl. The ^{37}Cl current was not used to determine the ^{36}Cl/Cl ratio so is not provided in Table 4.4.

HE-FSI			**HE-SSI**					**LE-FSI**		
^{35}Cl^{3+} current (nA)	Normalized ^{36}Cl/Cl	$\frac{^{37}\text{Cl}}{^{35}\text{Cl}}$	^{35}Cl^{3+} current (nA)	Normalized ^{36}Cl/Cl	^{37}Cl^{3+} current (nA)	Normalized ^{36}Cl/Cl	$\frac{^{37}\text{Cl}}{^{35}\text{Cl}}$	^{35}Cl^{-} current (nA)	Normalized ^{36}Cl/Cl	$\frac{^{37}\text{Cl}}{^{35}\text{Cl}}$
419	0.64 ± 0.01	0.45	489	0.43 ± 0.01	350	0.259 ± 0.005	0.53	726	1.06 ± 0.01	0.32
110	0.37 ± 0.01	0.31	97.2	0.318 ± 0.008	57.4	0.287 ± 0.007	0.35	156	0.99 ± 0.02	0.31
26	0.47 ± 0.02	0.36	3.31	0.45 ± 0.05	4.72	0.46 ± 0.02	0.31	14.9	1.12 ± 0.05	0.31

Table 4.4: The dependance of the ^{36}Cl/Cl ratio on the data acquisition mode and the input current. The ^{36}Cl/Cl ratio is normalized to the nominal ^{36}Cl/Cl ratio of the target, 4.16 x 10^{-11}. The HE or LE designates the location of the Faraday cups used to measure the stable Cl beam. The measured ^{37}Cl/^{35}Cl ratio is included with a nominal value of 0.32.

For each method, the ^{36}Cl/Cl ratio is normalized to the nominal ^{36}Cl/Cl ratio of the target, 4.16 x 10^{-11}. Ideally, these ratios will all be close to 1. Table 4.4 clearly shows that the ^{36}Cl/Cl ratio from the HE-FSI and HE-SSI methods are not stable under a change in input current. In both cases, the ^{37}Cl/^{35}Cl ratio is also dependent on the input current; high currents lead to large discrepancies in even the stable Cl ratio.

The LE-FSI methods do not have stable current injected and therefore the final ratio does not have any dependence on the stable beam current. All three targets resulted in similar ^{36}Cl/Cl ratios. The stable ^{37}Cl/^{35}Cl ratios are close to the known value of 0.32.

4.2.6 Space charge effects

With all previous tests indicating that the stable Cl beam cannot be injected into the ISA, the dependence of the ISA transmission on the input currents needed to be studied. The low eV energies of the anions within the ISA cell could lead to transmission variation due to space charge effects. The slow-moving anions can form a negative charge cloud that will repel other anions and limit the transmission through the ISA.

To determine the maximum beam intensity that can be injected into the ISA without additional transmission loss, the current injected was varied and the outgoing current was measured. Figure 4.4 shows the ISA transmission has a strong dependence on the incoming current. An incoming ^{37}Cl$^-$ beam was measured in the LE off-axis Faraday cup. The outgoing ^{37}Cl$^-$ was measured in the GIC Faraday cup. The ISA settings were optimized for an incoming current of 160 nA.

A range of linear transmission as a function of current can be seen at lower input currents in Figure 4.4 for the ISA cell filled with just He (13.7 μbar) and with a mixture of He and NO_2 (11 μbar and 10.8 μbar, respectively). These are indicated by solid lines. Transmission losses due to space charge effects begin to occur around 300 nA of incoming current, indicated by a dashed line in Figure 4.4. This effect has been demonstrated with other RFQ beam coolers at currents in the hundreds of nA [92].

If a stable beam current of 300 nA or less was used for measurement of ^{36}Cl ratios, there would insufficient counts for the rare radioisotope. The limitation on incoming current means

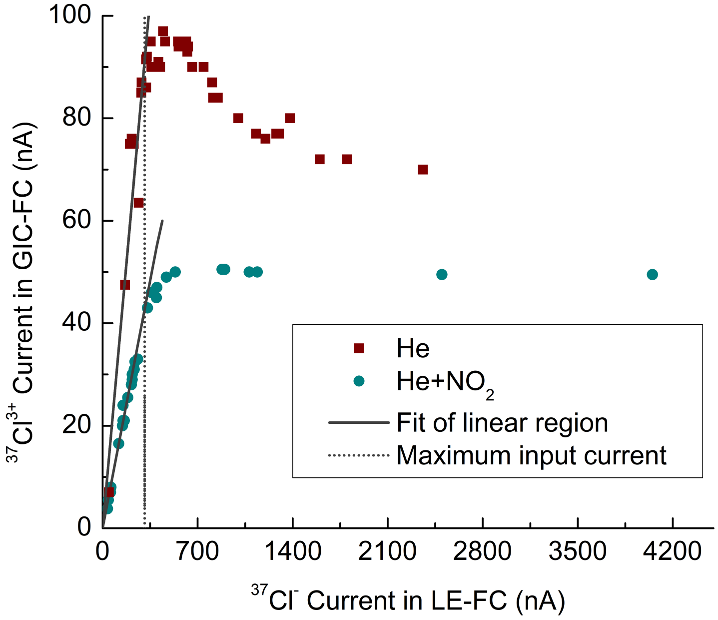

Figure 4.4: Outgoing ^{37}Cl current for various ^{37}Cl currents entering the ISA. The LE-FC is the off-axis Faraday cup at the entrance of the ISA and the GIC-FC is the Faraday cup preceding the GIC. An extension of the linear region is included as a solid line. A dashed line indicates the current at which the transmission deviates from linearity. [81]

that injection of the full stable beam current must be avoided. This can be accomplished either through attenuation of the stable beam before injection or by measuring the stable beam current prior to the ISA.

4.2.6.1 Space charge effect in Configuration 4

Figure 4.5 shows the transmission of a beam with varying incoming beam currents using 13.7 μbar of He in the cell. In this test, the incoming current was measured using an LE off-axis Faraday cup. The outgoing current was measured using the ISA-exit on-axis Faraday cup. This curve shows a lower space charge limit than Configuration 3, with departure from the straight line around 200 nA input current.

The Configuration 4 curve does appear smoother than the original test. This could be due to improved transmission or due to the measurement technique. In the first study, the GIC on-axis Faraday cup was used for measurement. This may result in beam losses

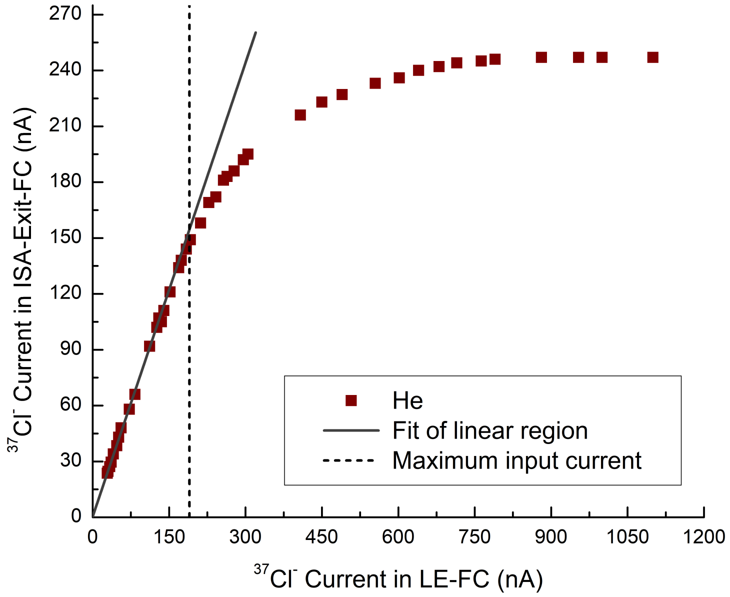

Figure 4.5: Outgoing ^{37}Cl current for various ^{37}Cl currents entering the ISA using the ISA Configuration 4. The ISA-Entrance-FC is the off-axis Faraday cup at the entrance of the ISA and the ISA-Exit-FC is the on-axis Faraday cup at the exit of the ISA. An extension of the linear region is included as a solid line. A dashed line indicates the current at which the transmission deviates from linearity.

elsewhere in the system. Additionally, a variety of targets were used to produce the range of incoming currents in the Configuration 3 tests. In the Configuration 4 tests, it was possible to use one target with a gradually increasing Cs temperature that resulted in the necessary incoming current range. The method used in Configuration 3 tests may result in changes in phase space that alter the transmission through the ISA.

4.2.7 Additional notes

Measurements were also completed to determine if altering the order of the isotopes during bouncing in FSI would make measurement of the stable isotopes using the HE Faraday cup viable. The masses injected and the order they are injected in can be controlled by the user. Bouncing between mass 35, 36, and then 37 resulted in a ^{37}Cl/^{35}Cl ratio of 0.34 in the HE cups. Bouncing 35, 37, and 37 resulted in a ^{37}Cl/^{35}Cl ratio of 0.48 in the HE cups and bouncing 35, 35, and 37 resulted in a ^{37}Cl/^{35}Cl ratio of 0.28 in the HE cups. None of these methods resulted in a viable technique for injecting the stable Cl beam.

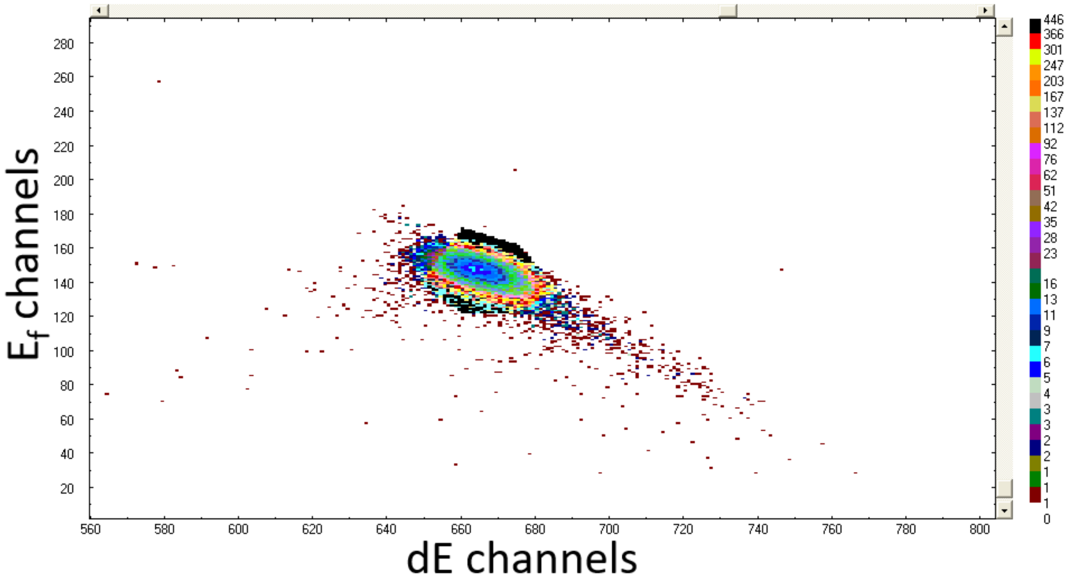

Figure 4.6: ^{36}Cl spectrum when stable Cl is injected into the ISA. The large tail is due to scattered ^{35}Cl and ^{37}Cl reaching the detector while the detector gate is open.

Bouncing the stable beam also led to additional features within the GIC spectrum. A large tail can be seen on the ^{36}Cl peak in Figure 4.6. This tail is the result of scattered ^{35}Cl and ^{37}Cl reaching the detector while the detector gate is open. This likely occurs due to the prolonged residence time the Cl beam has in the ISA compared to the rest of the beamline. This residence time may be on the order of tens of ms while the bouncing and opening of the detector gate is on the scale of hundreds of μs. When measuring in the 4+ charge state, an ^{18}O^{2+} peak was visible but only when bouncing the stable beam through the ISA.

4.2.8 Conclusion

Due to the low energy of the ions in the ISA, their residence time inside the ISA is much longer (ms) than in any other component along the beamline. Future work may quantify this residence time. It was hoped that using SSI, which increases the time between injected isotopes to the ms range, would remove the effects of this seen in the spectra. While it did show improvement in the final spectrum, it also showed a dependence on the injected current.

The low energy of the ions in the ISA also cause space charge effects. These effects were present in every injection method with the stable beam injected into the ISA. This meant that only the injection methods that measured the stable beam in the LE Faraday cups behaved in a predictable way and resulted in better precision and reproducibility. Therefore, all measurements of ^{36}Cl/Cl in this thesis were completed using the LE Faraday cups for the stable beam and the GIC for the rare beam. This was facilitated by the low-energy 120° injection magnet and off-axis Faraday cups on the Research Line. This method uses the more efficient injection method, FSI, with only the mass 36 counts entering the ISA. FSI must still be used despite continuous injection of only one mass to enable the gates to the GIC for measurement and enable the recording of the currents measured by the Faraday cups. The fact that all masses are not treated the same way is largely accounted for by calibrating the radioisotope to stable ratio to standards of a known ratio. However, it cannot account for any variations that occur due to fluctuations along the beamline or of the accelerator that would only affect the rare radioisotope measurement.

A beam attenuator could also be used to limit the current injected into the ISA without the disadvantage of treating the rare and stable beam differently. Using a beam attenuator must not alter the beams phase space and requires measurements to be completed using SSI, significantly increasing the measurement time of each target to achieve sufficient counts of the radioisotope. It would also require that control of the attenuator be integrated into the AMS system control software to synchronize it with the bouncer (Section 2.2.3.1). Future work may include adding a beam attenuator to the Research Line or a bypass system in which the stable beams would adopt a trajectory parallel to the ISA.

4.3 Tuning procedure for ^{36}Cl

To begin the tuning procedure for ^{36}Cl, a ^{37}Cl beam of less than 250 nA is used. The ^{35}Cl and ^{37}Cl only need to be tuned to the LE off-axis Faraday cups after the LE injection magnet on the Research line. The ability to move stepwise along the line make it much easier to tune using a current and the Faraday cups than using the counts of the rare isotope that only the GIC can detect.

If the settings of components along the beamline are available from a previous tune of ^{37}Cl, they are loaded and used as a starting point. Previous settings used for the measurement of ^{36}Cl using the HE-FSI measurement method are found in Appendix C. These include the settings used for all components along the beamline, the slit and aperture settings, and the ISA settings.

The ^{37}Cl can then be guided through the beamline using each subsequent Faraday cup, shown in Figure 4.2. Faraday cups are located before and after the Research line ESA, at the entrance and exit of the ISA, at the entrance of the accelerator, after the HE analyzing magnet, and before the GIC. The setting of each ion optical and deflecting component is scanned using the HVEE software. The scanning software allows the user to set the range of voltages or currents to be scanned on this component, the number of point within that range (thus setting the step size), and the Faraday cup measuring the ^{37}Cl beam current. This results in a scan of beam current for each step in voltage or current set on the component. The user can then select the setting that provides the highest beam current into the Faraday cup into which the beam is currently being optimized. The beam is optimized stepwise along the beamline until the ^{37}Cl beam current is optimized into the GIC.

In addition to optimizing for maximum current into the Faraday cups, the user can also use a beam profile monitor (BPM). The BPM displays a plot of the intensity of the beam as a function of its position along the two axes perpendicular to the beam direction. There are two along the beamline: one at the accelerator entrance and one after the HE analyzing magnet. Figure 4.7a) and c) show the beam profile at the accelerator entrance BPM and after the analyzing magnet, respectively. The peaks represent the horizontal and vertical profiles of the beam. Figure 4.7b) and d) show the respective beam cross section for those same BPMs. Ideally, the beam should have a small, intense cross section, as shown in Figure 4.7 and should be near the centre of the plot. The beam profiles should have similar heights and should align with the vertical lines in the plot region. The slight displacement of the beam at the accelerator entrance BPM is seen consistently and may be a result of a misalignment of the BPM.

As described in Section 2.3.1.1, the components of the ISA that are at the potential of

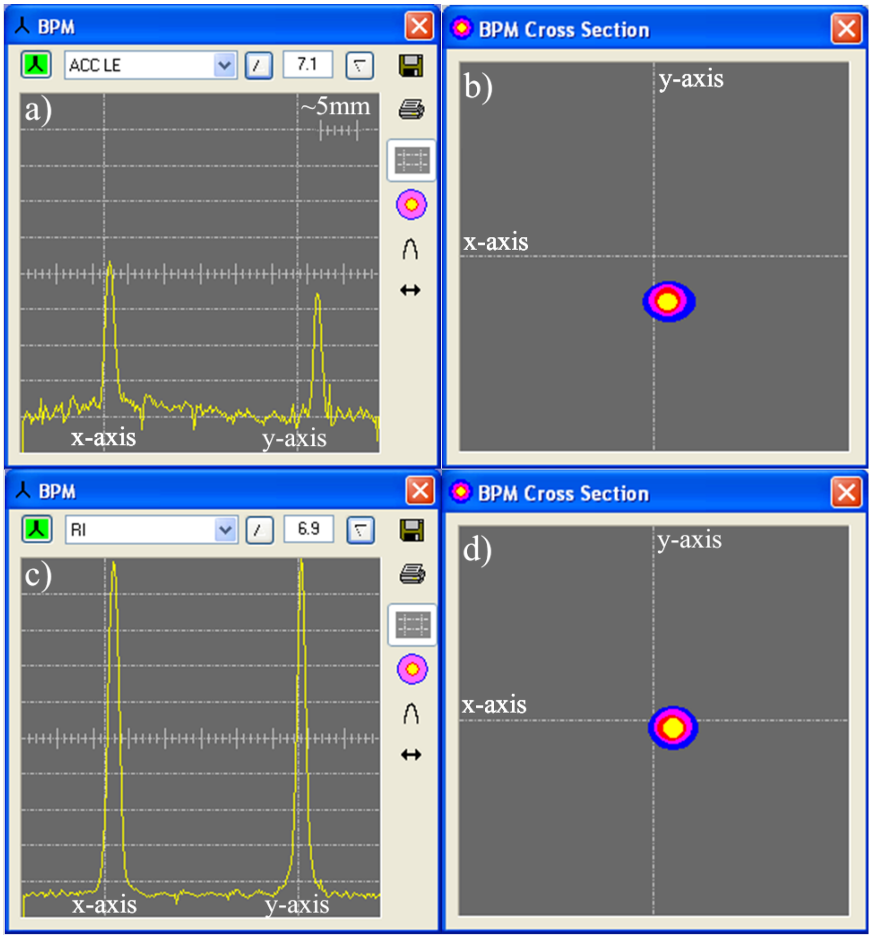

Figure 4.7: Beam profile monitor during tuning with ^{37}Cl. a) and b) are the beam profile and cross section at the entrance of the accelerator, respectively. c) and d) are the beam profile and cross section after the HE analyzing magnet, respectively. This was generated with the slits at 10.00 mm by 10.00 mm. Small divisions on the scale are approximately 1 mm.

the high voltage deck are controlled by a separate control computer. Therefore, the HVEE scanning program cannot be used on the ISA components. To tune into each Faraday cup following the ISA, previous settings are first loaded into the ISA control system. From this point, the voltage on each component is manually adjusted while the user watches the resulting changes in current reading from the Faraday cup of interest. The setting that produces the highest current value is selected.

After optimization of all beamline components has been completed for ^{37}Cl up to the GIC Faraday cup, the settings are saved. To tune for ^{36}Cl, the settings found for ^{37}Cl are used with adjustments to components affected by the change in mass. This rescaling only includes the HE analyzing magnet and the switching magnet. If a different charge state was selected, additional adjustments would include the HE ESA. To rescale the magnetic field on both magnets the following equation is used:

$$B(^{36}Cl) = B(^{37}Cl)\sqrt{\frac{35.969}{36.966}} \tag{4.1}$$

Rescaling is not required on the LE injection magnet because to tune, the bouncer is put in 'DC mode' which keeps the bouncer voltage constant on the setting for ^{37}Cl. Therefore, the change in mass will be accounted for by changing the bouncer voltage to that for ^{36}Cl instead of having to scale the magnetic field found through the original optimization of all beamline components.

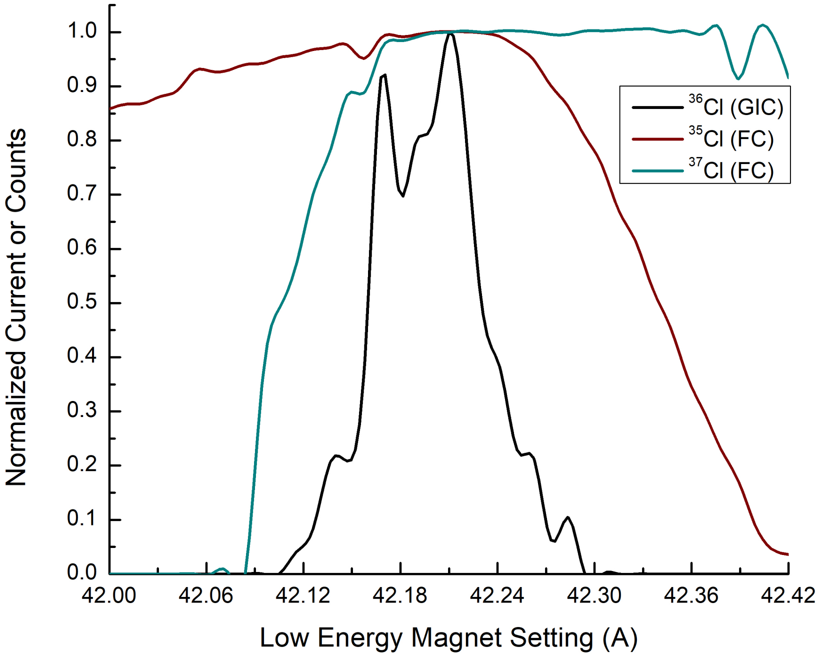

Figure 4.8: A scan of the LE magnet setting to optimize the stable beam current in the LE Faraday cups (FC) and the rare beam count rate in the GIC. Only the rare beam is passing through the ISA.

After rescaling is complete, the magnets and the HE ESA should still be optimized using the HVEE scanning program. However, the optimization is now completed using the ^{36}Cl counts in the GIC. It is also beneficial to check the tune on the LE injection magnet. Figure 4.8 shows the scan that should be found while adjusting the magnet setting and measuring all three isotopes. The ^{36}Cl is measured as counts in the GIC, and the ^{35}Cl and ^{37}Cl are measured in the off-axis Faraday cups after the LE injection magnet. To ensure that the peak of all 3 isotopes overlap for one magnet setting, the location of the two off-axis Faraday cups can be adjusted to capture the total stable beam current. Note that due to the proximity of the enclosures of the LE off-axis Faraday cups to the central beam axis in Cl isotope analysis, care should be taken not to cut off any of the ^{36}Cl beam. This proximity means that only the ^{35}Cl is used to determine the final ^{36}Cl/Cl ratio, so it is prioritized over ^{37}Cl. However, having both ^{35}Cl and ^{37}Cl will allow for monitoring the beam from the source throughout the run.

4.4 Transmission through the beamline

The transmission from one Faraday cup (FC1) to the next Faraday cup (FC2) was measured along the beamline. Knowing the average transmission between each Faraday cup can help with the tuning process. The transmission is calculated using:

$$T = \frac{Q_{FC1} * I_{FC2}}{Q_{FC2} * I_{FC1}} \tag{4.2}$$

where Q is the charge state of the ions and I is the current measured at the respective Faraday cup. The transmission along the beamline is detailed in Table 4.5 with each Faraday cup being compared to the current at the LE on-axis Faraday Cup. The transmission through the ISA is for typical running pressures of 10.8 μbar of NO_2 and 11 μbar of He. The transmission through the accelerator is for the 3+ charge state. There are two additional Faraday cups along the Research Line that are not included in this Table: the Source on-axis Faraday cup and the LE-ESA on-axis Faraday cup. The beams measured by these two Faraday cups are not mass analyzed and therefore will not provide transmission of the mass 36 beam.

There is no Faraday cup at the exit of the accelerator, prior to injection in the HE

Faraday Cup	Expected Cl Transmission from ISA Entrance Faraday Cup (%)
ISA exit on-axis	30.0
LE-ACC on-axis	28.5
HE on-axis	10.0
GIC on-axis	9.2

Table 4.5: Transmission of stable Cl along the beamline. The percentages are calculated from the current at the ISA entrance Faraday cup. The transmission through the ISA is for 10.8 μ bar of NO_2 and 11 μ bar of He. The transmission through the accelerator is for the 3+ charge state.

analyzing magnet. Therefore, all cations exiting the accelerator at the settings used cannot be measured without scanning the magnetic field of the HE analyzing magnet. However, the accelerator transmission may still be measured for the specific charge state.

The transmission values in Table 4.5 show that the majority of the transmission losses occur through the ISA and the accelerator. The transmission through the accelerator is based on the charge state yield discussed in Section 4.4.1. Less than 10% of the mass 36 beam injected into the ISA is observed in the ROI of the GIC. This is slightly lower than other facilities measuring ^{36}Cl [17, 91]

4.4.1 Charge state yield

The positive charge state yield out of the accelerator stripping gas column depends on the energy of the beam and the stripping medium (gas or foil). When gas is used as the stripper, the gas type and pressure will affect the charge state yield. Higher beam energies are required for the use of foil but often result in an increased yield for higher charge states. Therefore, ^{36}Cl is often measured in the 5+ charge state or higher, with foil used for stripping at larger facilities [88, 93, 94]. At the time of measurement, Ar gas was the only available stripping medium on the 3 MV accelerator; a recent upgrade has added He gas.

On the 3 MV AEL-AMS system, isotopes are typically measured in the 2+ to 4+ charge state. For ^{36}Cl measurement, the 4+ charge state was tested at a terminal voltage of 2.5 MV. This afforded some dE/dx separation between ^{36}S and ^{36}Cl in the detector. However, selecting the 3+ charge state with a terminal voltage of 3 MV results in similar dE/dx separation but with a higher transmission through the accelerator. Measurements in this work were therefore completed with these settings.

While a higher transmission is possible in the 2+ charge state, molecular isobars can remain stable in the 2+ charge state but have not been observed in the 3+ charge state or higher. This may result in interferences from the isotope $^{18}O_2$ in the 2+ charge state. Lachner et al. [63] found that these molecules were destroyed by laser photodetachment in the ILIAMS. The electron affinities of O is 1.46 eV [80]; it is likely that it would also be removed from the beam in the ISA.

A stripper gas pressure of 1.2 x 10^{-2} mbar was selected based on the pressures used for other isotopes studied using the 3 MV AEL-AMS system. Future tests should include a study of the charge state yield for a range of stripper gas pressures. However, this can be a time-consuming study, as time is needed for the stripper gas pressure to equilibrate.

4.5 Chlorine-36 detection

The $^{36}Cl^{3+}$ is counted in the GIC, discussed in Section 2.6.2. With the terminal voltage set to 3 MV, the $^{36}Cl^{3+}$ arrives at the detector with an energy of approximately 12 MeV. This provides partial dE/dx separation between the $^{36}Cl^{3+}$ and the remaining $^{36}S^{3+}$ in the detector, shown in Figure 4.9. The location of the $^{36}S^{3+}$ and the $^{36}Cl^{3+}$ are labelled in the figure. Some $^{36}Cl^{3+}$ is not included in the ROI to avoid counting $^{36}S^{3+}$ but at least 75% of the ^{36}Cl counts lie within the ROI.

Measurements in this work used a GIC pressure of 15 μbar for $^{36}Cl^{3+}$ at 12 MeV. Figure 4.9 shows the $^{36}Cl^{3+}$ spectrum using 15 μbar of isobutane. Future work could test if separation between $^{36}S^{3+}$ and $^{36}Cl^{3+}$ in the GIC is improved using with a change in isobutane pressure.

4.6 Measurement Routine

Batch mode is used in the HVEE software to set up a measurement. A batch can include up to 200 targets. It can be set to complete one or more ‘passes’ of these targets. A pass consists of multiple measurement blocks on each target. In each measurement block, the

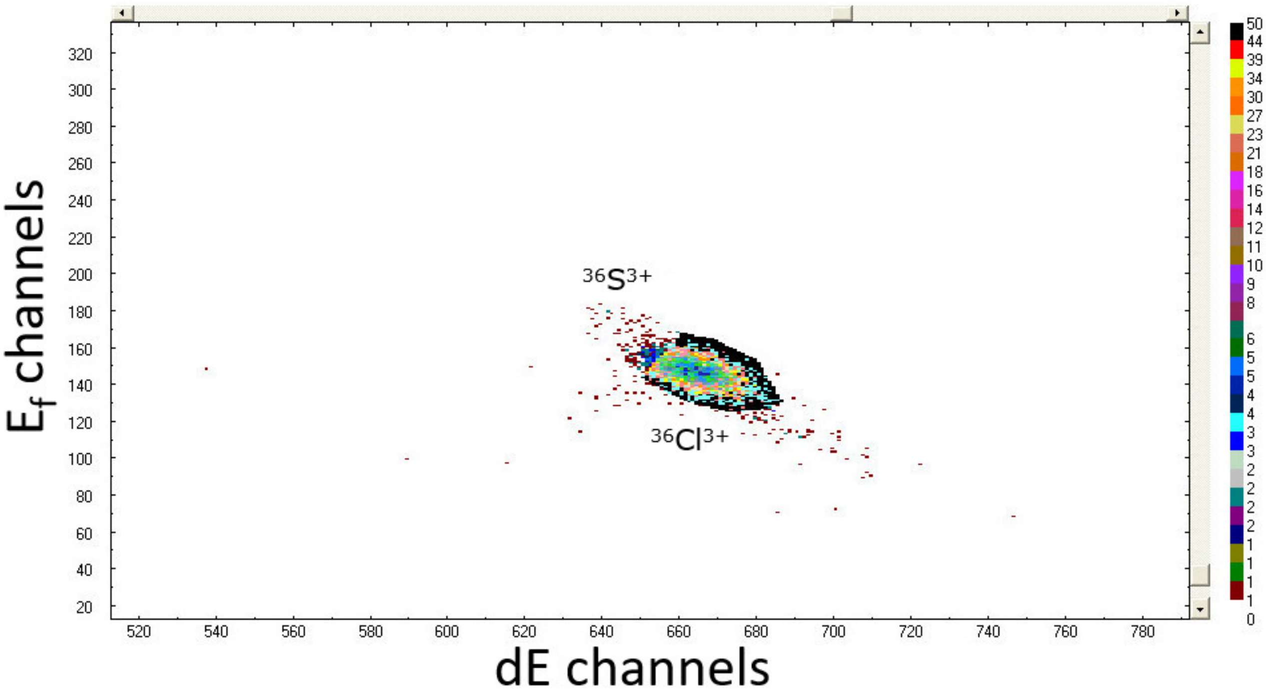

Figure 4.9: Isobar separation between $^{36}S^{3+}$ and $^{36}Cl^{3+}$ in the GIC using 15 μbar of isobutane.

average rare isotope count rate and stable isotope currents are recorded. The user can set the time length of a block and the number of blocks on each target. After that number of average count rates and currents have been recorded on one target, the source will move onto the next target until each target in the target list has been measured, making one complete pass. The number of passes can also be adjusted by the user. Measurement of ^{36}Cl uses 30 second blocks and typically consists of 1 pass of 10 blocks completed to condition each target. The data from this first pass is not used to determine the ^{36}Cl/Cl ratio. After this pass, the subsequent passes are set to 50 blocks of 30 seconds. Three to four passes are completed on each target. Therefore, the total measurement time per target is 75 to 100 minutes.

4.7 Data Reduction

At the time of measurement, raw data from a completed run was loaded into an AEL-AMS 3 MV data reduction Excel workbook created by Dr. Xiaolei Zhao. A recent upgrade to the

AEL-AMS 3 MV software will change the raw data file output and therefore the method of data reduction. In this work, the data is output as one row per block measurement for a sample. Typical runs include 100 blocks per sample or more. Each block contains the $^{36}Cl^{3+}$ counts, the average $^{35}Cl^{-}$ current, the average $^{37}Cl^{-}$ current, and the raw $^{36}Cl^{3+}/^{35}Cl^{-}$ ratio. For each target, there are K blocks or K data points of $R_i \pm \Delta R_i$, where R_i is the raw $^{36}Cl^{3+}/^{35}Cl^{-}$ ratio for sample i,and ΔR_i is the statistical error in that ratio. The statistical error is determined by the number of counts for each R_i.

All points are then plotted within the Excel workbook and the arithmetic mean, standard deviation, average counting error per block, scatter of the mean, counting error for the mean, and chi-squared test are calculated. These are used for quality assurance and inspection of the stability of the measurement and provides an easy way to identify outliers within the data.

After removal of outliers in the raw data, machine blanks are subtracted from the sample raw data. The weighted mean of all blocks is then calculated for each sample using the equation:

$$\overline{R} = \frac{\sum_{i=1}^{K} \frac{R_i}{(\Delta R_i)^2}}{\sqrt{\sum_{i=1}^{K} \frac{1}{(\Delta R_i)^2}}} \tag{4.3}$$

where R_i is the raw ratio of sample i, K is the number of blocks for that sample, and ΔR_i is the error calculated based on the statistical error for sample i given by:

$$\text{statisticalerror}(\%) = \frac{1}{\sqrt{N}} \tag{4.4}$$

where N is the number of counts. This error is used as σ when only a single measurement is completed. The standard deviation is then calculated based on the equation:

$$\sigma = \sqrt{\frac{\sum_{i=1}^{K} \frac{(R_i - \overline{R})^2}{(\Delta R_i)^2}}{\frac{(K-1)}{K} \sum_{i=1}^{K} \frac{1}{(\Delta R_i)^2}}} \tag{4.5}$$

The standards are then labelled and a calibration factor is calculated using their measured ^{36}Cl/^{35}Cl and their known ^{36}Cl/^{35}Cl ratios. The same calibration factor is applied to all other raw ratios and their error is adjusted according to the propagation of the calibration factor. To determine the ^{36}Cl/Cl ratio, the ^{36}Cl/^{35}Cl ratio is divided by 0.7578 to account for the natural abundance of Cl isotopes [43].

If more than one target is used for each sample, the weighted average (Equation 4.3) and the standard deviation of these targets (Equation 4.5) are calculated and reported with 1σ confidence limit. The statistical error for each targets can also be reported calculated using Equation 4.4.

4.8 Calibration curve linearity

A calibration curve is the set of calibration factors (the nominal isotope ratio /the measured ratio) over the range of ratios of interest. If experimental conditions are consistent for all samples, this curve should be linear. Calibration factors for the ^{36}Cl/Cl ratios were compiled by measuring two sets of reference materials based on the dilution of 2 standards, detailed in Sections 4.8.1 and 4.8.2, with ^{36}Cl/Cl ratios on the order of 10^{-15} to 10^{-11}.

During both measurements, the stable beam was measured in the LE Faraday cups after the research line injection magnet. The rare ^{36}Cl counts were measured in the GIC. The ^{37}Cl and ^{35}Cl had currents ranging from approximately 0.5-4 μA and 1-12 μA, respectively. The ISA cell used 10.8 μbar of NO_2 and 11 μbar of He. The accelerator terminal voltage was set to 3 MV and the 3+ charge state was selected.

The ratios were determined using the $^{36}Cl^{+3}$ counts and the $^{35}Cl^{-}$ current. This was multiplied by 0.7578 to account for the natural abundance of Cl isotopes [43]. In both measurements, the calibration factor was determined for the highest ratio standard and applied to all standards.

4.8.1 PRIME Lab standards

The calibration curve of Figure 4.10 shows the weighted average of two targets for each of the four PRIME Lab reference standards listed in Table 4.1. The error bars are the standard deviation of the mean calculated using Equation 4.5. The solid line shows the points at which the ISA measured values are equal to the nominal values provided by PRIME Labs.

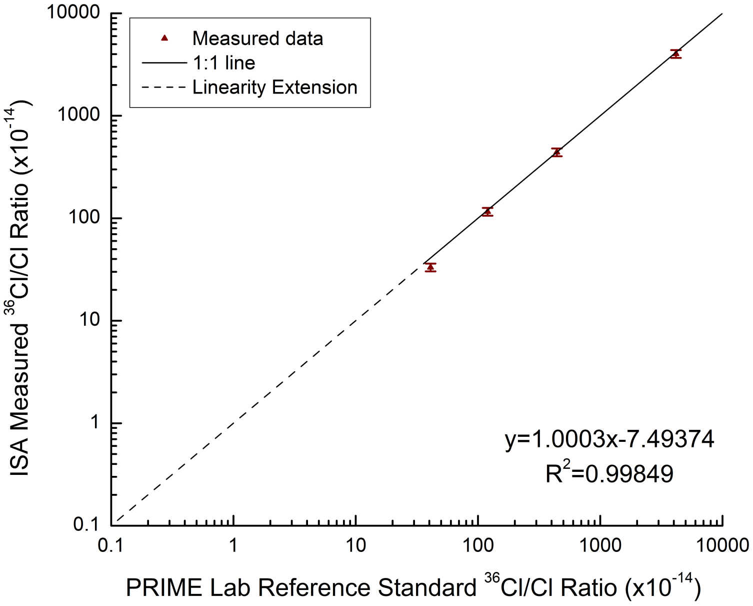

Figure 4.10: A comparison of the ISA-AMS measured values and the nominal value of the PRIME Lab set of four standards. The measured results were calibrated to the nominal value of the highest ratio PRIME Lab standard. Each point represents an average of two targets. The error bars are the standard deviation of the mean. The solid line represents the 1:1 agreement between the measured and nominal value. The dashed line represents the additional region of interest not covered by this standard series.

Good agreement was found between the ISA measured ratios and the nominal values from PRIME Lab. The results of a linear regression showed a slope of 1.0003, very close to the ideal value of 1 and an R^2 value of 0.998. This is further illustrated in Table 4.6, where the values for ratios above 10^{-13} agree within one standard deviation and have percent differences less than 3.5%. This percent difference is increased to approximately 19% for

Provided ^{36}Cl/Cl Ratio (x10^{-14})	ISA-AMS Measured ^{36}Cl/Cl Ratio (x10^{-14})	Statistical Error (%)	Standard Deviation (%)	Percent Difference (%)
4160	4020	0.3	8.7	3.4
442	441	0.9	8.6	0.2
120	116	1.1	8.6	3.3
40.8	33.2	2.9	8.7	18.6

Table 4.6: A comparison of the ISA-AMS measured values and the nominal value of the PRIME Lab set of four standards. The measured results were calibrated to the nominal value of the highest ratio PRIME Lab standard. The ISA-AMS data represents an average of two targets. The standard deviation of the mean and statistical error based on the number of counts are included.

the 40.8 x 10^{-14} standard. This is likely due to the lower count rate; the statistical error, calculated from Equation 4.4, is over double that of the other standards.

While these results are promising, many Cl samples will have ^{36}Cl/Cl ratios much lower than those examined by these standards. A dashed line on Figure 4.10 indicates the region that was of interest for further study using standards. In addition to this missing region, the PRIME Lab standards that were acquired over a decade prior to these tests, had not been stored in a dry and dark environment, and had been transferred from the University of Toronto. The standards were sticky and difficult to work with. To test that these factors had not impacted the results and to extend into the lower ratio region, a calibration curve using the NIST SRM 4943 standard set was produced, detailed in Section 4.8.2.

4.8.2 NIST SRM 4943

A dilution series of seven samples were prepared using the NIST SRM 4943 NaCl standard. Details of their preparation and the ^{36}Cl/Cl ratios calculated based on dilutions can be found in Appendix A. This dilution series was sent to ETH for measurement. Details of these results are found in Section 4.1.0.1. The lowest ratio sample, measured as 3 x 10^{-15} by ETH, is a Pugwash salt sample from the Windsor Salt Mine provided by Dr. John Gosse [90]. Pugwash is used as the ^{36}Cl blank in our measurement.

The weighted average of four targets of each sample was used to determine the calibration curve in Figure 4.11. For quality assurance, one target of the 4.16 x 10^{-11} and one target of the 1.20 x 10^{-12} PRIME Lab standards were included in the run. The error bars are equal to the standard deviation of the mean calculated using Equation 4.5. The solid line shows the points at which the ISA measured values are equal to the values measured by ETH.

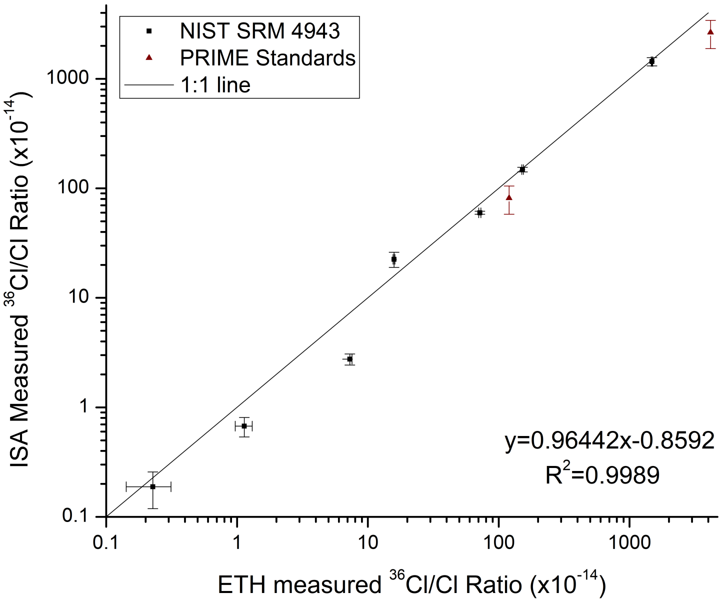

Figure 4.11: A comparison of the ISA-AMS measured values and the ETH measured values of the NIST SRM 4943 dilution series. The measured results were calibrated to the ETH measured value of the highest ratio sample in the NIST SRM 4943 dilution series. Each point represents an average of four targets. The error bars are the standard deviation of the mean. One target each of two PRIME Lab standards were included in the run for quality insurance. The solid line represents the 1:1 agreement between the ETH and ISA-AMS values.

Comparing the percent difference between the ETH and ISA measurements, found in Table 4.7, to those found in Section 4.8.1 shows similar results for ^{36}Cl/Cl ratios in the 4 x 10^{-13} to 10^{-11} region. The statistical error and standard deviation between the two standard sets are comparable. However, only two targets were measured by ISA-AMS for the PRIME standards and four targets were used in this measurement. Ratios below the PRIME Lab reference standards range begin to show larger statistical errors, standard deviations, and percent differences between the externally measured results and the ISA results.

The percent difference between the ETH-measured and ISA-measured samples remains low for the 7 x 10^{-13} and higher. However, for the lower ratio standards, the percent

ETH Measured ^{36}Cl/Cl Ratio (x10^{-14})	Statistical Error (%)	Standard Deviation (%)	ISA-AMS Measured ^{36}Cl/Cl Ratio (x10^{-14})	Statistical Error (%)	Standard Deviation (%)	Percent Difference (%)
1484.1	1.3	1.3	1436	0.4	8.5	3.2
152.1	2.0	1.4	148	1.3	4.7	2.6
71.8	2.6	1.9	60	1.9	3.3	16.4
15.9	5.0	1.7	23	3.1	17.4	44.7
7.3	5.8	3.9	2.8	5.5	10.7	61.6
1.2	16.3	14.5	0.67	10.8	14.9	44.2
0.3	36.6	33.3	0.19	16.0	36.8	36.7

Table 4.7: A comparison of the ISA-AMS measured values and the ETH measured values of the NIST SRM 4943 dilution series. The measured results were calibrated to the ETH measured value of the highest ratio sample in the NIST SRM 4943 dilution series. The ISA-AMS data represents an average of four targets. The ETH data represents the average of one or two targets. The standard deviation of the mean and statistical error based on the number of counts are included for both data sets. The ISA-AMS statistical error is calculated based on the number of counts for all targets of that sample.

difference rises to 44% or higher. In this region, the counting statistical error is slightly higher for the ETH-measured values than the ISA-measured values. However, these errors were achieved with just one or two targets at ETH but used four targets with ISA-AMS. The standard deviation is also comparable between the two for very low ratio standards, in the 10^{-15} to 10^{-14} region. In the 5 x 10^{-13} to 5 x 10^{-14} region, ETH maintains a much lower standard deviation than ISA-AMS. This difference may be a result of poorer separation between the ^{36}S and ^{36}Cl in the GIC of the AEL-AMS 3 MV system.

The accelerator had been idle for a month prior to this accelerator run, resulting in an increase in accelerator driver failures that may cause slight variations to the optimization of the beamline. These events may have increased the error in the results. Due to the measuring technique currently being used, only the ^{36}Cl would be affected by fluctuations in the HE end of the 3 MV system and therefore the calibration factor cannot correct these.

4.9 NO$_2$ pressure comparison

The presence of S in the spectrum, shown in Figure 4.12a), lead to a test to compare the accuracy of results using 11 μbar of He and two pressures of NO$_2$, 10.8 μbar or 13.5 μbar.

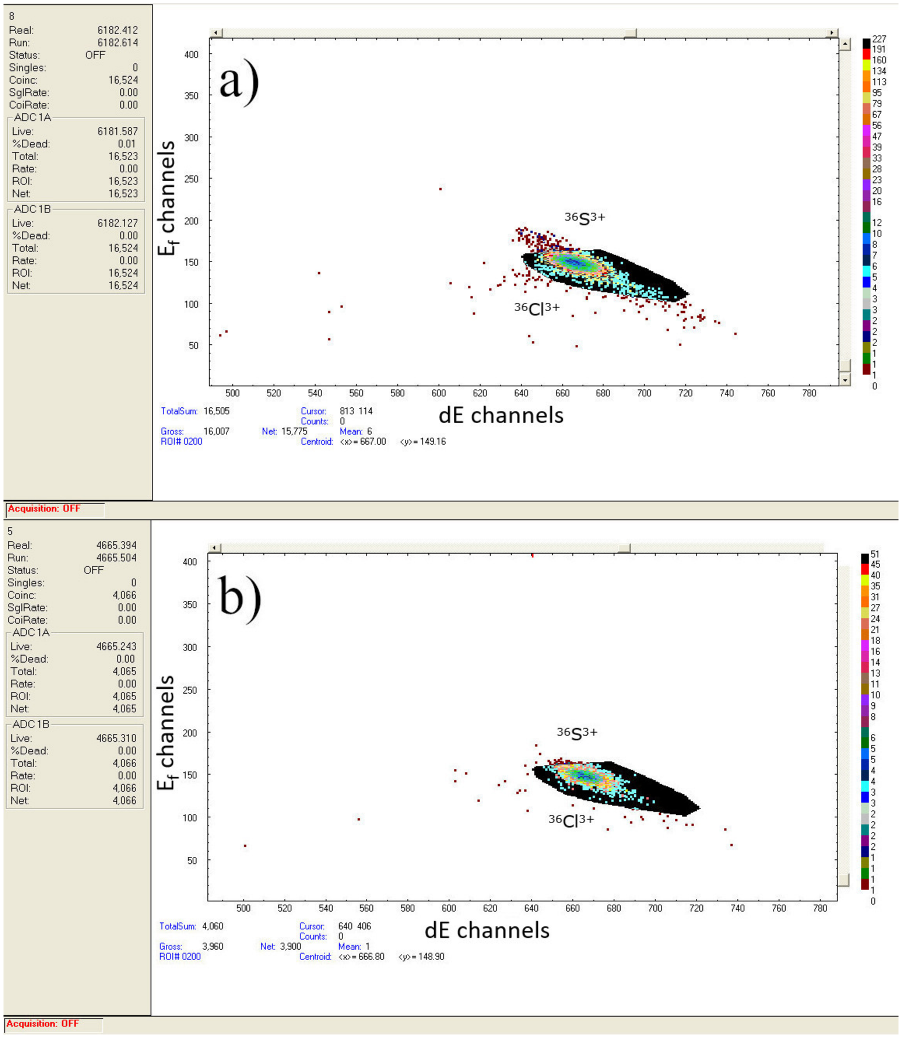

```
8
Real:        6182.412
Run:         6182.614
Status:      OFF
Singles:     0
Coinc:       16,524
SglRate:     0.00
CoiRate:     0.00
ADC 1A
Live:        6181.587
%Dead:       0.01
Total:       16,523
Rate:        0.00
ROI:         16,523
Net:         16,523
ADC 1B
Live:        6182.127
%Dead:       0.00
Total:       16,524
Rate:        0.00
ROI:         16,524
Net:         16,524

TotalSum:  16,505                  Cursor:    813  114
                                   Counts:    0
Gross:     16,007      Net: 15,775 Mean:  6
ROI# 0200                          Centroid:  <x>= 667.00   <y>= 149.16

Acquisition: OFF
```

```
5
Real:        4665.394
Run:         4665.504
Status:      OFF
Singles:     0
Coinc:       4,066
SglRate:     0.00
CoiRate:     0.00
ADC 1A
Live:        4665.243
%Dead:       0.00
Total:       4,065
Rate:        0.00
ROI:         4,065
Net:         4,065
ADC 1B
Live:        4665.310
%Dead:       0.00
Total:       4,066
Rate:        0.00
ROI:         4,066
Net:         4,066

TotalSum:  4,060                   Cursor:    640  406
                                   Counts:    0
Gross:     3,960       Net: 3,900  Mean:  1
ROI# 0200                          Centroid:  <x>= 666.80   <y>= 148.90

Acquisition: OFF
```

Figure 4.12: Spectra from a 1.5 x 10^{-11} ^{36}Cl/Cl ratio NIST dilution series sample. a) uses 10.8 μbar NO_2 in the ISA, b) uses 13.5 μbar NO_2. The decrease in sulfur (counts on top of the ROI) is visible but measurement time of the a) is 6182 s compared to 4665 s for b).

Previous measurements have been completed using 10.8 μbar NO_2. The increase in NO_2 will result in less sulfur contaminating the spectrum but will also reduce the ^{36}Cl counts. The sulfur suppression curve, Figure 3.11, showed an order of magnitude reduction in sulfur going from 10.8 μbar to 13.5 μbar. In the same NO_2 adjustment, chlorine was reduced by 20%. After 13.5 μbar NO_2, a plateau in sulfur suppression was observed, so it is not useful to increase the NO_2 beyond this point.

In this test, increasing the NO_2 reduced the sulfur count rate, calculated from (Total counts - gross counts)/livetime. For example, in Figure 4.12 the sulfur count rates for the 1.5 x 10^{-11} ^{36}Cl/Cl ratio standards went from 0.081 cps to 0.021 cps. Figure 4.12a) uses

ETH Measured ^{36}Cl/Cl Ratio (x10^{-14})	Count Rate (cps) for 10.8 μbar (4 SCCM) NO_2	Count Rate (cps) for 13.5 μbar (5 SCCM) NO_2
1484.1	1.8058	0.8500
152.1	0.1744	0.0885
71.8	0.1077	0.0543
15.9	0.0351	0.0204
7.3	0.0172	0.0064
1.2	0.0035	0.0011
0.3	0.0009	0.0004

Table 4.8: A comparison of ^{36}Cl/Cl ratios of NIST SRM 4943 dilution series measured at ETH and by AMS-ISA. The latter measurements used 11 μbar of He and either 10.8 μbar or 13.5 μbar NO_2.

10.8 μbar NO_2 and had a ^{36}Cl count rate of 2.59 cps. Figure 4.12b) uses 13.5 μbar NO_2 and had a ^{36}Cl count rate of 0.085 cps. The ^{36}Cl counts are those that fall in the black ROI, such that the count rate is the gross counts/livetime. The sulfur counts fall just above this region.

Table 4.8 shows that the increase in NO_2 also reduced the ^{36}Cl count rate of every standard by approximately half. This resulted in an increased error for many of the final measured ratios, as seen in Figure 4.13. Figure 4.13 compares the final ^{36}Cl/Cl ratios using 11 μbar of He and 10.8 μbar or 13.5 μbar NO_2. Similar measurement times were used on each sample. These are also compared to the measurements completed by ETH.

When comparing to the error in ETH, the error when using 13.5 μbar NO_2 is now 5-23 times greater. This is not the case for the blank, which only has an error of 3.7% (compared to 37.5% at ETH). The individual errors on the blank are 75 and 150% but happen to have good agreement in the ratio and therefore a small standard deviation of the mean. Overall, the 10.8 μbar NO_2 produced results closer to the accepted value and had smaller associated errors, as seen in Figure 4.13. Therefore, an increase in the chlorine transmission appears necessary for the use of 13.5 μbar NO_2 and for sufficient sulfur suppression. This may be possible with Configuration 4 and will be tested in the future.

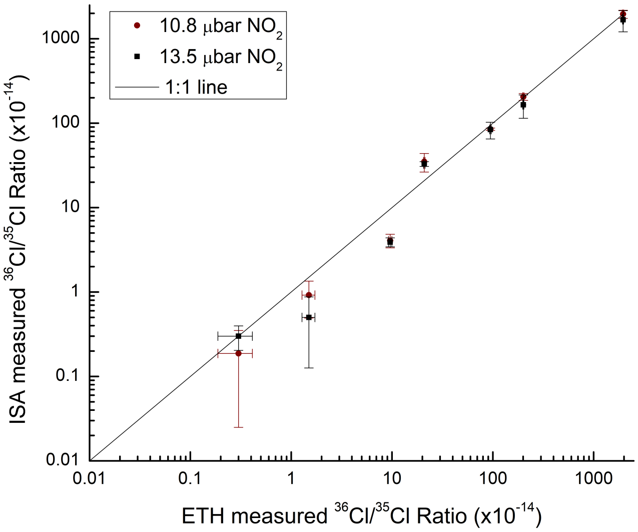

Figure 4.13: A comparison of ^{36}Cl/Cl ratios of NIST SRM 4943 using 11 μ bar of He and either 10.8 μbar or 13.5 μbar NO_2 for the NIST SRM 4943 dilution series. They are compared to the ETH measured ratios.

4.10 Measurement stability

The stability of the measurements are of particular importance to the measurement of ^{36}Cl on the AEL-AMS 3 MV system because the rare and stable beams are not treated in the same way. Therefore, fluctuations that occur after the Faraday cups at the ISA entrance will only affect the ^{36}Cl and cannot be accounted for with calibration to a reference material.

The accelerator run of the PRIME Lab ^{36}Cl/Cl ratio standards can be used to test the stability of the measurements technique. Figure 4.14 shows the raw data ratios for two targets each of the three highest ratio PRIME Lab standards listed in Table 4.1.

Each data point corresponds to the average ^{36}Cl/^{35}Cl ratio of one 30 second measurement block. The measurement order and blocks measured are listed in Table 4.9. For each target, the lowest ratio was measured first for 225 30 second blocks. The targets were then cycled through for a second set of 225 30 second blocks. This means that each target was measured for 3 hours and 45 minutes and the total accelerator run time was approximately 39 hours.

Good agreement for the entire measurement time can be seen for the three standards

Measurement order	Nominal ^{36}Cl/Cl ratio (Target number)	Number of measurement blocks	Length of measurement blocks (s)
1	AgCl Blank (1)	225	30
2	$4.08\text{x}10^{-13}$ (1)	225	30
3	$1.20\text{x}10^{-12}$ (1)	225	30
4	$4.42\text{x}10^{-12}$ (1)	225	30
5	$4.16\text{x}10^{-11}$ (1)	225	30
6	AgCl Blank (2)	225	30
7	$4.08\text{x}10^{-13}$ (2)	225	30
8	$1.20\text{x}10^{-12}$ (2)	225	30
9	$4.42\text{x}10^{-12}$ (2)	225	30
10	$4.16\text{x}10^{-11}$ (2)	225	30
11	AgCl Blank (1)	225	30
12	$4.08\text{x}10^{-13}$ (1)	225	30
13	$1.20\text{x}10^{-12}$ (1)	225	30
14	$4.42\text{x}10^{-12}$ (1)	225	30
15	$4.16\text{x}10^{-11}$ (1)	225	30
16	AgCl Blank (2)	225	30
17	$4.08\text{x}10^{-13}$ (2)	225	30
18	$1.20\text{x}10^{-12}$ (2)	225	30
19	$4.42\text{x}10^{-12}$ (2)	225	30
20	$4.16\text{x}10^{-11}$ (2)	225	30

Table 4.9: Stability check measurement order of the PRIME Lab standard targets. The block time and time per block is included for each target.

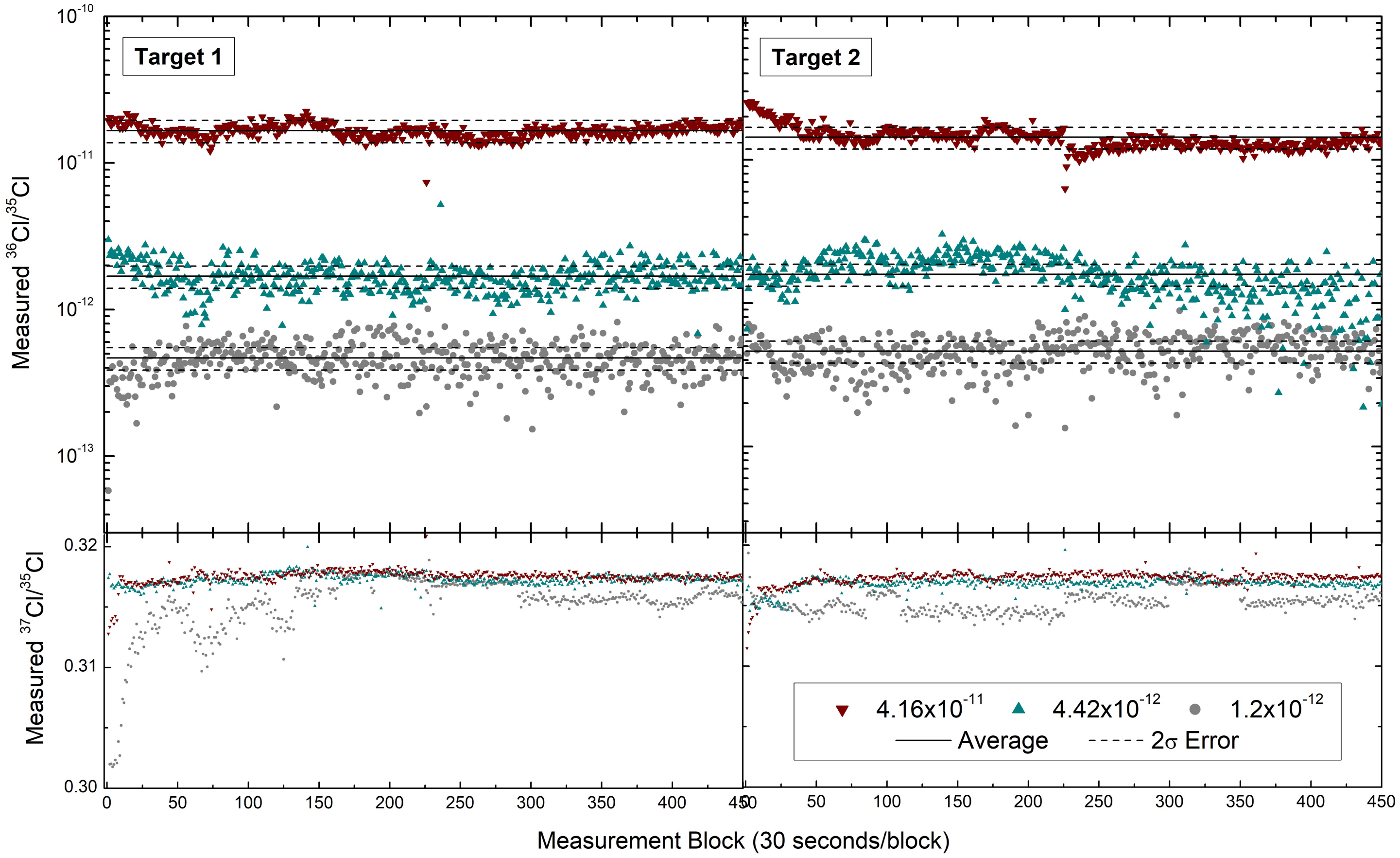

Figure 4.14: The raw data ^{36}Cl/^{35}Cl and ^{37}Cl/^{35}Cl ratios for two targets each of the three highest ratio PRIME Lab standards. Each data point corresponds to the average ratio of one 30 second measurement block. The average ratio is shown as a solid line. The 2σ of the mean of the two targets is shown as a dashed line.

included in Figure 4.14. The percent difference between the average measured ^{36}Cl/^{35}Cl ratios of the two targets for the 1.20 x 10^{-12} PRIME Lab standard is 0.3%, 11% for the 4.42 x 10^{-12} standard, and 15% for the 4.16 x 10^{-11} standard. The low count rate of the 4.08 x 10^{-13} PRIME Lab standard increases the scatter of the ^{36}Cl/^{35}Cl ratios and does not appear highly stable. It is not included in Figure 4.14 because it makes the higher ratio standards difficult to see. Despite this, the 4.08 x 10^{-13} standard only had a 0.9% difference between the two targets.

An increase in instability can be seen in the ^{36}Cl/^{35}Cl ratio of the last 225 measurement blocks of target 2 of the 4.16 x 10^{-11} standard. This was the last set of measurements and is likely a result of a drift in components along the beamline. This implies that additional

Measurement Laboratory	Number of targets	^{36}Cl/Cl Ratio (x10^{-14})	Standard Deviation (%)	Limit of Detection (x10^{-14})	Limit of Quantification (x10^{-14})
ISA-AMS	13	0.21	21	0.34	0.65
ETH	5	0.12	35	0.24	0.51
CAMS	5	0.19	6	0.22	0.30

Table 4.10: ^{36}Cl/Cl ratios of an AgCl blank found by ISA-AMS, ETH, and CAMS. The number of targets, standard deviation, LOD and LOQ are included for each laboratory.

tuning may be necessary after approximately 28 hours.

The stable ^{37}Cl/^{35}Cl ratio of 0.32 [43] can be monitored in the LE end of the beamline, prior to injection into the ISA. Outliers can be removed from the data set prior to data reduction and calibration to a standard. The scatter in ^{37}Cl/^{35}Cl ratio seen in the first 20 measurement blocks of Figure 4.14 indicate that large fluctuations in current occur on a fresh target. To account for this, an initial pass of 10 measurement blocks is completed on each target. These data points are removed prior to data reduction.

4.11 Blank level

At the time of writing, 13 targets of the Pugwash blank have been measured using ISA-AMS. Five targets of Pugwash blank have also been measured at both ETH and Center for Accelerator Mass Spectrometry, Lawrence Livermore National Laboratory (CAMS-LLNL). Table 4.10 provides the ^{36}Cl/Cl ratio found at all three AMS laboratories and the corresponding standard deviation. The average blank level determined by ISA-AMS is a ^{36}Cl/Cl ratio of (2.1 ± 0.4)x 10^{-15}. Within error, this agrees with the blank ratio measured at ETH and CAMS-LLNL.

The limit of detection (LOD) can be calculated using the equation:

$$\text{LOD} = \overline{R}_{blank} + 3 * \sigma_{blank} \tag{4.6}$$

where $\overline{R}_{blank}$ is the ^{36}Cl/Cl ratio weighted average for the blank and σ_{blank} is the standard deviation of the mean of the blank. Similarly, the limit of quantification (LOQ) can be calculated using the equation:

$$\mathrm{LOQ} = \overline{R}_{blank} + 10 * \sigma_{blank} \tag{4.7}$$

The LOD and LOQ based on the measurement of the Pugwash blank are presented in Table 4.10. Both ETH and CAMS-LLNL also measured their in house AgCl blank material at similar ^{36}Cl/Cl ratios. ISA-AMS has the highest ratio LOD and LOQ despite having more measured targets.

The individual ^{36}Cl/Cl ratios for each of the 13 Pugwash targets measured are shown in Figure 4.15. As more runs are completed, a more accurate blank ^{36}Cl/Cl ratio can be determined. The weighted average of the targets, the LOD, and the LOQ are indicated by solid lines. The average falls within error of all targets measured, with two exceptions.

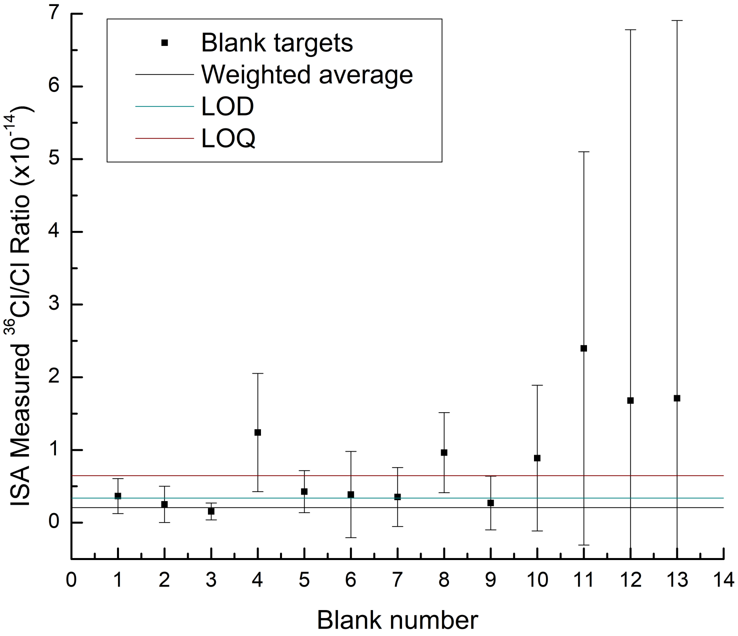

Figure 4.15: The individual ^{36}Cl/Cl ratios for each of the 13 Pugwash targets measured by ISA-AMS. The weighted average of the targets (black), the LOD (blue), and the LOQ (red) are indicated by solid lines.

The large error bars on the blank numbers 11, 12, and 13 are likely due to the addition of groundwater samples to the ISA-AMS run, discussed further in Chapter 5. Blanks 1 to 10 were only run with other standards, that had much lower levels of S than the groundwater samples. An increase in S was seen in the spectra of the standards run with groundwater samples compared to those run with no samples present in the target wheel. In the detector, there is a region of overlap between the ^{36}S and ^{36}Cl, where the two cannot be distinguished. Additional ^{36}S from cross contamination may increase the ^{36}Cl/Cl ratio and its associated error in those 3 targets.

4.12 Conclusion

Multiple tests were implemented to determine the best data acquisition technique to measure the ^{36}Cl/Cl ratio using ISA-AMS. The residence time in the ISA and the transmission dependence on injected current meant the techniques that injected the stable beam current were not viable. Therefore, FSI with only mass 36 injected into the ISA and ^{35}Cl and ^{37}Cl measured in LE off-axis Faraday cups was selected. The ILIAMS has demonstrated a similar decrease in transmission with incoming current of hundreds of nA but employs the use of a beam attenuator to limit the incoming current [92]. Future work will include the addition of a beam attenuator on the Research Line to allow injection of a reduced current stable beam into the ISA.

Using a set of ^{36}Cl reference standards and a dilution series, it was determined that linear calibration results could be obtained for a ^{36}Cl/Cl ratio ranging from 10^{-11} to 10^{-15}. The measurements were stable over more than 24 hours of continuous measurement. A blank level of 2.1 x 10^{-15} was observed.

The increased transmission with the ISA Configuration 4 may allow for a higher NO_2 pressure, reducing the ^{36}S in the spectrum and therefore the measurement error. Future work should remeasure the standards and blanks with this configuration.

With confirmation of calibration linearity over a range of ^{36}Cl/Cl ratio and an established measurement and data reduction technique, the ISA could be applied to the measurement of samples with unknown ^{36}Cl/Cl ratios.

Chapter 5

Application of ISA-AMS to measurement of ^{36}Cl in water samples

The confirmation that ^{36}Cl standards and dilution series samples follow a linear calibration curve, using Configuration 3 and the measurement method selected, means that ISA-AMS can be tested for measurement on unknown samples. The measurement of ^{36}Cl in water samples, particularly groundwaters, is a common application of ^{36}Cl AMS. ISA-AMS was applied to the measurement of a variety of water samples and the resulting ^{36}Cl/Cl ratios were compared to the results determined by AMS measurements at ETH and CAMS-LLNL on the same material. The effects of chemical sulfur removal on the accuracy of the results were also studied.

5.1 Chlorine in water samples

Dr. Guang Yang and Dr. John Gosse of Cosmic Ray Isotope Sciences at Dalhousie Lab (CRISDal) provided tap water, ^{35}Cl carrier, and Pugwash samples listed in Table 5.1. The samples had unknown ^{36}Cl/Cl ratios to test the capabilities of ISA-AMS. All samples were provided as AgCl and mixed with Nb at AEL-AMS. Half of the tap water and Pugwash samples underwent chemical S removal at CRISDal. They were redissolved from AgCl and purified of S using $BaNO_3$ [95]. Purification with $BaNO_3$ was completed five times prior to the reprecipitation of AgCl. The ^{35}Cl carrier and Pugwash samples were expected to have low to blank levels of ^{36}Cl. The tap water samples were expected to have ^{36}Cl/Cl ratios in the 10^{-13} to 10^{-14} range.

Sample ID	Source	Sulfur Removal
5423	50 ml tap water	5 days S removal
5424	50 ml tap water	5 days S removal
5425	50 ml tap water	5 days S removal
5426	50 ml tap water	5 days S removal
5427	50 ml tap water	No S removal
5428	50 ml tap water	No S removal
5429	50 ml tap water	No S removal
5430	50 ml tap water	No S removal
5431	^{35}Cl carrier only*	No S removal
5432	^{35}Cl carrier only*	No S removal
5433	^{35}Cl carrier only*	No S removal
5434	^{35}Cl carrier only*	No S removal
5435	^{35}Cl carrier only*	No S removal
5436	^{35}Cl carrier only*	No S removal
5437	^{35}Cl carrier only*	No S removal
5438	^{35}Cl carrier only*	No S removal
5439	10 ml tap water	5 days S removal
5440	10 ml tap water	5 days S removal
5441	10 ml tap water	5 days S removal
5442	10 ml tap water	5 days S removal
5443	10 ml tap water	No S removal
5444	10 ml tap water	No S removal
5445	10 ml tap water	No S removal
5446	10 ml tap water	No S removal
5447	Pugwash	5 days S removal
5448	Pugwash	5 days S removal
5449	Pugwash	5 days S removal
5450	Pugwash	5 days S removal
5451	Pugwash	No S removal
5452	Pugwash	No S removal
5453	Pugwash	No S removal
5454	Pugwash	No S removal

Table 5.1: Tap water, ^{35}Cl carrier, and Pugwash samples prepared and provided by Dr. Guang Yang and Dr. John Gosse of CRISDal. The samples that underwent chemical removal of sulfur are indicated. *Supplier: Oak Ridge National Laboratories.

An additional 63 environmental samples were provided from an external supplier to compare an ISA-AMS run of unknown samples with a run of the same samples by a lab with a larger accelerator (ETH or CAMS-LLNL). These groundwater, porewater, and drillwater samples are listed in Table 5.2 along with an identification number and the Cl concentration in each sample. The concentrations were sufficient to provide enough sample material to run on ISA-AMS and at one of the alternative AMS laboratories.

When collecting the groundwater samples, exposure to air was minimized to avoid atmospheric contaminates [96]. Core materials were crushed and leached to obtain the porewater samples. The groundwater and porewater are expected to have low ^{36}Cl/Cl ratios, having reached the secular equilibirium discussed in Section 1.3.2. Five drilling water samples and two water samples are also included, with ^{36}Cl/Cl ratios expected to be slightly higher for these samples.

The samples in Table 5.2 were provided as solutes. These solutes were precipitated into AgCl using the method described in Appendix B. Chemical removal of S was not completed on these samples using $BaNO_3$. However, they were passed through resin-filled columns (Dowex 1x8 100-200 mesh ion-exchange) for purification.

The samples were mixed with Nb at a ratio of 1:3 AgCl to Nb by volume. Approximately 5 mg of the AgCl-Nb mixture is pressed into a copper target using a 3 ton pneumatic press. When enough sample material was available two targets of each sample were prepared. In cases were less material was available, only one target was analyzed (Samples 5423 and 5441).

5.2 Measurement method of samples

Based on the results discussed in Section 4.2, the samples were run with ^{35}Cl and ^{37}Cl measured in the LE off-axis Faraday cups. Only the rare radioisotope, ^{36}Cl, was injected into the ISA and was then measured in the GIC using FSI. The approximate accelerator and ISA settings used are listed in Appendix C and the tuning procedure is detailed in Section 4.3. The gas pressure used in the ISA were 10.8 μbar of NO_2 and 11 μbar of He.

Due to various preparation times for these samples, two accelerator runs were completed.

Sample ID	Source	Cl (ppm)
001	Groundwater	4700
002	Groundwater	4600
003	Groundwater	3900
004	Groundwater	3900
005	Groundwater	4000
006	Groundwater	8200
007	Groundwater	5100
008	Groundwater	9600
009	Groundwater	9700
010	Groundwater	13000
011	Groundwater	15000
012	Groundwater	14000
013	Groundwater	14000
014	Groundwater	1400
015	Groundwater	1400
016	Groundwater	1600
017	Groundwater	1600
018	Groundwater	3200
019	Groundwater	2900
020	Groundwater	6900
021	Porewater	2133
022	Porewater	614
023	Porewater	3180
024	Porewater	3554
025	Porewater	4282
026	Porewater	3740
027	Porewater	4538
028	Porewater	2140
029	Porewater	1025
030	Porewater	2046
031	Porewater	2719
032	Porewater	735
033	Porewater	1710
034	Porewater	847
035	Porewater	5406
036	Porewater	5495
037	Porewater	2908
038	Porewater	719
039	Porewater	413
040	Porewater	662
041	Porewater	1538
042	Porewater	1217
043	Porewater	5883
044	Porewater	2527
045	Porewater	1024
046	Porewater	1330
047	Porewater	2632
048	Porewater	1237
049	Porewater	1127
050	Porewater	854
051	Porewater	822
052	Porewater	753
053	Porewater	883
054	Porewater	1224
055	Porewater	2222
056	Drill water	69
057	Drill water	90000
058	Drill water	58000
059	Drill water	71000
060	Drill water	88000
061	Water sample	130
062	Water sample	130
063	Pugwash solution	2000

Table 5.2: Groundwater, porewater, and drillwater samples for ^{36}Cl/Cl measurement by ISA-AMS. The samples were also measured externally by ETH or CAMS-LLNL. The Cl concentration in the samples was provided. All sample had sufficient Cl to not require addition of a carrier.

The first run included samples 1-13 and 57-60, while the second included all other samples. The runs included targets made from the NIST SRM 4943 dilution series material. The same measurement method was used for both accelerator runs. The approximate ratios of the dilution series used are 1 x 10^{-11} for tuning, 1 x 10^{-12}, 1 x 10^{-13}, and 5 x 10^{-14} or 1 x 10^{-14}, depending on the run. The external measurement of the dilution series is discussed in Section 4.1.0.1 and Section 4.8.2. All resulting ^{36}Cl/Cl ratios for the samples were calibrated to one of these dilution series targets with a known ^{36}Cl/Cl ratio. The dilution series targets were measured first, passing from highest to the lowest ^{36}Cl/Cl ratio. After this dilution series, a Pugwash target was used as a process blank. A machine blank of pure Nb was run after the process blank. The lack of ^{36}Cl in both the process blank and machine blank allow time for burn off of residual memory between the higher ^{36}Cl/Cl ratio dilution series targets and the unknown water sample targets. The water samples of Table 5.2 were run next, as they were expected to have low ^{36}Cl/Cl ratios.

The original plan was to include the samples of Table 5.2, followed by those in Table 5.1 in a single accelerator run. However, during this run, frequent issues with the rotation of the target wheel were seen, resulting from the weight of approximately 200 copper targets in the target wheel. To alleviate the strain on the target wheel, the accelerator run was split into two parts and the Table 5.1 samples were run after the water samples of Table 5.2.

A new set of dilution series targets (1 x 10^{-12}, 1 x 10^{-13}, and 1 x 10^{-14}) was prepared for the Table 5.1 accelerator run. As with the water sample run, the dilution series targets, from highest to lowest ^{36}Cl/Cl ratios, a Pugwash process blank, and a Nb machine blank were run first. The samples in Table 5.1 were separated based on expected S content in the targets. The ^{35}Cl carrier and Pugwash are blanks that should contain low S counts, regardless of undergoing chemical S removal. The tap water samples that did not undergo chemical S removal (5427-5430 and 5451-5454) were expected to produce higher S count rates in the GIC and were kept as the last samples in the sequence.

In both accelerator runs, an initial pass of five 30 second measurement blocks was completed on all of the targets. This data is not included in the final analysis. Each following pass used fifty 30 second measurement blocks. At least three passes were completed on each target. This resulted in approximately 75 minutes of measurement on each target.

5.3 Effect of chemical removal of S on ISA-AMS

Two targets of each tap water and Pugwash sample in Table 5.1 were tested, except Sample IDs 5423 and 5441, which only had enough material for one target each. However, the results of all samples of the same material would be expected to have similar ^{36}Cl/Cl ratios. The raw ^{36}Cl/Cl ratios were calibrated with the 1 x 10^{-13} dilution series sample to determine the actual ratios.

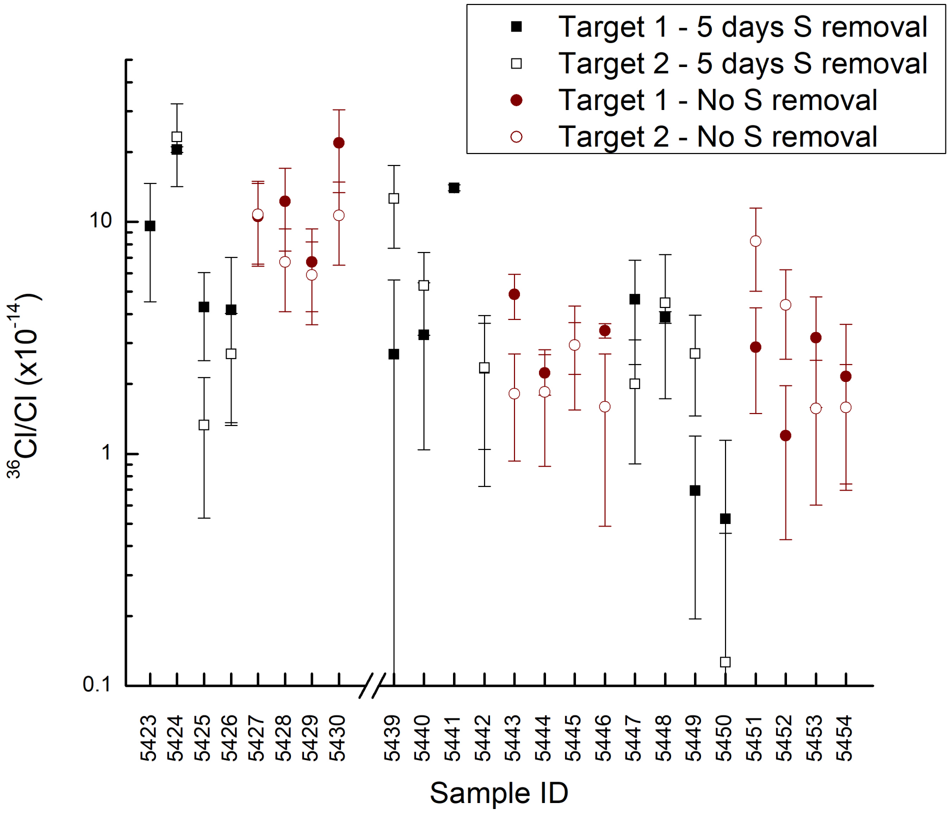

Figure 5.1: A comparison of the ^{36}Cl/Cl ratio results of ISA-AMS on multiple targets of the same sample material. The black squares are targets with 5 days of chemical S removal. The red circles are targets without chemical S removal. Two targets of most material were prepared (shown as a filled and unfilled symbol). Each set of 8 samples (i.e. 5423-5430, 5439-5446, 5447-5454) are the same sample material.

The resulting ^{36}Cl/Cl ratios of an ISA-AMS run on these samples can be seen in Figure 5.1. It is presented on a logarithmic scale to compare the water samples with the blanks, which have ^{36}Cl/Cl ratios which differ by an order of magnitude. The black squares are targets with 5 days of chemical S removal. The S removal process is discussed in Section 5.1. The red circles are targets without chemical S removal. When two targets are available, the first target measured is shown with a filled symbol and the second is an unfilled symbol. The same material is shown as a set of eight sample IDs. Therefore, samples 5423 to 5430 (50 ml tap water) should result in similar ^{36}Cl/Cl ratios as each other; the same is true for samples 5439 to 5446 (10 ml tap water) or 5447 to 5454 (Pugwash).

Figure 5.1 shows that the ^{36}Cl/Cl ratio of two targets of the same sample ID typically agree within error. For the Pugwash samples (5439-5446) and the 10 ml tap water without S removal (5443-5446) there is also agreement between all sample IDs measured. However, there are much larger fluctuations between measured ^{36}Cl/Cl ratio for the 50 ml tap water sample (5423-5430) and the 10 ml samples that underwent chemical S removal (5439-5442). This variability may be a result of the chemical S removal process itself. Undergoing any chemical process may affect the Cl yield. The water targets were separated prior to the chemical S removal and therefore, may have had different final yields of Cl. Each target underwent 5 instances of precipitation of S as $BaSO_4$, each of which may have altered the Cl in the target.

The ISA-AMS average ^{36}Cl/Cl ratio results and their standard deviation are presented in Table 5.3, along with the average count rate of all targets of that material. The weighted average is calculated using Equation 4.3 and the standard deviation is calculated using Equation 4.5. The count rate was determined by the total counts for each sample type over the measurement time of all the targets for that sample type. Table 5.3 compares the average ^{36}Cl/Cl ratio and the count rate of the samples with 5 days of chemical S removal and the samples with no sulfur removal. This may indicate if removal of S from the AgCl material, through precipitation of S as $BaSO_4$ using $BaNO_3$, is necessary to obtain accurate results with ISA-AMS.

The ^{36}Cl/Cl ratios between the 50 ml tap water samples with or without chemical S removal are in agreement within error. They are also close to the 1 x 10^{-13} ratio expected of tap water. However, the errors in the samples with S removal are high. This may be due to differences in the ^{36}Cl/Cl ratio between the four samples grouped in this average. The two

	50 ml tap water		**10 ml tap water**		**Pugwash**	
Sulfur Removal	Average ^{36}Cl/Cl ratio (x10^{-14})	Average count rate	Average ^{36}Cl/Cl ratio (x10^{-14})	Average count rate	Average ^{36}Cl/Cl ratio (x10^{-14})	Average count rate
5 days S removal	11 ± 6	0.183	9 ± 3	0.113	1 ± 1	0.097
No S removal	9 ± 1	0.227	2.3 ± 0.2	0.103	1.7 ± 0.1	0.113

Table 5.3: A comparison of the weighted average ^{36}Cl/Cl ratio and counte rate of all targets of 50 ml tap water, 10 ml tap water, and Pugwash with or without chemical S removal. The count rate was calculated using gross counts/livetime.

targets of 5424 consistently measured higher ratios (approximately 2 x 10^{-13}) than the other targets of this sample. The difference between the 10 ml tap water with or without S removal is much larger. This could be due to differences in the tap water samples, especially 5439. The ^{36}Cl/Cl ratio of the Pugwash sample are in good agreement but are approximately an order of magnitude higher than expected for a blank material. This is discussed in more detail in Section 5.4.4.

Comparing the average count rate of the 5 days of S removal to no S removal being completed shows no significant difference between the two. This may indicate that there is no additional S being detected in the ROI of the GIC and therefore chemical removal of S may not be necessary for ISA-AMS measurements. The discrepancy between count rate and ^{36}Cl/Cl ratio (the lower ^{36}Cl/Cl ratio has a higher count rate) is due to the measurement of some of these samples during a different accelerator run and therefore being calibrated by differing amounts.

5.4 Groundwater and porewater results

ISA-AMS was used to measure the ^{36}Cl/Cl ratios of the groundwater, porewater, and drill water samples of Table 5.2. The analysis of these types of samples is a common application of ^{36}Cl measurement using AMS. Analysis of these samples and comparison to measurement of the same samples by external laboratories uncovered sources of error not observed in the analysis of the standards (Chapter 4). These include the S content in the spectra of the water samples, and a higher ^{36}Cl/Cl ratio for blanks.

5.4.1 Sulfur content in samples

The S content in the water samples appeared significantly higher than previously seen in the standards and dilution series, regardless of chemical removal of the S. This increased ^{36}S required a cutout in the ROI of the GIC, shown in Figure 5.2. Figure 5.2a) shows the spectrum of a 1.5 x 10−11 NIST SRM 4943 dilution series target. The ^{36}S content in the sample appears to not overlap with the ^{36}Cl peak. Figure 5.2b) is a spectrum for water sample 12 with a similar count time. In this case, a large ^{36}S tail can be seen in the ROI for ^{36}Cl. The approximate count rate for ^{36}S in Figure 5.2a) is 0.12 cps, while in Figure 5.2b) the ^{36}S count rate is much higher at 0.21 cps. This approximate count rate is calculated using (total counts - gross counts)/livetime. It may be an underestimate due to some ^{36}S falling within the ROI and therefore being counted in the gross counts.

The ^{36}S count rate for the dilution series in this measurement (Figure 5.2) is even larger than in accelerator runs that only included standards and dilution series targets, with much lower S content. This can be compared to Figure 4.13a) where the ^{36}S count rate was only 0.08 cps for the same dilution series material. This indicates that the higher S content in the water samples in this run is contaminating the standards in the same target wheel. This could be due to memory effects in the ion source or due to residual S in the ISA. To decrease the S content in all of these samples, the NO_2 pressure in the ISA may need to be increased. Alternatively, while tests for chemical S removal did not indicate that S removal was necessarily, it may still be required for higher S samples, such as groundwaters.

5.4.2 Comparison of calibration standards

In each accelerator run, two sets of NIST SRM 4943 dilution series targets were included for calibration of the raw ^{36}Cl/Cl ratios. In both cases, the blank level was much higher than in the calibration curve found in Chapter 4. The average raw ratios of the dilution series for the 10^{-14} targets and the 10^{-15} targets were the same, so no distinction could be found between the two target materials. Typically, these values differ by a factor of approximately 10. Similarly, there was also only a factor of 4 (or less) difference between the dilution series

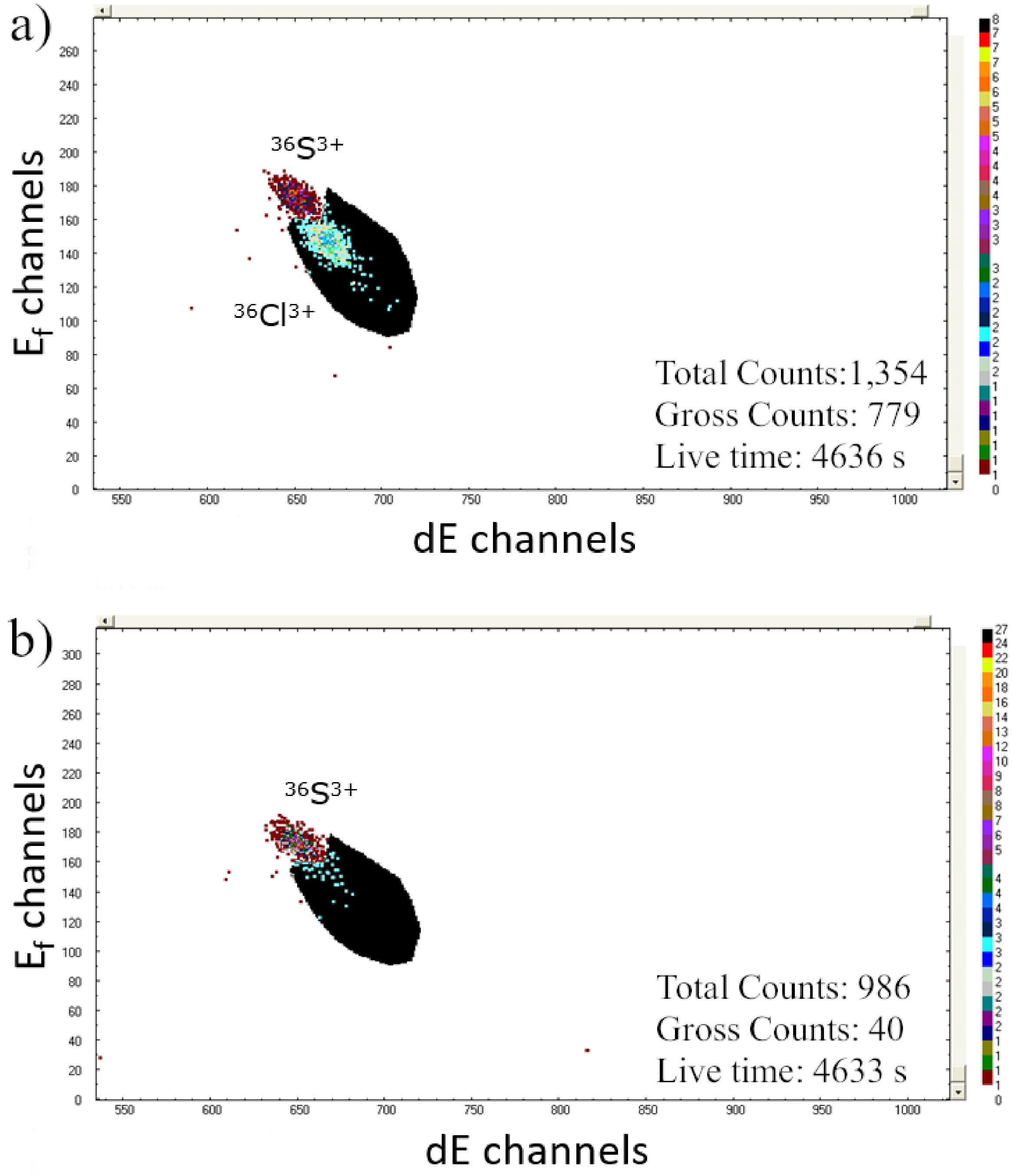

Figure 5.2: The spectra in the GIC of a) a 1 x 10−11 NIST SRM 4943 dilution series and b) Water sample 12. The ROI was selected using a ^{36}Cl standard. The ^{36}S count rate in a) is approximately 0.12 cps and in b) is approximately 0.21 cps. This is calculated using (total counts - gross counts)/livetime. The water sample 12 appears to have a larger S tail entering into the ROI than the dilution series.

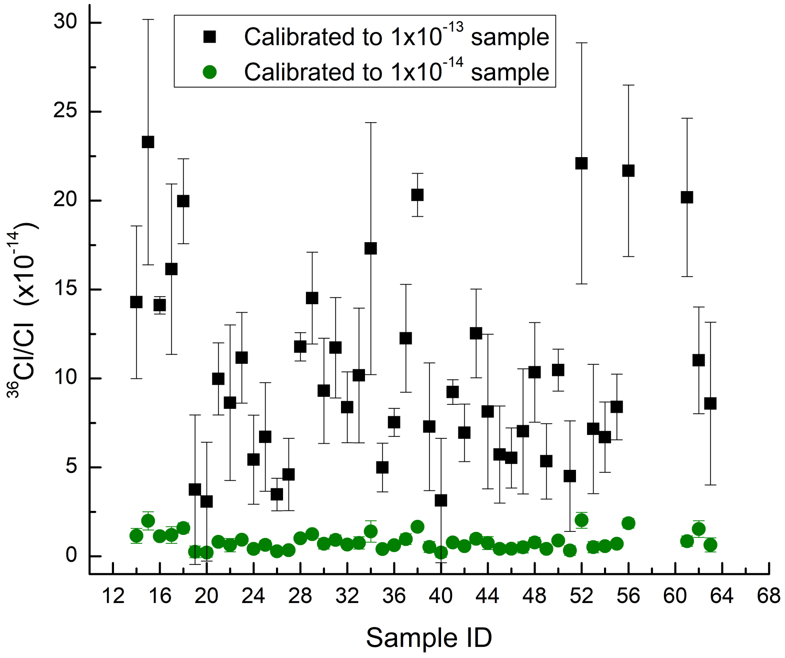

Figure 5.3: A comparison of ^{36}Cl/Cl ratios for water samples 14-57 and 60-63 using different standards for calibration. The ^{36}Cl/Cl ratio of the black squares were calibrated to the 1.59 x 10^{-13} NIST SRM 4943 dilution series targets. The green circles were calibrated to the 1.2 x 10^{-14} NIST SRM 4943 dilution series targets. The disagreement between the results indicates that the blank level was higher than expected and that the samples had low count rates.

10^{-13} targets and the 10^{-14} targets.

The effect of this increased blank level can be seen in Figure 5.3. Figure 5.3 shows a comparison in the ISA-AMS ^{36}Cl/Cl ratios for water samples 14-57 and 60-63 using two different NIST SRM 4943 dilution series targets to determine the calibration factor. The ^{36}Cl/Cl ratio of the black squares were calibrated to the 1.59 x 10^{-13} NIST SRM 4943 dilution series targets. The green circles were calibrated to the 1.2 x 10^{-14} NIST SRM 4943 dilution series targets.

If the blank level was lower, the values should not be dependent on which ratio is used to determine the calibration factor. The ^{36}Cl/Cl ratios for the two calibration methods, shown in Figure 5.3, have a difference of up to an order of magnitude. This disagreement is likely a result of the count rate at low ratios and the high S content found in the sample spectra, discussed in Section 5.4.1.

In Section 5.4.3 either the 1.2 x 10^{-14} or 7.3 x 10^{-14} targets were selected to determine the calibration factor. The selection was based on the lowest available ^{36}Cl/Cl ratio dilution series target. These dilution series targets were selected over the others included in the accelerator run due to their proximity to the ratios determined by the external laboratories.

5.4.3 Comparison to external measurements

The groundwater, porewater, and drill water samples were prepared at different times, following the same procedure outlined in Appendix B. Due to the various timing of preparation, the samples have been analyzed by two different external laboratories, ETH or CAMS-LLNL. The samples measured at ETH and the samples measured at CAMS-LLNL were also included in different accelerator runs using ISA-AMS.

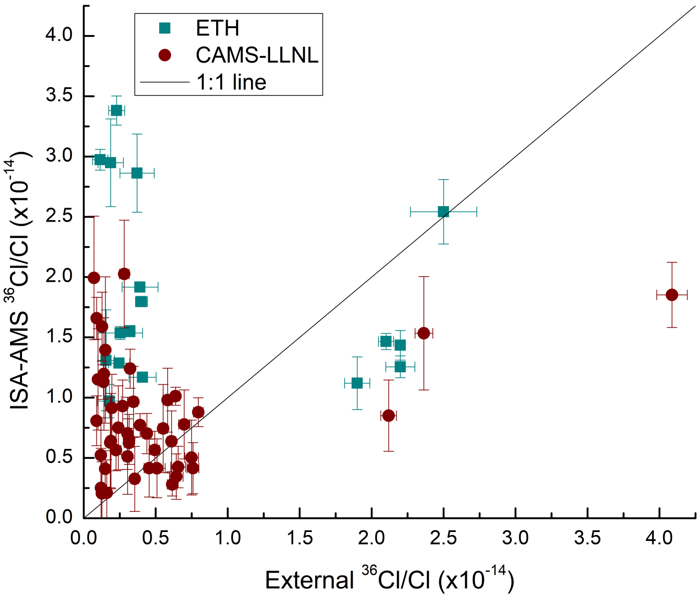

Figure 5.4: A comparison of the ISA-AMS measured and externally measured ^{36}Cl/Cl ratios of the samples in Table 5.2. The blue squares were measured by ETH. The red circles were measured by CAMS-LLNL. The error bars are the standard deviation of the mean. The solid line represents the 1:1 agreement between the externally measured and the ISA-AMS values.

The ^{36}Cl/Cl ratio results of the samples listed in Table 5.2 are shown in Figure 5.4. The x-axis is the ^{36}Cl/Cl ratio measured by an external laboratory. The blue squares were measured by ETH and the red circles were measured by CAMS-LLNL. Most ETH results also used two targets. The CAMS-LLNL results used one target for each result.

The y-axis is the ^{36}Cl/Cl ratio measured by ISA-AMS. The ^{36}Cl/Cl ratio of samples compared to the ETH results were calibrated to the 7.3 x 10^{-14} NIST SRM 4943 dilution series. The ^{36}Cl/Cl ratio of samples compared to the CAMS-LLNL results were calibrated to the 1.2 x 10^{-14} NIST SRM 4943 dilution series. The ISA-AMS values are the result of the weighted average of two targets. The error bars are the standard deviation of the mean. The solid line represents the 1:1 agreement between the externally measured and the ISA-AMS values.

Many of the ISA-AMS measured ^{36}Cl/Cl ratios in Figure 5.4 differ from the ^{36}Cl/Cl ratios measured externally. The ISA-AMS measured values are higher than the external measurements for the lower ratios (lower than 1 x 10^{-15}). In contrast, the ISA-AMS measured ^{36}Cl/Cl ratios for samples at higher ratios (in the 2 x 10^{-14} region) are lower than the external measurements. Samples in between these two regions appear to agree well. This may be indicative of ion source cross contamination, commonly found in ^{36}Cl measurements [97], or sources of ^{36}S cross contamination.

5.4.4 Blank measurements with water samples

The issues described in Section 5.4.1 and Section 5.4.2 resulted in a higher blank level, LOD, and LOQ in the accelerator runs that included water samples compared to those of Chapter 4, that only measured standards and dilution series targets with low S content. The blank levels, LODs, and LOQs for both set of accelerator runs are included in Table 5.4. The ^{35}Cl carrier targets of Table 5.1 and the Pugwash targets were separated into two blank types.

Table 5.4 shows that with a similar number of targets, the ^{36}Cl/Cl ratio of the Pugwash target and its associated standard deviation are both approximately doubled when measured with the water samples. Based on Equation 4.6 and Equation 4.7 are also approximately

Blank Sample	Number of targets	Average ^{36}Cl/Cl Ratio (x10^{-14})	Error (x10^{-14})	LOD (x10^{-14})	LOQ (x10^{-14})
Pugwash with standards	13	0.21	0.04	0.3	0.7
Pugwash with samples	14	0.4	0.1	0.7	1.5
^{35}Cl carrier with samples	16	0.38	0.09	0.65	1.3

Table 5.4: ^{36}Cl/Cl ratios of an AgCl blank found by 3 MV ISA-AMS with the blank included in an accelerator run with only ^{36}Cl standards or with water samples. The number of targets, standard deviation (error), LOD, and LOQ are included.

doubled for the measurements with water samples included. Many of the individual Pugwash targets in these runs had a ratio an order of magnitude higher than the expected 2.5 x 10^{-15}. The ^{35}Cl carrier targets had comparable blank levels, LODs, and LOQs to the Pugwash also run with water samples.

Figure 5.4 shows that most of the externally measured ^{36}Cl/Cl ratios for the water samples are below the LOD, 0.7 x 10^{-14}, of these ISA-AMS measurements.

5.5 Conclusion

There are often large differences between the ISA-AMS ^{36}Cl/Cl ratios for the water samples and the ratios measured externally by ETH or CAMS-LLNL. However, comparing the ^{36}Cl/Cl ratios to the blank targets, the LOD, and the LOQ, all methods are in agreement that the samples are at or near blank level ^{36}Cl.

During routine measurement of ^{36}Cl, the ^{36}Cl/Cl ratio of the water samples would be unknown and external measurements could not be used to help determine which dilution series target to use to determine the calibration factor. Therefore, the high S content in the water samples that leads to the high blank level results for dilution series targets needs to be addressed in future work.

The chemical removal of S did not appear to solve the issues seen in the water sample measurements. However, this work was completed using Configuration 3 of the ISA. The improved transmission of Configuration 4, may allow for an increase in NO_2 gas pressure used during routine ^{36}Cl measurement, without a decrease in the count rate. This may lead to lower ^{36}S counts in the GIC spectra of water samples.

Chapter 6

Concluding Remarks

6.1 Summary

The ISA is an RFQ reaction cell system that has been combined with a 3 MV AMS system to provide selective isobar suppression prior to injection of an ion beam into an accelerator. Small to medium-sized accelerators, like the 3 MV tandem accelerator of AEL-AMS, are unable to separate the isobars of many isotopes. The possible isotopes of study can be increased using the ISA, as shown by previous work on the prototype device [36, 84, 39].

The ISA has been integrated into a second injection line, the Research Line, of the 3 MV AEL-AMS system. This line begins with a Cs^+ sputter ion source, which produces a negative ion beam in the 20 keV-35 keV energy range. The beam is then energy analyzed, using an ESA and momentum analyzed, using an injection magnet. This momentum-analyzed beam is injected into the ISA, where the beam is decelerated from keV to eV energies.

These low energy ions are confined by the RFQ and maintain a controlled velocity through the cell due to DC offset voltages placed on the RFQ segments. The low energy ions are further decelerated through collisional cooling with a non-reactive gas. The cell is filled with a second gas, selected to have energetically favourable charge change reactions with the interfering isobar, while allowing the isotope of interest to pass through unreacted.

After removal of the interfering isobar, the isotope of interest is reaccelerated before it is injected into the 3 MV tandem accelerator. The resulting positive ion beam is analyzed for momentum and energy in the high energy end of the AMS system before the rare radioisotope is counted in the GIC.

Multiple configurations of the ISA were tested to optimize the transmission of the isotope of interest, using ^{36}Cl as a benchmark isotope. The majority of the work presented here was completed using 'Configuration 3', which consisted of a single open RFQ segment before a 6 mm entrance aperture plate to a joint cooling and reaction cell. The cooling and reaction cell was filled with two gases and consists of eleven RFQ segments. A 13 mm aperture plate is present between the sixth and seventh RFQ segment of the cooling and reaction cell. Finally, there is a 4 mm exit aperture plate before one final open RFQ segment. SIMION 8.1 ion optics simulations were completed to optimize work in the deceleration region of Configuration 3.

The transmission for Cl anions was optimized experimentally based on cooling gas type and pressure. This led to the selection of He gas for cooling, at pressures of approximately 13.7 μbar for best transmission with only a cooling gas. At this He pressure 50% transmission was achieved. Based on past work, NO_2 was selected as a reaction gas for the suppression of S anions. The pressure of the cooling and reaction gases selected for routine measurements were 11 μbar He and 10.8 μbar NO_2. The He pressure was decreased to achieve best transmission in the mixture of the two gases. This provided over 7 orders of magnitude suppression of S anions but reduced transmission of Cl anions to only 30%. Optimized settings of the deck voltage on the ISA and of the Mathieu q_2 parameter were also determined using the transmission of Cl anions.

Later studies were completed on a new configuration, 'Configuration 4'. This configuration added an additional 6 mm aperture plate immediately after the deceleration cone, at the beginning of the first RFQ segment. The addition of this aperture will change the field seen by the decelerating anions. It will block the effects of the RF field on the deceleration cone field, which may completely negate the potential at some times, based on the time-dependent voltage. It will also block the attractive field of the cone after the ions enter the first RFQ segment. This improved transmission of Cl anions by 2x or greater (80% transmission in He and 60% transmission in a mixture of He and NO_2).

Configuration 3 of the ISA was tested using ^{36}Cl/Cl reference standards and an in-house made dilution series from the NIST SRM 4943 ^{36}Cl reference material. These standards were used to develop a method of measuring ^{36}Cl using ISA-AMS. It was determined that a space charge limit of 300 nA existed for the ISA and therefore, the unattenuated stable ^{35}Cl or ^{37}Cl beams could not be injected into the ISA. To avoid injecting the stable beams, it was determined that the currents would be measured in Faraday cups in the low energy system. This was only possible due to the injection magnet and off-axis Faraday cups at the entrance of the ISA, and the high stability of the HVEE accelerator system. The use of a calibration factor to determine the final ^{36}Cl/Cl ratio avoids most issues with the method, except if instability is seen in the accelerator or high energy system. These instabilities would only affect the rare ^{36}Cl counts.

A tuning procedure, measurement routine, and data reduction method were determined for ^{36}Cl. The transmission through the AMS system was characterized and a charge state of 3+ was selected with the accelerator at 3 MV. This provided partial dE/dx separation of ^{36}Cl and its abundant isobar ^{36}S in the GIC.

Two calibration curves, one using four PRIME ^{36}Cl standards ranging in ^{36}Cl/Cl ratio from 10^{-11} to 10^{-13} and one using the six dilution series materials ranging from 10^{-11} to 10^{-15}, were shown to have linear results. The measurements remained stable for over 24 hours. The ^{36}Cl blank materials had ^{36}Cl/Cl ratios of 2 x 10^{-15}. The LOD was a ^{36}Cl/Cl ratio of 3 x 10^{-15} and the LOQ was 7 x 10^{-15}.

Finally, ISA-AMS has been applied to measuring ^{36}Cl/Cl of water samples from environmental applications. These included groundwaters and porewaters and were expected to have low ^{36}Cl/Cl ratios. The increased ^{36}S in these samples compared to the standards and dilution series materials was apparent in the GIC spectra. Memory effects in either the source or the ISA increased the ^{36}S present in the diluton series target spectra and the blank materials included in the run along with the samples. This resulted in a higher blank level than previously observed. Further reduction in S will need to be completed before ISA-AMS can be reliably applied to environmental samples.

6.2 Outlook and future development

There are many opportunities for future research and development with the ISA, both for the benchmark isotope ^{36}Cl and for various other isotopes with abundant isobars. The first area of study that should be explored is the use of Configuration 4. A better understanding of the increased Cl transmission with this configuration could be achieved using SIMION 8.1 simulations of the deceleration region of both this configuration and Configuration 3.

The high S content seen in the water samples will need to be reduced to apply ISA-AMS to environmental samples. ISA-AMS still needs improved counting rates to reach good agreement with external laboratories for low ratio measurements. Larger AMS facilities (5-10 MV) analyzing ^{36}Cl have reported discrepancies in the measurement of ^{36}Cl/Cl of standards in the 10^{-11} to 10^{-13} range of up to 17% between facilities [56]. The most likely cause of these discrepancies are the use of in-house materials in place of standards for calibration of unknown results. If these materials have not been intercalibrated, they could produce systematic measurement errors. Additionally, incomplete background correction due to the presence of ^{36}S or from cross contamination of ^{36}Cl from higher ratio samples in the source could cause some of these discrepancies.

The increased transmission achieved in Configuration 4 may also allow for a higher NO_2 pressure inside the cooling and reaction cell. The higher NO_2 pressure should decrease the ^{36}S seen in the GIC spectra for ^{36}Cl. In Configuration 3, an increase in NO_2 pressure was shown to decrease the count rate of ^{36}Cl. The decrease in count rate meant that the corresponding decrease in ^{36}S did not result in improved measurement error. However, with double the ^{36}Cl counts, the count rate may still be sufficient at the higher NO_2 pressure. Configuration 4 should then be tested on ^{36}Cl standards, blanks, and water samples.

A plateau was observed in the suppression of ^{36}S with increased NO_2 pressure. A study of the reaction products leaving the ISA using a detector system placed after the 45° magnet could clarify if reverse reactions are present in the reaction cell. It could also be of interest to examine other reaction gases. F_2 and BF_3 have electron affinities of 3.00 eV and 2.65 eV [80], respectively. These are likely to have electron transfer reactions with S anions but not with Cl anions. However, both gases require many safety precautions to use.

Additionally, the separation between $^{36}S^{3+}$ and $^{36}Cl^{3+}$ in the GIC may be improved by altering the isobutane pressure. Studies of stripper gas pressure may improve the charge state yield. Both tests may improve the count rate achievable for ISA-AMS.

Finally, a method for attenuating the stable beam prior to injection into the ISA should be established. Mesh attenuators often degrade rapidly and with spatial variability when exposed to high current beams. Options such as a beam chopper are being explored.

The ISA has shown promising results for the measurement of ^{36}Cl with blank levels, LODs, and LOQs comparable to other laboratories when measured without additional sources of S contamination. Future work should improve these values and further reduce S interferences found in the ^{36}Cl spectra of ISA-AMS. The ISA should also be applied to the measurement of other isotopes and could greatly expand the isotopes available for analysis by the 3 MV system at AEL-AMS.

Bibliography

[1] W. Kutschera. Accelerator mass spectrometry: state of the art and perspectives. *Adv. Phys.*, 1:570–595, 2016.

[2] A. E. Litherland, X-L. Zhao, and W. E. Kieser. Mass spectrometry with accelerators. *Mass Spectrom. Rev.*, 30:1037–1072, 2010.

[3] K.H. Purser, R.B. Liebert, A.E. Litherland, R.P. Beukens, H.E. Gove, C.L. Bennett, M.R. Clover, and W.E. Sondheim. An attempt to detect stable N^- ions from a sputter ion source and some implications of the results for the design of tandems for ultra-sensitive carbon analysis. *Rev. Phys. appl.*, 12:1487–1492, 1977.

[4] D. E. Nelson, R. G. Kortelin, and W. R. Stott. Radiocarbon dating using electrostatic accelerators: Negative ions provide the key. *Science*, 198:507–508, 1977.

[5] C. L. Bennett, R. P. Beukens, M. R. Clover, H. E. Gove, R. B. Liebert, A. E. Litherland, K. H. Purser, and W. E. Sondheim. Radiocarbon dating using electrostatic accelerators: Negative ions provide the key. *Science*, 198:508–510, 1977.

[6] W. Kutschera. Applications of accelerator mass spectrometry. *Int. J. Mass. Spectrom.*, 349-350:203–218, 2013.

[7] R. Hellborg and G. Skog. Accelerator Mass Spectrometry. *Mass Spectrom. Rev.*, 27:398–427, 2008.

[8] W. Kutschera. Progress in isotope analysis at ultra-trace level by AMS. *Int. J. Mass. Spectrom.*, 242:145–160, 2005.

[9] W. Kutschera. An overview of world-wide AMS facilities. *Nucl. Instr. Meth. B.*, 538:87–94, 2023.

[10] M. Stocker, R. Bertschinger, M. Döbeli, M. Grajcar, S. Jacob, J. Scheer, M. Suter, and H.-A. Synal. Status of the PSI/ETH compact AMS facility. *Nucl. Instr. Meth. B*, 223-224:104–108, 2004.

[11] A. E. Litherland. Fundamentals of accelerator mass spectrometry. *Phil. Trans. R. Soc. Lond. A*, 323:5–21, 1987.

[12] M-J. Nadeau, M. A. Garwan, X-L. Zhao, and A. E. Litherland. A negative ion survey; towards the completion of the periodic table of the negative ions. *Nucl. Instr. Meth. B*, 123:521–526, 1997.

[13] G.M. Raisbeck, F. Yiou, D. Bourles, J. Lestringuez, and D. Deboffle. Measurement of ^{10}Be with a tandetron accelerator operating at 2 MV. *Nucl. Instr. Meth. B*, 5:175–178, 1984.

[14] M. Klepper. Bound-state beta decay and nuclear lifetime measurements at the storage-cooler ring ESR. *Nucl. Phys. A*, 626:199–213, 1997.

[15] M. Paul. Separation of isobars with a gas-filled magnet. *Nucl. Instr. Meth. B*, 52:315–321, 1990.

[16] O. Forstner, P. Andersson, D. Hanstorp, J. Lahner, M. Martschini, J. Pitters, A. Priller, P. Steier, and R. Golser. The ILIAS project for selective isobar suppression by laser photodetachment. *Nucl. Instr. Meth. B*, 361:217–221, 2015.

[17] M. Martschini, J. Lachner, K. Hain, M. Kern, O. Marchhart, J. Pitters, A. Priller, P. Steier, A. Wiederin, A. Wieser, and R. Golser. 5 years of ion-laser interaction mass spectrometry - status and prospects of isobar suppression in AMS by lasers. *Radiocarbon*, 64:555–568, 2021.

[18] M. Honda, M. Martschini, O. Marchhart, A.Priller, P. Steier, R. Golser, T. K. Sato, T. Kazuaki, and A. Sakaguch. Novel ^{90}Sr analysis of environmental samples by Ion-Laser InterAction Mass Spectrometry. *Anal. Methods*, 14:2732–2738, 2022.

[19] M. Martschini, J. Lachner, S. Merchel, A. Priller, P. Steier, A. Wallner, A. Wieser, and R. Golser. The quest for AMS of ^{182}Hf^{-} why poor gas gives pure beams. *EPJ Web Conf.*, 232:02003, 2020.

[20] M. Schiffer, O. Machhart, A. Priller, S. Herb, G. Hackenberg, S. Heinze, M. Martschini, E. Strub, T. Dunai, R. Golser, and A. Dewald. An advanced radio-frequency quadrupole ion cooler for accelerator mass spectrometry. *Nucl. Instr. Meth. B*, 528:27–33, 2022.

[21] H-A. Synal. New ion-optical devices utilizing oscillatory electric fields. I. Principle of operation and analytical theory of multipole devices with two-dimensional electric fields. *Int. J. Mass Spectrom.*, 73:197–235, 1985.

[22] D. J. Douglas and N. V. Konenkov. Influence of the 6th and 10th spatial harmonics on the peak shape of a quadrupole mass filter with round rods. *Rapid Commun. Mass Spectrom.*, 16:1425–1431, 2002.

[23] D. J. Douglas, A. J. Frank, and D. Mao. Linear ion traps in mass spectrometry. *Mass Spectrom. Rev.*, 24:1–29, 2004.

[24] S. D. Tanner, V. I. Baranov, and D. R. Bandura. Reaction cells and collision cells for ICP-MS: a tutorial review. *Acta Part B At. Spectrosc.*, 57:1361–1452, 2002.

[25] P. H. Dawson. Quadrupole mass analyzers: Performance, design and some recent applications. *Mass Spectrom. Rev.*, 5:1–37, 1986.

[26] W. Paul and H. Steinwedel. Notizen: Ein neues Massenspektrometer ohne Magnetfeld. *Z. Naturforsch. A*, 8:448–450, 1953.

[27] D. J. Douglas. Some current perspectives on ICP-MS. *Can. J. Appl. Spectrosc.*, 34:38–49, 1989.

[28] J. T. Rowan and R. S. Houk. Attenuation of polyatomic ion interferences in Inductively Coupled Plasma Mass Spectrometry by gas-phase collisions. *Appl. Spectrosc.*, 43:976–980, 1989.

[29] D. J. Douglas. Mechanism of the collision-induced dissociation of polyatomic ions studied by triple quadrupole mass spectrometry. *J. Phys. Chem.*, 86:185–191, 1982.

[30] Y. Liu, J.F. Liang, and J.R. Beene. A high efficiency RF quadrupole ion beam cooler for negative ions. *Nucl. Instr. Meth. B*, 255:416–422, 2007.

[31] Y. Liu, C. C. Havener, T. L. Lewis, A. Galindo-Uribarri, and J. R. Beene. Purification of Radioactive Ion Beams by Photodetachment in a RF Quadrupole Ion Beam Cooler. *AIP Conf. Proc.*, 1097:431–442, 2009.

[32] D. B. Dunkin, F. C. Fehsenfeld, and E. E. Ferguson. Thermal energy rate constants for the reactions ${NO_2}^- + Cl_2 \rightarrow Cl_2^- + NO_2$, ${Cl_2}^- + NO_2 \rightarrow Cl^- + NO_2Cl$, $SH^- + NO_2 \rightarrow {NO_2}^- + SH$, $SH^- + Cl_2 \rightarrow {Cl_2}^- + SH$, and $S^- + NO_2 \rightarrow {NO_2}^- + S$. *Chem. Phys. Lett.*, 15:257–259, 1972.

[33] J. P. Doupé, A. E. Litherland, I. Tomski, and X.-L. Zhao. Isobar separation at low energy in accelerator mass spectrometry. *Nucl. Instr. Meth. B*, 223-224:323–327, 2004.

[34] W. E. Kieser, X. L. Zhao, A. E. Litherland, J. A. Eliades, and R. J. Cornett. RFQ Reaction Cells for AMS: Developments and Applications. *EPJ Web Conf.*, 63:03005, 2013.

[35] A. E. Litherland, I. Tomski, X-L. Zhao, L. M. Cousins, J. P. Doupé, G. Javahery, and W. E. Kieser. Isobar separation at very low energy for AMS. *Nucl. Instr. Meth. B*, 259:230–235, 2007.

[36] J. Eliades, X-L. Zhao, W. E. Kieser, and A. E. Litherland. Isobar Attenuation Using Anion–Gas Reactions for Accelerator Mass Spectrometry and Application to ^{36}Cl. *Geostand. Geoanal. Res.*, 34:107–115, 2010.

[37] W. E. Kieser, J. A. Eliades, A. E. Litherland, X. L. Zhao, L. M. Cousins, and S. J. Ye. The low-energy Isobar Separator for Anions: Progress Report. *Radiocarbon*, 52:236–242, 2010.

[38] J. Eliades, A. E. Litherland, W. E. Kieser, L. M. Cousins, S. J. Ye, and X-L. Zhao. Cl/S isobar separation using an on-line reaction cell for ^{36}Cl measurement at low energies. *Nucl. Instr. Meth. B*, 268:839–842, 2010.

[39] J. Eliades, X-L. Zhao, A. E. Litherland, and W. E. Kieser. On-line ion chemistry for the AMS analysis of ^{90}Sr and ^{135,137}Cs. *Nucl. Instr. Meth. B*, 294:361–363, 2015.

[40] J-F. Alary, G. Javahery, W. E. Kieser, X-L. Zhao, A. E. Litherland, L. M. Cousins, and C. Charles. Isobar Separator for Anions: Current status. *Nucl. Instr. Meth. B*, 361:197–200, 2015.

[41] Laboratoire National Henri Becquerel. Atomic and nuclear data: ^{36}Cl - emissions and decay scheme, 2021. Last accessed June 2022.

[42] P.J. Linstrom and W.G. Mallard. *NIST Chemistry WebBook, NIST Standard Reference Database Number 69.* National Institute of Standards and Technology, 2022.

[43] K. J. R. Rosman and P. D. P. Taylor. Isotopic compositions of the elements 1997 (Technical Report). *Pure Appl. Chem.*, 70:217–235, 1998.

[44] T. Torgersen, M. A. Habermehl, F. M. Phillips, D. Elmore, P. Kubik, B. G. Jones, T. Hemmick, and H. E. Gove. Chlorine 36 Dating of Very Old Groundwater Further Studies in the Great Artesian Basin, Australia. *Water Resour. Res.*, 27:3201–3213, 1991.

[45] H. W. Bentley, F. M. Phillips, S. N. Davis, M. A. Habermehl, P. L. Airey, G. E. Calf, D. Elmore, H. E. Gove, and T. Torgersen. Chlorine 36 Dating of Very Old Groundwater 1. The Great Artesian Basin, Australia . *Water Resour. Res.*, 22:1991–2001, 1986.

[46] M. G. Zreda, F. M. Phillips, D. Elmore, P. W. Kubik, P. Sharma, and R. I. Dorn. Cosmogenic chlorine-36 production rates in terrestrial rocks. *Earth Planet. Sci. Lett.*, 105:94–109, 1991.

[47] I. Clark. *Groundwater Geochemistry and Isotopes.* CRC Press, Florida, United States of America, 2015.

[48] C. M. Lederer and V. S. Shirley. *Table of isotopes.* Wiley-Interscience, New York, 7th edition edition, 1978.

[49] D. Roman and P. L. Airey. The application of environmental chlorine-36 to hydrology - I. Liquid scintillation counting. *Int. J. Appl. Radiat. Isot.*, 32:287–290, 1981.

[50] M. Itoh, K. Watanabe, M. Hatakeyamab, and M. Tachibana. Determination of ^{36}Cl in biological shield concrete using pyrohydrolysis and liquid scintillation counting. *Analyst*, 127:964–966, 2002.

[51] R. Collé and J. W. L. Thomas. ^{36}Cl/Cl Accelerator-Mass-Spectrometry Standards: Verification of Their Serial-Dilution-Solution Preparations by Radioactivity Measurements. *J. Radioanal. Nucl. Chem.*, 98:653–677, 1993.

[52] D. Lariviere, V. F. Taylor, R. D. Evans, and R. J. Cornett. Radionuclide determination in environmental samples by inductively coupled plasma mass spectrometry. *Acta Part B At. Spectrosc.*, 61:877–904, 2006.

[53] J. Comte, C. Guy, A. L. Tornabene, M. Bertaux, S. Parraud, B. Pasquet, and P. Bienvenu. Radiochemical and SIMS measurement of ^{36}Cl in nuclear graphite: the issue of the measurement dispersion. *J. Res. Natl. Inst. Stand. Technol.*, 314:1245?1255, 2017.

[54] P. E. Warwick, B. C. Russell, I. W. Croudace, and Z. Zacharauskas. Evaluation of inductively coupled plasma tandem mass spectrometry for radionuclide assay in nuclear waste characterisation. *J. Anal. At. Spectrom.*, 34:1810–1821, 2019.

[55] D. Elmore, B. R. Fulton, M. R. Clover, J. R. Marsden, H. E. Gove, H. Naylor, K. H. Purser, L. R. Kilius, R. P. Beukens, and A. E. Litherland. Analysis of ^{36}Cl in environmental water samples using an electrostatic accelerator. *Nature*, 277:22–25, 1979.

[56] S. Merchel, W. Bremser, V. Alfimov, M. Arnold, G. Aumaître, L. Benedetti, D. L. Bourlès, M. Caffee, L. K. Fifield, R. C. Finkel, S. P. H. T. Freeman, M. Martschini, Y. Matsushi, D. H. Rood, K. Sasa, P. Steier, T. Takahashi, M. Tamari, S. G. Tims, Y. Tosaki, K. M. Wilcken, and S. Xu. Ultra-trace analysis of ^{36}Cl by accelerator mass spectrometry: an interlaboratory study. *Anal. Bioanal. Chem.*, 400:3125–3132, 2011.

[57] S. Merchel, R. Braucher, V. Alfimov, M. Bichler, D. L. Bourlès, and J. M. Reitner. The potential of historic rock avalanches and man-made structures as chlorine-36 production rate calibration sites. *Anal. Bioanal. Chem.*, 18:54–62, 2013.

[58] K. M. Wilcken, S. P. H. T. Freeman, A. Dougans, S. Xu, R. Loger, and C. Schnabel. Improved ^{36}Cl AMS at 5 MV. *Nucl. Instr. Meth. B*, 268:748–751, 2010.

[59] C. Vockenhuber, K.-U. Miltenberger, and H.-A. Synal. ^{36}Cl measurements with a gas-filled magnet at 6 MV. *Nucl. Instr. Meth. B*, 455:190–194, 2019.

[60] A. Galindo-Uribarri, J. R. Beene, M. Danchev, J. Doupé, B. Fuentes, J. Gomez del Campo, P. A. Hausladen, R. C. Juras, J. F. Liang, A. E. Litherland, Y. Liu, M. J. Meigs, G. D. Mills, P. E. Mueller, E. Padilla-Rodal, J. Pavan, J. W. Sinclair, and D. W. Stracener. Pushing the limits of accelerator mass spectrometry. *Nucl. Instr. Meth. B*, 259:123–130, 2007.

[61] M. Martschini, O. Forstner, R. Golser, W. Kutschera, S. Pavetich, A. Priller, P. Steier, M. Suter, and A. Wallner. Recent advances in AMS of ^{36}Cl with a 3-MV-tandem. *Nucl. Instr. Meth. B*, 269:3188–3191, 2011.

[62] L. K. Fifield, S. G. Tims, J. O. Stone, D. C. Argento, and M. De Cesare. Ultra-sensitive measurements of ^{36}Cl and ^{236}U at the Australian National University. *Nucl. Instr. Meth. B*, 294:126–131, 2013.

[63] J. Lachner, C. Marek, M. Martschini, A. Priller, P. Steier, and R. Golser. ^{36}Cl in a new light: AMS measurements assisted by ion-laser interaction. *Nucl. Instr. Meth. B*, 456:163–168, 2019.

[64] W. E. Kieser, X. L. Zhao, I. D. Clark, R. J. Cornett, A. E. Litherland, M. Klein, D. J. W. Mous, and J. F. Alary. The André E. Lalonde AMS Laboratory - The new accelerator mass spectrometry facility at the University of Ottawa. *Nucl. Instr. Meth. B*, 361:110–114, 2015.

[65] M. Klein and D. J. W. Mous. Technical improvements and performance of the HVE AMS sputter ion source SO-110. *Nucl. Instr. Meth. B*, 406:210–213, 2017.

[66] R. Middleton. A review of ion sources for accelerator mass spectrometry. *Nucl. Instr. Meth. B*, 5:193–199, 1984.

[67] M. Klein, J. Heinemeier, A. Gottdang, D. J. W. Mous, and J. Olsen. Extension of the HVE 1 MV multi-element AMS system for low background. *Nucl. Instr. Meth. B*, 331:204–208, 2014.

[68] J. Heinemeier, J. Olsen, M. Klein, and D. Mous. The new extended HVE 1 MV multi-element AMS system for low background installed at the Aarhus AMS Dating Centre. *Nucl. Instr. Meth. B*, 361:143–148, 2015.

[69] M. Klein, D. J. W. Mous, and A. Gottdang. Fast and accurate sequential injection AMS with gated Faraday cup current measurement. *Radiocarbon*, 46:77–82, 2004.

[70] W. E. Kieser, R. P. Beukens, L. R. Kilius, A. E. Litherland, M. J. Nadeau, and J. C. Rucklidge. Accelerator mass spectrometry at Toronto. *Nucl. Instr. Meth. B*, 24-25:667–671, 1987.

[71] X-L. Zhao. Comparison of single and double lenses for normal ams operations. Internal document, 2012.

[72] A. E. Litherland. Comparison of telescopic pair and a single einzel lens. Internal document, 2014.

[73] H-A. Synal. Developments in accelerator mass spectrometry. *Int. J. Mass Spectrom.*, 349-350:192–202, 2013.

[74] E. Ebrahimibasabi and S. A. H. Feghhi. Design and construction of a secondary electron suppressed Faraday Cup for measurement of beam current in an electrostatics proton accelerator. *Int. J. Mass Spectrom.*, 386:1–5, 2015.

[75] J. F. Ziegler, M. D. Ziegler, and J. P. Biersack. SRIM The stopping and range of ions in matter (2010). *Nucl. Instr. Meth. B*, 268:1818–1823, 2010.

[76] Germany FAST ComTec GmbH. MPA-NT multiparameter system software, 2023.

[77] D. A. Dahl. SIMION for the personal computer in reflection. *Int. J. Mass Spectrom.*, 200:3–25, 2000.

[78] X-L. Zhao and A. E. Litherland. A simulation study of linear RF ion guides for AMS. *Nucl. Instr. Meth. B*, 344:16–32, 2014.

[79] V. I. Baranov, D. R. Bandura, and S. D. Tanner. Limitations of the effective potential for the evaluation of the ion energy in the RF-driven quadrupole field. *Int. J. Mass Spectrom.*, 247:40–47, 2005.

[80] NIST Computational Chemistry Comparison and Benchmark Database. Nist standard reference database number 101, 2022. Last accessed March 2023. Editor: Russell D. Johnson III.

[81] E. L. Flannigan, J-F. Alary, W. E. Kieser, L. M. Cousins, and G. Javahery. Characterization of the isobar separator for anions integrated into the A. E. Lalonde laboratory's 3 MV AMS system. *Nucl. Instr. Meth. B*, 528:34–39, 2022.

[82] H. K. Roscoe and A. K. Hind. The equilibrium constant of NO_2 with N_2O_4 and the temperature dependence of the visible spectrum of NO_2: A critical review and the implications for measurements of NO_2 in the polar stratosphere. *J. Atmos. Chem.*, 16:257–276, 1993.

[83] P. Atkins and J. de Paula. *Physical Chemistry.* Oxford University Press, Great Britain, 8th edition edition, 2006.

[84] John Alexander Eliades. *A Radio Frequency Quadrupole Instrument for use with Accelerator Mass Spectrometry: Application to Low Kinetic Energy Reactive Isobar Suppression and Gas-Phase Anion Reaction Studies.* PhD thesis, University of Toronto, 2012.

[85] P. H. Dawson. *Quadrupole Mass Spectrometry and Its Applications.* Elsevier Scientific Publishing Company, New York, 1976.

[86] J. Eliades, X-L. Zhao, A. E. Litherland, and W. E. Kieser. Negative ion-gas reaction studies using ion guides and accelerator mass spectrometry II: S^-, SO^- and Cl^- with NO_2 and N_2O. *Nucl. Instr. Meth. B*, 361:300–306, 2015.

[87] National Institute of Standards and Technology. Material details: Srm 4943 - chlorine-36 radioactivity standard, 2021. Last accessed June 2022.

[88] M. Christl, C. Vockenhuber, P.W. Kubik, L. Wacker, J. Lachner, V. Alfimov, and H.-A. Synal. The ETH Zurich AMS facilities: Performance parameters and reference materials. *Nucl. Instr. Meth. B*, 294:29–38, 2013.

[89] P. Sharma, P. W. Kubik, U. Fehn, H. E. Gove, K. Nishiizumo, and D. Elmore. Development of ^{36}Cl standards for AMS. *Nucl. Instr. Meth. B*, 52:410–415, 1990.

[90] J. Gosse. Personal communications, 2021.

[91] H-A. Synal, J. Beer, G. Bonani, Ch. Lukasczyk, and M. Suter. $^{36}C1$ measurements at the Zürich AMS facility. *Nucl. Instr. Meth. B*, 92:79–84, 1994.

[92] M. Martschini, J. Pitters, T. Moreau, P. Andersson, O. Forstner, D. Hanstorp, J. Lachner, Y. Liu, A. Priller, P. Steier, and R. Golser. Selective laser photodetachment of intense atomic and molecular negative ion beams with the ILIAS RFQ ion beam cooler. *Int. J. Mass Spectrom.*, 415:9–17, 2017.

[93] R. Braucher, K. Keddadouche, G. Aumaître, D.L. Bourlès, M. Arnold, S. Pivot, M. Baroni, A. Scharf, G. Rugel, and E. Bard. Chlorine measurements at the 5MV French AMS national facility ASTER: Associated external uncertainties and comparability with the 6MV DREAMS facility. *Nucl. Instr. Meth. B*, 420:40–45, 2018.

[94] S. Akhmadaliev, R. Heller, D. Hanf, G. Rugel, and S. Merchel. The new 6 MV AMS-facility DREAMS at Dresden. *Nucl. Instr. Meth. B*, 294:5–10, 2013.

[95] S. M. Marrero, F. M. Phillips, M. W. Caffee, and J. C. Gosse. CRONUS-Earth cosmogenic ^{36}Cl calibration. *Quat. Geochronol.*, 31:199–219, 2016.

[96] I. Clark. Personal communications, 2023.

[97] S. Pavetich, S. Akhmadaliev, M. Arnold, G. Aumaître, D. Bourlès, J. Buchriegler, R. Golser, K. Keddadouche, M. Martschini, S. Merchel, G. Rugel, and P. Steier. Interlaboratory study of the ion source memory effect in ^{36}Cl accelerator mass spectrometry. *Nucl. Instr. Meth. B*, 329:22–29, 2014.

Appendix A

Preparation of ^{36}Cl standards

Standards with a range of ^{36}Cl/Cl ratios, at ratios similar to samples to be measured, are needed to provide a calibrationS curve using the ISA at the AEL-AMS Laboratory. These standards are also necessary to determine the calibration factor applied to future ^{36}Cl samples. A set of PRIME Lab standards with ^{36}Cl/Cl ratios of 4.16 x10^{-11}, 4.42 x10^{-12}, 1.20 x10^{-12} and 4.08 x10^{-13} were available as solid AgCl. However, these standards were not properly stored and exposure to light and moisture resulted in poor quality material. The new standards have been stored as aqueous NaCl in break seal vials.

A.1 Materials

To make the ^{36}Cl/Cl standard series, a source of stable Cl with blank levels ^{36}Cl and a standard with high levels of ^{36}Cl are needed. For stable Cl, a blank level solid NaCl sample called 'Pugwash' was used. The NIST SRM 4943 ^{36}Cl [87] was used for ^{36}Cl. Details on both samples can be found in Sections A.1.1 and A.1.2, respectively.

A.1.1 Pugwash blank

The Pugwash blank was provided as solid NaCl from Dr. John Gosse, Dalhousie University. It is from the Windsor Salt Mine in Pugwash, Cumberland County, Nova Scotia, Canada. Because ^{36}Cl is produced in the atmosphere, the NaCl in the mine has low levels of ^{36}Cl, making the sample ideal to dilute the ^{36}Cl/Cl ratio. Previous AMS measurements of the Pugwash NaCl provided a ^{36}Cl/Cl ranging from 0.12 x10^{-15} to 6.6 x10^{-15} [90].

A.1.2 NIST SRM 4943

The NIST SRM 4943 is a ^{36}Cl radioactivity standard prepared in the Center for Radiation Research, Nuclear Radiation Division, Radioactivity Group [87]. It comes in a flame-sealed borosilicate-glass ampoule as a 3 mL NaCl solution. The solution has 0.2 g of NaCl per liter of water. As of December, 1984 it had a radioactivity concentration of 1.095 x10^4 $\frac{Bq}{g}$ with a 0.82% uncertainty, measured by a 4π β gas-proportional counter. The ^{36}Cl/Cl ratio of this standard is calculated in Section A.2.1.

A.2 Dilution procedure

A saltwater ^{36}Cl blank solution was prepared using the solid Pugwash. The Pugwash was diluted to 10,000 ppm using 1 L of MilliQ water. The MilliQ water was first tested for Cl content, with the concentration being below the limit of detection of ICP-MS.

The NIST SRM 4943 standard was opened and 20 μL was removed using a micropipette. This was added to a small vial, tared on a microbalance. The weight of the NIST SRM was recorded. Using a micropipette, the 20 μL was removed from the vial and added to 400 mL of Pugwash solution in a 500 mL Nalgene bottle. This completed the dilution 1 listed in Table A.1. An example calculation for the necessary mixtures can be found in Section A.2.2. The remainder of the NIST SRM 4943 standard (approximately 3 mL) was pipetted into a new break seal ampoule and sealed off for safe storage.

Dilution 2 is made by measuring 20 μL of dilution 1 and dispensing it into a tared vial on the microbalance for accurate mass measurement. The 20 μL of dilution 1 was added to 85 mL of Pugwash solution. A 150 mL Wheaton bottle was used to mix the solution. This solution (dilution 2) is used for all further dilutions. The remainder of dilution 1 was stored in sealed ampoules.

Depending on the volume needed, a new vial (dilutions 5-7) or a 15 mL centrifuge bottle (dilutions 3, 4) were weighed and the desired volume of dilution 2 will be added to it using a pipette. The required volume of Pugwash is listed in Table A.1. Dilution 8 was taken as a sample from the 10,000 ppm Pugwash solution. All unused standards were sealed in

Dilution Number	Target Standard ^{36}Cl/Cl	Standard Dilution Number Used	Calculated SRM 4943 Mixture (ml)	Calculated Pugwash (ml)	Measured SRM 4943 Mixture (g)	Measured Pugwash (mg)	Calculated Standard ^{36}Cl/Cl
0	7.28x10^{-2}	N/A (NIST)	N/A	N/A	N/A	N/A	7.28x10^{-2}
1	4.42x10^{-8}	0	0.02	400	0.0195	400.00	4.31x10^{-8}
2	1.04x10^{-11}	1	0.02	85	0.0199	85.01	1.03x10^{-11}
3	1.03x10^{-12}	2	11	100	11.03	99.99	1.03x10^{-12}
4	5.00x10^{-13}	2	5	100	5.02	100.01	4.96x10^{-13}
5	1.06x10^{-13}	2	0.98	100	0.9873	100.03	1.04x10^{-13}
6	5.26x10^{-13}	2	0.46	100	0.4628	100.01	5.01x10^{-13}
7	1.02x10^{-14}	2	0.04	80	0.0393	80.04	7.63x10^{-15}
8	5.05x10^{-15}	2	0	35	0	N/A	5.05x10^{-15}

Table A.1: Targeted ^{36}Cl/Cl Ratios for the set of standards, calculated Pugwash and NIST SRM 4943 volumes to achieve these ratios, masses weighed during preparation, and the final calculated ^{36}Cl/Cl.

ampoules.

A.2.1 Standard ^{36}Cl/Cl calculation

Prior to calculating the dilutions necessary to produce the desired range of ^{36}Cl/Cl standards, the ^{36}Cl/Cl ratio of the NIST SRM 4943 standard needs to be determined. With the data provided in section A.1.2, the NaCl concentration is 200 ppm. From this, the Cl concentration can be calculated:

$$\begin{aligned}[Cl] &= \frac{[NaCl]M_{\mathrm{Cl}}}{M_{\mathrm{NaCl}}} \\ &= \frac{200ppm(35.453\frac{g}{mol})}{58.44277\frac{g}{mol}} \\ &= 121.3ppm\end{aligned} \tag{A.1}$$

The mass of the NaCl in the solution is:

$$\begin{aligned}m_{\mathrm{NaCl}} &= [NaCl]V \\ &= 0.2\frac{g}{L}(0.003L) \\ &= 0.0006g\end{aligned} \tag{A.2}$$

Giving a total mass of the sample of 3.0006 grams. The mass and the atoms of stable

Cl can then be found.

$$\begin{aligned} m_{\mathrm{Cl}} &= \frac{m_{\mathrm{NaCl}}M_{\mathrm{Cl}}}{M_{\mathrm{NaCl}}} \\ &= \frac{(0.0006g)(35.453\frac{g}{mol})}{58.44277\frac{g}{mol}} \\ &= 3.63x10^{-4}g \end{aligned} \tag{A.3}$$

$$\begin{aligned} \text{Cl atoms} &= \frac{m_{\mathrm{Cl}}N_{\mathrm{A}}}{M_{\mathrm{Cl}}} \\ &= \frac{(3.63\text{x}10^{-4}g)(6.02\text{x}10^{23}mol^{-1})}{35.453\frac{g}{mol}} \\ &= 6.18\text{x}10^{18}atoms \end{aligned} \tag{A.4}$$

To find the modern activity of the sample, we can use the specific activity provided and the half-life of ^{36}Cl [41]. Because the half life is significantly longer than the 37 years that have passed since the activity was measured, the modern activity will have little difference.

$$\begin{aligned} A_0 &= mA_{\mathrm{s}} \\ &= (3.0006g)(1.095\text{x}10^4\frac{Bq}{g}) \\ &= 3.2856\text{x}10^4 Bq \end{aligned} \tag{A.5}$$

$$\begin{aligned} A &= A_0 e^{\frac{-ln(2)T}{t_{1/2}}} \\ &= (3.2856\text{x}10^4 Bq)e^{\frac{-ln(2)1.17\text{x}10^9 s}{9.53\text{x}10^{12}s}} \\ &= 3.2853\text{x}10^4 Bq \end{aligned} \tag{A.6}$$

The number of ^{36}Cl atoms can be found from the half life and the activity.

$$\begin{aligned} {}^{36}\text{Cl atoms} &= \frac{At_{\frac{1}{2}}}{ln(2)} \\ &= \frac{(3.2853\text{x}10^4 Bq)(9.53\text{x}10^{12}s)}{ln(2)} \\ &= 4.502\text{x}10^{17}atoms \end{aligned} \tag{A.7}$$

Using the calculations in Equations A.4 and A.7, the ^{36}Cl/Cl ratio of NIST SRM 4943 can be determined.

$$\begin{aligned}\frac{^{36}Cl}{Cl} &= \frac{4.502\text{x}10^{17}atoms}{6.18\text{x}10^{18}atoms} \\ &= 7.282\text{x}10^{-2}\end{aligned} \tag{A.8}$$

This ratio agrees with an external calculation by Sharma *et al.* [89].

A.2.2 Dilution calculations

Using the ratio in Equation A.8, the necessary dilutions can now be calculated. An example calculation can be seen below. The final calculated and measured mixture numbers can be found in Table A.1.

Beginning with a nominal 10,000 ppm Pugwash solution (measured at 9758 ppm) with a ^{36}Cl/Cl ratio of approximately 5.05 x10^{-15} [90], we made 400 mL of the first dilution. Using these values, we can find the mass and the number of atoms of stable Cl in our Pugwash solution.

$$\begin{aligned}m_{\text{Cl}} &= \frac{(10,000\frac{mg}{L})(0.4L)}{1000\frac{mg}{g}} \\ &= 4g\end{aligned} \tag{A.9}$$

$$\begin{aligned}\text{Cl atoms} &= \frac{m_{Cl}N_A}{M_{Cl}} \\ &= \frac{(4g)(6.02\text{x}10^{23}mol^{-1})}{35.453\frac{g}{mol}} \\ &= 6.79\text{x}10^{22}atoms\end{aligned} \tag{A.10}$$

The known ^{36}Cl/Cl ratio can be used to determine the number of ^{36}Cl atoms:

$$\begin{aligned}{}^{36}\text{Cl atoms} &= \text{Cl atoms}\frac{^{36}Cl}{Cl} \\ &= (6.79\text{x}10^{22}atoms)(5.05\text{x}10^{-15}) \\ &= 3.43\text{x}10^{8}atoms\end{aligned} \tag{A.11}$$

The same equations are used to calculate the Cl and ^{36}Cl atoms of the SRM 4943, using

121.3 ppm, 2 x10^{-5} l, and a ^{36}Cl/Cl ratio of 7.28 x10^{-2}. This results in 4.12 x10^{16} Cl atoms and 3x10^{15} ^{36}Cl atoms. To calculate the final ratio, the number of stable and rare atoms from each solution can be added and the ratio is taken.

$$\begin{aligned}\text{Cl atoms} &= \text{Pugwash Cl atoms} + \text{SRM 4943 Cl atoms}\\ &= 6.79\text{x}10^{22} atoms + 4.12\text{x}10^{16} atoms\\ &= 6.79\text{x}10^{22} atoms\end{aligned} \tag{A.12}$$

$$\begin{aligned}{}^{36}\text{Clatoms} &= \text{Pugwash}^{36}\text{Clatoms} + \text{SRM 4943}^{36}\text{Clatoms}\\ &= 3.43\text{x}10^{8} atoms + 3\text{x}10^{15} atoms\\ &= 3\text{x}10^{15} atoms\end{aligned} \tag{A.13}$$

$$\begin{aligned}\frac{^{36}Cl}{Cl} &= \frac{3\text{x}10^{15} atoms}{6.79\text{x}10^{22} atoms}\\ &= 4.42\text{x}10^{-8}\end{aligned} \tag{A.14}$$

Further dilutions use the same method but use the stable Cl atoms in the last solution instead of SRM 4943. The Pugwash is still used for the dilution.

Appendix B

Preparation of ^{36}Cl samples and targets

B.1 Column conditioning

An ion exchange column was packed with Dowex 1x8 100-200 mesh, ion-exchange resin. The column was conditioned with 150 mL of 1.5 M nitric acid. 3 drops of 1 M silver nitrate were added to the last 5 mL of eluent to test for remaining chloride in the resin. Additional nitric acid was added until the test showed no chloride in the last 5 mL. The column was then washed with 300 mL of Milli-Q water. The resin was kept moist until ready to use with the last 2-3 mL of water.

B.2 Sample preparation

An approximate Cl concentration of each of the water samples was provided by the supplier of the samples. Enough water sample for 5 mg of silver chloride was measured. If the samples did not have sufficient quantities of Cl for 5 mg of silver chloride, the Pugwash carrier was added to increase the Cl content without increasing the ^{36}Cl. Additional details on Pugwash are in Section A.1.1.

The samples were poured through the columns. 10 mL of 0.1 M ammonium hydroxide followed the samples and then 10 mL of 0.05 M nitric acid was drained to the top of the resin. 5 mL of 0.50 M nitric acid was added to the column; A 50 mL centrifuge tube with 10 drops of 1 M silver nitrate solution was placed below the column to catch the solution as it drained to the top of the resin. 20 drops of 6 M nitric acid was added to the centrifuge tubes and swirled to coagulate the silver chloride. The centrifuge tubes were refrigerated overnight.

B.3 Chloride purification

The columns were conditioned following the same procedure as described in Section B.1.

The samples were centrifuged and the supernatent was discarded. To redissolve the silver chloride, 5 mL or more of Milli-Q water and 20 drops of ammonium hydroxide were added to the sample tubes. The dissolved samples were added to the columns and the ammonium hydroxide was drained to the top of the resin. 10 mL of 0.1 M ammonium hydroxide was used to rinse the centrifuge tube and drained through the resin. 5 mL of 0.5 M nitric acid was added to the column and caught with a 50 mL centrifuge tube. This was repeated until the resin was clean. 20 drops of nitric acid were added to the centrifuge tubes, swirled to coagulate silver chloride and refrigerated overnight.

B.4 AgCl precipitate

A 5 mL centrifuge tube was weighed for each sample. The samples were centrifuged and the supernatent was discarded using a transfer pipette. The sample was rinsed with 1 mL of Milli-Q water to dislodge and pipette the precipitate. It was transfered to the 5 mL centrifuge tube and was centrifuged for 20 minutes. The remaining supernatent was removed and the sample was left in the oven overnight to dry. The samples were weighed for the final silver chloride mass the following day.

B.5 Target preparation

The AgCl is mixed with niobium at a ratio of 1:3 by volume. Approximately 5 mg of the AgCl-Nb mixture is pressed into the target using a 3 ton pneumatic press.

Appendix C

Accelerator settings for ^{36}Cl measurements

Before a run several electronic connections need to be moved from the main injection line to the Research Line. These include the bouncer, the 120° magnet thermocouple interlock and deGaussing supply. The ISA LE off-axis cups need to be connected to the converter cables so that batch mode will read them. The terminal voltage needs to be conditioned to 3100 kV and the HE ESA needs to be conditioned to 99 kV. After a Cl run, all cables and power supplies need to be reconnected to the main injection line components. The slits, GIC pressure, and amplifier gains should be adjusted by the next accelerater operator.

In a Cl run, the stable beams (^{35}Cl and ^{37}Cl) were measured in the ISA LE off-axis cups. ^{36}Cl was measured in the GIC. The approximate settings for the accelerator beamline used in a Cl run are found in Table C.1. The slit and aperture settings are found in Table C.2. The approximate ISA settings are found in Table C.3. The accelerator and ISA settings can be tuned from these initial settings or from the settings of the last Cl run.

The targets in a batch run should include at least three sets of targets for three standards and one process blank. At least two targets of each unknown sample should also be included. Runs were completed using a LE-FSI batch run with thirty seconds per block and without injection of the stable beams into the ISA. Five blocks were done in the first pass and fifty blocks per pass and minimum of three passes per target.

Component	Value	Component	Value
Tuning Bouncer DC Voltage	-500V	SO-110-2 Y-Steerer	75.82V
Cs Temperature	100^{o}C	SO-110-2 X-Steerer	10.13V
Target Voltage	7kV	ISA LE X-Steerer	N/A
Extraction Voltage	13kV	ISA LE Y-Steerer	N/A
Terminal Voltage	3000kV	BI LE X1-Steerer	24.79V
ISA Deck Voltage	20009V	BI LE X2-Steerer	47.74V
Stripper Pressure	1.2x10^{-2}mbar	BI LE Y1-Steerer	Grounded
Slit-Err Cup Selection	N/A	BI LE Y2-Steerer	-153.72V
GIC Pressure	15.0mbar	HE X1-Steerer	4387V
dE Amplifier Gain	20-12.00	HE X2-Steerer	-406V
E_f Amplifier Gain	20-12.00	HE Y1-Steerer	4728V
ISA Off-Axis IN Cup Position	112.9	HE Y2-Steerer	-296V
ISA Off-Axis OUT Cup Position	9866.8	LE ESA	2504.9V
ISA Off-Axis Cups Range	Auto	HE ESA	92.174kV
Bouncer Voltage for ^{35}Cl$^-$	613.5V	SO-110-2 Lens	14.076kV
Bouncer Voltage for ^{36}Cl$^-$	40.8V	ISA Deceleration Lens 1	16468V
Bouncer Voltage for ^{37}Cl$^-$	-500V	ISA Deceleration Lens 2	0V
LE Magnet Current	42.217A	ISA Acceleration Lens 1	1706V
LE Magnet Field	0.148019T	ISA Acceleration Lens 2	0V
BI Magnet DeGauss	42mA	CON Lens	26.984%
HE Magnet Current	87.735A	BI Lens	14.403kV
HE Magnet Field	0.483500T	ACC Lens	59.12kV
Switching Magnet Current	64.080A	ACC Q-Pole Focus	63.248%
		ACC Q-Pole Astigmatism	-2.137%
		HE Q-Pole Focus	38.437%
		HE Q-Pole Astigmatism	2.674%
		RI Foil Q-Pole Focus	0%
		RI Foil Q-Pole Astigmatism	0%
		RI ESA Q-Pole Focus	25.421%
		RI ESA Q-Pole Astigmatism	20.549%

Table C.1: Example settings for the components of the accelerator line for ^{36}Cl runs.

Component	Value
Slits at LE magnet object plane	10.00 / 10.00
Slits at LE magnet focal place	10.00 / 10.00
Aperture at LE magnet focal place	Out
Slits after ISA	10.00 / 10.00
Slits at BI magnet focal plane	10.00 / 10.00
Aperture at BI magnet focal plane	Out
Slits at HE magnet object plane	10.00 / 10.00
Slits after BI	10.00 / 10.00
Aperture at HE magnet object plane	Out
Aperture at HE magnet exit	Out
Slits at HE magnet focal plane	5.00 / 5.00
Aperture at HE magnet focal plane	Out
Slits at RI ESA exit	10.00 / 10.00
Slits at GIC	5.00 / 5.00

Table C.2: Slit settings along the accelerator run for ^{36}Cl runs.

Component	Value	Component	Value
Deceleration Cone	326V	Segment 1	43V
Deceleration Cone setting	5200 setting	Segment 2	-16V
Acceleration Cone	480V	Segment 3	-9V
Aperture 1	62V	Segment 4	-9V
Aperture 2	-6V	Segment 5	-4V
Aperture 3	5.3V	Segment 6	-6V
Radiofrequency 1	1150V$_{pp}$	Segment 7	-1V
Radiofrequency 2	1360V$_{pp}$	Segment 8	0V
		Segment 9	2.1V
		Segment 10	14.1V

Table C.3: Example settings for the components of the ISA line for ^{36}Cl runs.